Automated Surface Classification of SRF Cavities for the Investigation of the Influence of Surface Properties onto the Operational Performance

Dissertation

zur Erlangung des Doktorgrades
des Department Physik
der Universität Hamburg

vorgelegt von

MARC WENSKAT

aus Kaiserslautern

Hamburg
2015

"Ceci n'est pas une pipe"
- Rene Magritte

"All models are wrong, but some are useful"
- George E.P. Box

"Be water, my friend"
- Lee Jun Fan

Abstract

Superconducting niobium radio-frequency cavities are fundamental for the European XFEL and the International Linear Collider. To use the operational advantages of superconducting cavities, the inner surface has to fulfill quite demanding requirements. The surface roughness and cleanliness improved over the last decades and with them, the achieved maximal accelerating field. Still, limitations of the maximal achieved accelerating field are observed, which are not explained by localized geometrical defects or impurities. The scope of this thesis is a better understanding of these limitations in defect free cavities based on global, rather than local, surface properties.

For this goal, more than 30 cavities underwent subsequent surface treatments, cold RF tests and optical inspections within the ILC-HiGrade research program and the XFEL cavity production. An algorithm was developed which allows an automated surface characterization based on an optical inspection robot. This algorithm delivers a set of optical surface properties, which describes the inner cavity surface. These optical surface properties deliver a framework for a quality assurance of the fabrication procedures. Furthermore, they shows promising results for a better understanding of the observed limitations in defect free cavities.

Zusammenfassung

Supraleitende Hochfrequenz-Resonatoren aus Niob sind die Grundlage für den Europäischen XFEL und den International Linear Collider. Um die Vorteile des Betriebs von diesen supraleitenden Resonatoren zu nutzen muss die innere Oberfläche hohen Ansprüche erfüllen. Die Oberflächenrauheit und Reinheit dieser Resonatoren hat sich in den vergangenen Jahrzenten deutlich verbessert, und mit ihnen die maximal erreichbare Beschleunigungsspannung. Dennoch treten Limitationen der Beschleunigungsspannung auf, welche nicht durch lokale geometrische Defekte oder Unreinheiten erklärt werden. Das Ziel dieser Arbeit ist ein besseres Verständnis dieser Limitationen in defektfreien Resonatoren aufgrund von globaler anstatt lokaler Oberflächeneigenschaften.

Speziell für diesen Zweck durchliefen mehr als 30 Resonatoren Oberflächenbehandlungen, Hochfrequenztests und optischen Inspektionen während der XFEL Resonatorproduktion und des ILC-HiGrade Forschungsprogramm. Es wurde ein Algorithmus entwickelt, welcher eine automatische Oberflächenklassifizierung ermöglicht, basierend auf einem Roboter für optische Inspektionen. Dieser Algorithmus liefert einen Satz von Variablen, welche die innere Resonatoroberfläche beschreibt. Diese optischen Oberflächeneigenschaften liefern ein Bezugssystem für die Qualitätssicherung der Herstellungsprozeduren. Zusätzlich ergeben sich vielversprechende Ergebnisse für ein besseres Verständnis der beobachteten Limitationen in defektfreien Resonatoren.

Contents

CHAPTER 1

Introduction

The first steps towards the Standard Model (SM) of particle physics were made in 1961 with Glashow's work on the unification of electromagnetism and weak forces into a electroweak theory [1] and culminated in the discovery of a spin zero boson with a mass of (125.09 ± 0.24) GeV [2–4] at the Large Hadron Collider (LHC) in 2012, which is widely regarded as the predicted and awaited SM Higgs particle [5]. Although the Standard Model is a theory with an excellent agreement between theory and experiment, many open questions, which can not be addressed consistently within the Standard Model, still exist [6–10]. Even the discovered boson could be a first trace towards physics beyond the Standard Model. Different theoretical extensions of the Standard Model make different predictions on the properties of this and possible other new particles. Hence, detailed and precise analysis of these properties are essential. But given the fact that the LHC is a proton collider, and protons are composite particles, precision measurements at this facility demand sophisticated experiments which have to deal with not-well defined initial states during particle collisions. To overcome these intrinsic difficulties of a hadron facility, a lepton-antilepton collider is well suited as a successor and complementary to the LHC. The physics case for such a lepton-antilepton collider is quite clear, since it can complement and augment the research program carried out at the LHC and has been studied for several years [11–14]. The only lepton-antilepton collider design at present, which has already proven to be realizable, is the International Linear Collider (ILC) [15, 16], see chapter 2 of this thesis for details.

The key technology of the ILC are superconducting radio frequency (SRF) accelerating structures called *cavities*. The advantages and specific terms of operations for these superconducting cavities will be discussed in chapter 3 of this thesis. Generally speaking, the properties of the inner surface play a crucial role to maintain the superconducting phase during operation with an externally applied accelerating field. In order to achieve high accelerating fields, the inner cavity surface has to fulfill certain quality demands and in chapter 4, the emphasis lies on the fabrication steps and the surface treatments of the cavities used for the European X-ray Free Electron Laser (XFEL) cavity production.

Although sophisticated diagnostic methods to investigate the cavity RF performance are available, see chapter 5, up to now no formulation and quantitative analysis of these surface demands in terms of optical methods has been done.

This thesis quantitatively characterizes the inner cavity surface with images obtained with the help of an optical inspection robot and to investigate possible correlations between optical surface properties and the RF performance of cavities. Chapter 6 describes the optical inspection robot which has been developed at DESY and is used for the image acquisition of this work. The image processing and analysis code, developed for this purpose is presented in chapter 7. In addition, it includes series of benchmarks of the code and the introduction of optical surface properties which are used to quantify the surface as captured by the optical system. Chapter 8 introduces a characterization of the cavity surface by means of the newly defined optical surface properties. Additionally, the surface change under chemical surface treatment - which is well known and described - serves as test case for these optically obtained surface properties. Chapter 9 shows the existence of vendor dependent optical surface properties which can be traced back to specific fabrication and surface treatment steps. The last chapter concludes with a study on the correlation of optical surface properties and RF performance and how this concurrence can be interpreted by means of theoretical models. The tools and algorithms developed in the scope of this thesis and the presented results can become a cornerstone of a quality assurance for the future ILC cavity production.

CHAPTER 2

Pathway to the International Linear Collider

The idea to construct a superconducting linear accelerator for energies in the TeV regime came up in the early 1990s by Bjorn Wiik [17]. An enormous effort was put into this vision to realize the needed technology. An incomplete overview of existing accelerators along the path to the ILC is given in this chapter.

2.1   Tesla Test Facility and FLASH

In 1992 a linear accelerator prototype was proposed to test superconducting materials and develop treatment procedures for accelerating structures called cavity with a designated design. It was named Tesla Test Facility (TTF) and is located at DESY [18, 19]. TTF evolved into a user facility named Free Electron Laser in Hamburg (FLASH) [20]. The first lasing in the nanometer regime was observed in 2002 [21] and the evolution of the machine [22–24] lead to a first harmonic wavelength of 4.1 nm [25,26] which allows water to become transparent and new kind of experiments are possible at FLASH. FLASH is a unique facility for a variety of research fields, such as material science, pharmaceutics, biology and physics. An overview over the research done in the last years is given in [27–29].

The key technology is the superconducting cavity, which has several advantages against normal conducting technology, see section 3 for details. FLASH itself underwent many upgrades [30–33], where the latest upgrade included several module exchanges and the installation of the newest XFEL-type module [34] with an average gradient of 30 MV/m [32]. In the mean time, FLASH has been upgraded with a second undulator beamline FLASH II [35,36]. In figure 2.1 the current version of the machine is shown. The machine parameters are listed in table 2.1.

Beam energy	[GeV]	1.25
Nominal accelerating field	[MV/m]	26
Number of TESLA Cavities		65
Repetition rate	[Hz]	5-10
Radio frequency pulse length	[ms]	1300
Bunch length	[ms]	800
Bunch charge	[nC]	0.1-1
Average beam current	[mA]	9
Radio frequency	[GHz]	1.3
Effective acceleration length	[m]	56

Table 2.1: Machine parameters of FLASH [28]
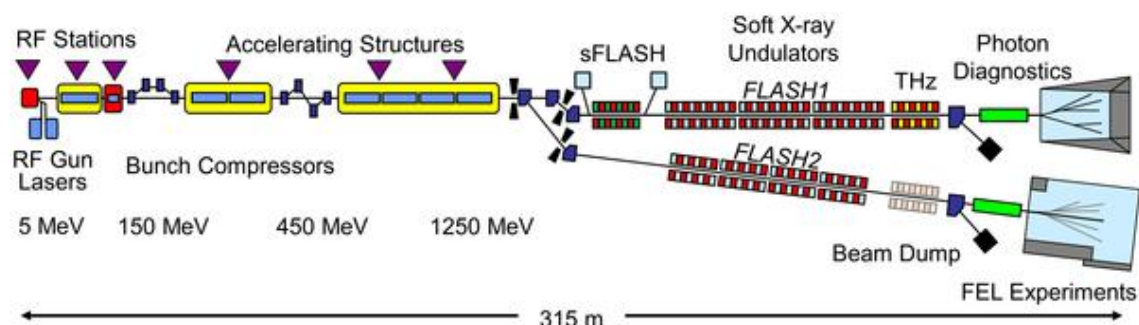
Figure 2.1: Layout of FLASH. The electron gun is on the left, the experimental hall on the right. The superconducting linac consists of seven accelerator modules with TESLA-type cavities (yellow), one 3rd-harmonic module (red, [37]) and magnetic chicanes for bunch compression. Behind the last accelerating module, the beam is switched between FLASH I, which is the present undulator line, and FLASH II, which is the upgrade. Towards FLASH I, after the dogleg, a seeding section, a longitudinal beam diagnostic section (LOLA) and the soft x-ray undulator is installed [33]. Behind the extraction point for FLASH II, space is reserved for an additional laser system for seeding.

At FLASH it is a possible to test the low level radio frequency (LLRF) control of the cavities. The LLRF control is a vital component to operate several coupled cavities, each close to its individual limits, with demanding beam parameters. The FLASH 9mA run simulates an environment comparable to the design values of the International Linear Collider (ILC). Stable operation of the accelerator with long bunch trains, high current and high gradients close to the operational limits were achieved [38–41], which is an important step towards the realization of the ILC.

2.2 European X-Ray Free Electron Laser

FLASH represents a successful test of a new accelerating technique and operates as an intense light source for users such as material science, structural biology and research on infection, but the increasing request of beam time lead to the decision towards a 3.4 km long accelerator using the same key technology. The European X-Ray Free Electron Laser (XFEL) was proposed in 2007 [34] and is currently under construction. In figure 2.2 an overview of the machine is shown. The nominal accelerating field at XFEL is 23.6
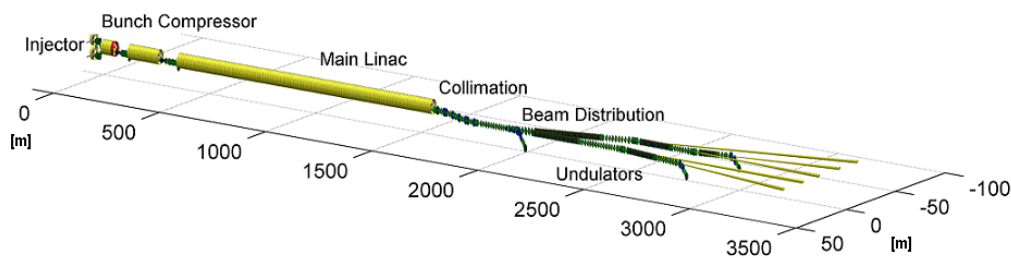
Figure 2.2: Layout of the XFEL. The acceleration section will have a length of 1.2 km. A beam delivery system will distribute the accelerated electron beam into five distinct tunnels with undulators to generate intense laser pulses [34].

MV/m [34], in table 2.2 the XFEL machine parameters are given. To achieve this high accelerating field, a dedicated cavity surface treatment has been defined, see chapter 4. The main challenge for XFEL is the industrialization of the cavity production [42,43]. To qualify each fabrication and surface treatment step, a quality control was established and reference cavities underwent an acceptance test after each fabrication step [44]. The experience gained through the production of the 800 cavities for XFEL is valuable information towards the planning of the International Linear Collider [45]. With half of the cavities delivered, first analysis concerning stability of the process, quality assessment and results of the productions were published [46–48] and toy models about the impact on the ILC production are developed [49].

In addition to the 800 XFEL cavities, the ILC-HiGrade program was set up [50,51]. This includes the production of 24 cavities within the standard XFEL production, as additional quality assessment but also to investigate the cavity properties like RF performance and surface properties in detail. The work presented in this thesis is based on the HiGrade cavities.

2.3 International Linear Collider

The International Linear Collider [15, 16] is the successor of three national projects. In 2004 the decision was made that the accelerator should be based on superconducting technology developed by the TESLA collaboration [52].

Beam energy	[GeV]	17.5
Nominal accelerating field	[MV/m]	23.6
Number of TESLA Cavities		800
Repetition rate	[Hz]	10
Radio frequency pulse length	[ms]	1400
Bunch length	[ms]	650
Bunch charge	[nC]	1
Average beam current	[mA]	5
Radio frequency	[GHz]	1.3
Effective acceleration length	[m]	800

Table 2.2: Machine parameters of the XFEL [34]

Although other concepts exist for a lepton collider [53, 54], the ILC is the most advanced design with operational experience of components and proven concepts.
Some advantages of a lepton collider against a hadron collider are

- The colliding leptons are point-like particles. No statistical assumptions of the involved partons in the production process necessary.

- Reduced background for lepton collisions, which would be caused by multi-parton interactions.

- Initial state center-of-mass energy and polarization is well known and controllable.

After the discovery of a new boson at 125.09 ± 0.24 GeV at the LHC [2–4], the physics case for the ILC was pushed. As for many reasons, the common interpretation of this new particle is that a Higgs boson has been discovered. Fur further analysis several priorities have been defined. To understand the boson and its implication the studies need to include precision measurements of the mass (1), its spin and parity (2), the coupling to gauge bosons (3) and decay branching ratios (4) as well as the total decay width (5), the Yukawa coupling to the top quark (6) and its coupling (7). Besides the Higgs, other important questions will be investigated, see [11–14, 55] for details.
A staged construction of the ILC is foreseen. At the first stage with a center of mass (cms) of 250 GeV the tasks one to five can be investigated while six and seven would require a cms of 500 GeV [56]. Further upgrades of the machine going to 1 TeV via extensions of the linear accelerator or plasma-wakefields as an afterburner [57] are possible.
A schematic view of the ILC is shown in figure 2.3. The electrons are retrieved from a polarized source and are accelerated to 250 GeV and injected into undulators to produce the positrons. The 3.2 km damping rings are used to reduce the beam emittance which is needed for a high luminosity at the interaction point (IP). A dedicated beam delivery system transfers the beam to the linac, with its design parameters given in table 2.3. The main linac consists of 16000 cavities, where the cavities will be assembled in cryomodules. A single cryomodules will support nine cavities or eight cavities and one quadrupole

Beam energy	[GeV]	500
Luminosity	[cm^{-2}s^{-1}]	$2 \cdot 10^{34}$
Nominal accelerating field	[MV/m]	31.5
Number of TESLA Cavities		16000
Repetition rate	[Hz]	5
Radio frequency pulse length	[ms]	1600
Bunch length	[ms]	970
Bunch charge	[nC]	3.2
Average beam current	[mA]	9
Radio frequency	[GHz]	1.3
Effective acceleration length	[m]	$\approx 2 \cdot 8000$

Table 2.3: Machine parameters of the ILC [16].

magnet. Three cryomodules, in an 8-9-8 cavity arrangement, will be powered by a single RF power unit. The bunch timing structure foreseen at the ILC is a 2625 bunch train with a total length of 1 ms and a bunch spacing of 300 ns and a 199 ms gap between each bunch train.

To reduce the luminosity loss at the IP caused by an angle between the colliding beams, a crab cavity system is installed before the IP [58]. Close to the IP two detectors will be placed [59, 60], were only one at a time will be in the IP for data taking [61].
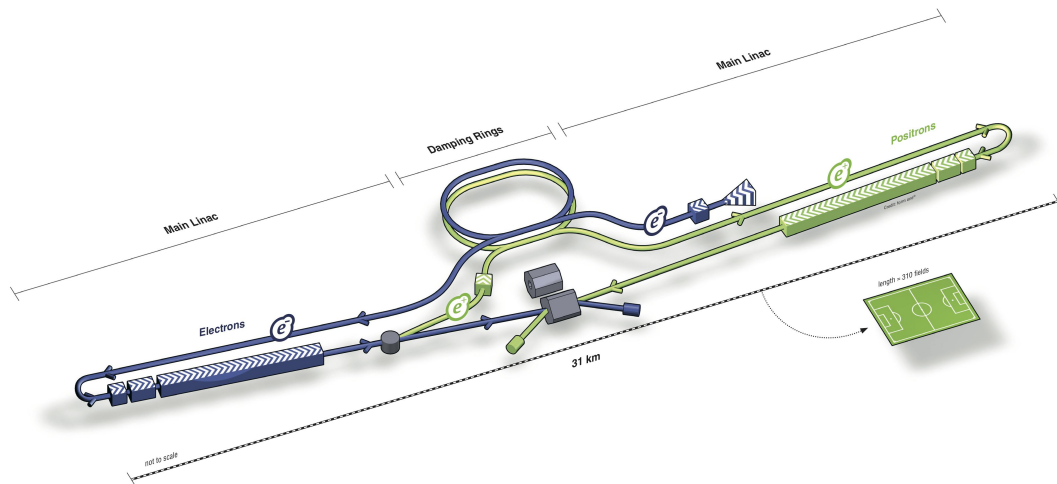
Figure 2.3: Schematic view of the ILC The linear accelerator will have a length of 2×8 km [16].

The production of 16000 superconducting cavities with a nominal accelerating field of 31.5 MV/m will be a technological and logistical challenge. A global effort to realize this goal with regional R&D programs is needed to realize such an ambitious goal.

CHAPTER 3

Essentials of Superconductivity and RF Cavities

A large variety of radio frequency (RF) cavities are used in particle accelerators. Historically, most have been made of copper and operated near room temperature with water cooling to dissipate the ohmic induced heating. Superconducting RF cavities enable accelerators to increase accelerating field levels while reducing the use of electrical power. The ultra-low electrical resistivity of a superconducting material allows a cavity to obtain an extremely high quality factor, Q_0 - see section 3.2.4. The advantages of superconducting against normal conducting cavities are

- *Low beam impedance*: The low electrical loss in an SRF cavity allows their geometry to have large beam pipe apertures while still maintaining a high accelerating field along the beam axis. Normal-conducting cavities need small beam apertures to concentrate the electric field as compensation for power losses in wall currents. However, the small apertures have a negative influence onto the particle beam due to their excitation of larger wakefields.

- *Higher duty cycle*: A higher duty cycle or even continuous wave (cw) operation of a machine increases the luminosity for a collider or brilliance for a light source. Because of the low losses during operation, the cavities can run at high accelerating fields with high duty cycle in comparison to normal conducting cavities. Given the operating parameters of superconducting cavities, the dissipated heat in normal conducting cavities would melt the copper by any means.

- *Lower energy spread*: Because of the low losses, SRF cavities allow a standing wave operation with constant accelerating field without dissipating to much energy into the material. This leads to a rather low energy spread within the beam, even for long beam pulses, since every particle sees the same field. In contrast to normal conducting cavities, where, because of the higher dissipation, the beam must be rather short or the energy spread will increase.

First, an overview of the basic principles and theories of superconductivity will be given. A description of the working principle and key parameters of RF cavities will follow and the chapter will conclude with a discussion of SRF limitations due to cavity surface properties.

3.1   Superconductivity

In 1911, a series of papers were published by Heike Kamerlingh-Onnes [62–64] in which he described the vanishing direct current (DC) resistance of mercury below a critical transition temperature T_C. This effect was later named superconductivity and lead to a series of discoveries and applications. One application of superconductivity in accelerator physics are superconducting cavities. The first SRF cavity was tested in 1974 [65] and the first synchrotron based on SRF cavities, the Cornell Electron Storage Ring (CESR), was constructed in 1975 [66]. From this time on, SRF cavities underwent an evolution in design, material and surface treatment. The current state of the art design, for particles with a ratio of $\frac{v}{c} \approx 1$, is the TESLA-cavity design [67] produced of niobium.

3.1.1   Microscopic Theory of Superconductivity

After the discovery by Kamerlingh-Onnes many attempts where made to understand and describe the vanishing DC resistance. In 1950, two papers were published which describe that the critical transition temperature T_C [68, 69] depends on the isotopic mass of a material. This dependency leads to the deeper insight that superconductivity is not just an electric effect but also includes electron-lattice interactions. Cooper described a bounded state of two electrons via an attractive virtual phonon interaction in [70] which lays the foundation of the BCS-Theory, named after Bardeen, Cooper and Schrieffler [71]. A phonon can be understood as a quasi-particle and the discrete state of lattice vibrations. While an electron travels along the atomic lattice, polarizes it and hence excites lattice vibrations, a second electron travels along the wakefield of the first electron and experiences an indirect attraction. The attraction of the second electron towards the first electron is the polarized potential of the atomic lattice and is maximized, when the second electron travels along the path of the first electron but with opposite momentum. Below the transition temperature this attraction is strong enough to create a bound state of these two electrons, which is then called a Cooper pair. Such a Cooper pair forms a singulet which is described via an antisymmetric spin- and symmetric space-wavefunction Ψ

$$\Psi = \left\{ \vec{k} \uparrow, -\vec{k} \downarrow \right\}$$

with $\vec{k}$ and $-\vec{k}$ as the impulse and $\downarrow$ and $\uparrow$ as the spin of the single electrons. They form a singulet state with an effective total momentum of zero.

This means that such a pair can be considered as a single boson and all Cooper pairs act as a superconducting fluid with a single wavefunction. The bound state of the electrons

is energetically favored below the transition temperature. Not all electrons of the Fermi-gas can condense into Cooper pairs. Only the electrons which can be scattered into an unoccupied state which is in the range around $E_F \pm \hbar \omega_C$ while ω_C is the highest phonon-frequency for which the the interaction potential is still attractive and E_F as the Fermi-energy, the energy of the highest occupied state. This means, that only a thin spherical shell in the Fermi-space contributes to superconductivity. The energy of the bound system is

$$E_{BCS} = 2 \cdot E_F - \Delta \tag{3.1}$$

with Δ as the condensation energy or 'gap'. The gap itself depends on material parameters and the temperature and can be calculated to [72]

$$\Delta_0 = 1.76 \cdot k_B \cdot T_C \tag{3.2}$$

with k_B as Boltzmann constant, T_C the material dependent critical temperature for the phase transition, and $\Delta(T = 0) = \Delta_0$ in the order of 10^{-5} eV. The vanishing DC resistance can be explained with the existence of the gap. The DC resistance is a consequence of energy transfer via elastic scattering of an electron and the atomic lattice. In the superconducting state, the Cooper pair prevents any energy transfer below the value of the gap, which would break up this pair. Hence the scattering probability decreases and the resistance vanishes.

To break up a Cooper pair, the energy deposited in the material needs to be above the gap value. There are several possible contributions to the energy of the superconducting material, like temperature rise, current or an external magnetic field. Each of these contributions influence the order parameter, which describes the phase-transition from super- to normal conduction state. In figure 3.1, the phase space is given.
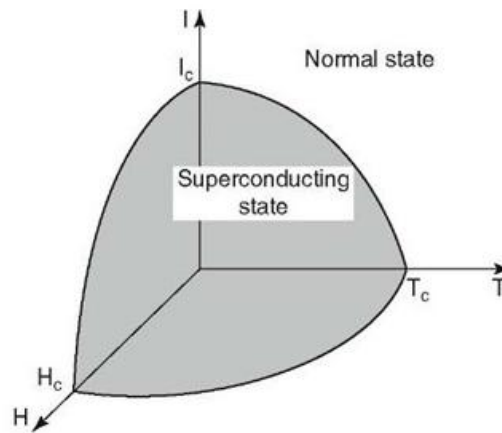
Figure 3.1: Three dimensional phase space of a superconductor. The material will stay in the superconducting phase if the current, the temperature and magnetic field are inside the volume of the shown phase space. An excess of one of the variables will lead to a breakdown of superconductivity [73].

19

Nevertheless a non-vanishing alternating current (AC) resistance exists [74]. The resistance arises due to the mass of the Cooper pairs. In an oscillating field the particles are accelerated into different directions within a period and the inertia of the Cooper pairs need to be taken into account. The formula to calculate the AC resistance R_{ac} [75], is

$$R_{ac} = R_{BCS} + R_{res} = A \frac{\omega^2}{T} exp \left(-\frac{\Delta}{k_B T} \right) + R_{res} \qquad (3.3)$$

with A including material parameters and ω describing the frequency of the applied electromagnetic field in GHz and R_{res} as the residual resistance of the material. R_{BCS} for niobium with a frequency of 1.3 GHz is about 800 nΩ at 4.2 K and drops to 15 nΩ at 2 K. The residual resistance is in the order of of 10-20 nΩ [67]. It depends on impurities of the surface exposed to the electromagnetic field and other factors, which will be discussed later in section 3.3.

3.1.2 Characteristic Lengths and Critical Parameters

In 1935, the London equations developed by the brothers Fritz and Heinz London [76] were a first attempt to describe the superconducting state. The London equations replace Ohms law in a superconductor and were able to describe the expulsion of magnetic fields from a superconductor which is cooled down below the transition temperature [77]. A new characteristic length is introduced in this set of equations, the London penetration length λ_L. It is the distance in which the magnetic field decays inside the superconductor to 1/e of its surface strength. For pure niobium this value is about 47 nm. In 1950 the Ginzburg-Landau-Theory was proposed [78]. While the BCS-theory is a microscopic theory, the Ginzburg-Landau one is a thermodynamic theory based on phase-transition.It has been shown [79] that the Ginzburg-Landau-Theory can be derived from the BCS-theory for T $\rightarrow$ T$_C$ and with the wave function in the Ginzburg-Landau-Theory describing all Cooper pairs together as a superfluid.

In this context another characteristic length arise, the coherence length ξ_{GL} which can be interpreted as the correlation distance of the two electrons of a Cooper pair. For pure niobium this value is around 64 nm and is larger than the lattice constant a $\approx$ 0.4 nm of niobium. This large overlap across the crystal lattice is the reason why all Cooper pairs can be considered as a single superfluid. The Ginzburg-Landau-Theory allows the classification of superconducting materials into two classes, namely type I and type II superconductors. Type II materials where discovered in 1936 [80] and described by Abrikosov in 1957 [81]. The free energy F of a superconducting material in an external magnetic field H_C is

$$F = \frac{\mu_0}{2} (\underbrace{\xi_{GL} H_C^2}_{\text{condensation energy}} - \underbrace{\lambda_L H_C^2}_{\text{penetration energy}}) \qquad (3.4)$$

with the condensation energy gained by condensing Cooper pairs and the penetration energy gained by intrusion of the external magnetic field. Depending on the characteristic lengths λ_L and ξ_{GL} it can be thermodynamical favored that a magnetic flux can penetrate

the material above a certain critical magnetic field $B_{C,1}$ to minimize the free energy of the system. The so called Ginzburg-Landau-parameter $\kappa = \frac{\lambda_L}{\xi_{GL}}$ allows to decided whether a material is a type I or type II superconductor.

- $\kappa < \frac{1}{\sqrt{2}} \Rightarrow$ type I - no magnetic flux penetration possible

- $\kappa > \frac{1}{\sqrt{2}} \Rightarrow$ type II - magnetic flux penetration possible (Shubnikov phase)

In figure 3.2 the phase diagram of a type I and type II superconductor is shown. Niobium
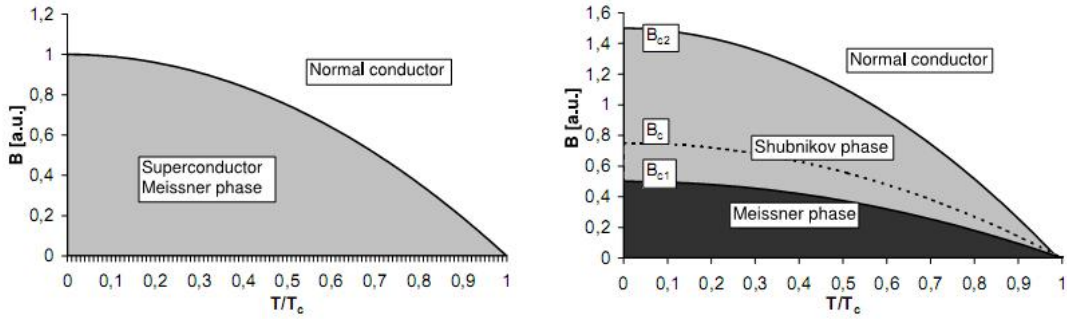
Figure 3.2: The phase space diagrams for type I (left) and type II (right) superconductor are shown. The x-axes show the normalized temperature while the y-axes depict the external magnetic field in arbitrary units. For type I superconductors, an increase above B_C will induce the normal conducting phase. For type II superconductors, magnetic vortices can penetrate the material above $B_{C,1}$ and a mixture phase of superconductivity and magnetism occurs.

is a type II superconductor with $\kappa \approx 1$ but is operated at $\frac{T}{T_C} = 0.21$. To avoid the Shubnikov-phase or a possible FFLO-state, the external magnetic field should be below $B_{C,1}$ to avoid any increase in losses.

With the Ginzburg-Landau-Theory it is also possible to derive an expression which relates the critical external magnetic field B_C to the temperature of the material

$$B_C(T) = B_C(0)\left[1 - \left(\frac{T}{T_C}\right)^2\right]. \tag{3.5}$$

As mentioned, to maintain the superconducting Meissner phase the critical magnetic field is of utmost importance. Hence, it limits the maximal accelerating field which can be applied to the surface. The critical magnetic field for niobium is 190 mT, but an excess of this value can be measured [82], where this is called superheating and the resulting value can be 20% above the thermodynamical field [83, 84]. This effect can only be observed if the frequency of the applied field has a shorter period than the relaxation time of the phase transition process, which is in this case in the order of 1 ns.

21

3.2 RF Basics

A cavity is a structure, which uses electromagnetic fields to transfer energy to the particle beam. This can be either a static or an oscillating electric field. In the latter case, the phase between the particle beam an the oscillating field needs to be adjusted and such a structure is called RF cavity.

In general, two possibilities to operate such an RF cavities are possible: As traveling wave or as standing wave cavity - a comparison can be found here [85], [86]. In the traveling wave cavity, the RF wave co-propagates with the bunch through the cavity. During this co-propagation, the energy is transfered to the bunch. Although high accelerating fields can be achieved with this method, even with reasonable cryogenic costs, a high energy spread is induced in the bunch since the wave decays as it travels along the structure. In a standing wave cavity, two RF waves are induced which generates a standing wave pattern. This lead to a high duty cycle with a long beam pattern and lower energy spread compared to the traveling wave structure. However, the accelerating field needs to be actively be corrected for energy loss due to beam loading [87] and need some time to recover before the next bunch can be injected.

3.2.1 Working Principle of RF Cavities

Particles are accelerated by high electric fields within cavities. Using static fields, a breakdown due to ionization of gas at around 1 MV/m will occur [88]. This process takes about 10^{-6} s and can be overcome by RF fields. Using the TESLA technology with a frequency of 1.3 GHz the field changes its direction every 0.76 ns and the ionization process is suppressed. In figure 3.3 a schematic view of a typical SRF cavity design for particles with $\beta = \frac{v}{c} = 1$ is shown. Other cavity designs besides the TESLA design exist, which have dif-
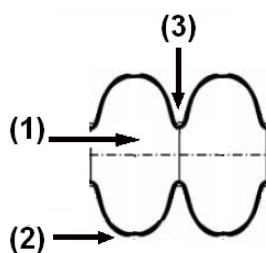
Figure 3.3: Schematic view of a two cell cavity. (1) is the cell, (2) depicts the equator and (3) the iris.

ferent advantages and disadvantages during fabrication, treatment or operation [89–92]. For XFEL, these designs are not relevant, but for ILC this topic is still of interest. Combining cavities with different shapes, where each fulfill the ILC specifications, should be considered. To guarantee a plug compatibility between different designs, the connections between different types should be standardized [93]. A first accelerator module based on this principle with cavities from different laboratories has been successfully tested [94].

3.2.2 Accelerating Field

The energy gain of a particle, traveling through a cavity, is determined by the accelerating field E_{acc}. To calculate the accelerating field along the beam axis, neglecting the magnetic component of the standing wave, the following equation is used

$$E_{acc} = \frac{1}{l} \int_{-\frac{l}{2}}^{\frac{l}{2}} E(z) \cos\left(\frac{\omega z}{c}\right) dz \qquad (3.6)$$

with l as the length of the cavity, $\omega = 2\pi f$ with f as the frequency of the RF field and E(z) the electric field along the beam axis. Furthermore, the ratio of the peak electric field at the surface to the accelerating field E_{peak}/E_{acc} and the ratio of the surface magnetic peak field to the accelerating field B_{peak}/E_{acc} are important parameters. The maximal accelerating field for TESLA-type cavities can be calculated with the B_{peak}/E_{acc} ratio, which is $4.26\frac{mT}{MV/m}$ [67]. Together with the superheating field of niobium of 228 mT, a thermodynamical limit of the accelerating field of $\approx$ 55 MV/m exist. Up till now, the highest accelerating field measured for a 9-cell TESLA cavity is a field of 45 MV/m [95]. In figure 3.4, the electric and magnetic field distribution in a TESLA cavity is shown.
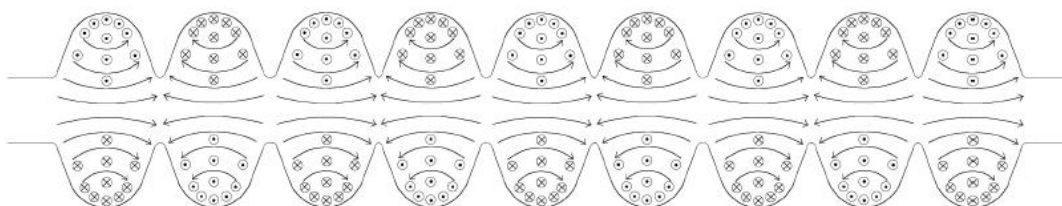
Figure 3.4: Overview of the electromagnetic field distribution in a 9-cell TESLA cavity [96]. The particle is accelerated along the cavity symmetry axis. The magnetic field is perpendicular to the electric field lines. The amplitude of the electric field shows the so called π-mode distribution.

3.2.3 Coupled Resonators and Eigenmodes

As the particles travel through a cavity they will not only see an accelerating field but they will also excite eigenmodes of the cavity by wakefields. A N-cell cavity is a coupled resonator with N fundamental eigenmodes. The higher order eigenmodes can lead to a disruptive effect on the beam and need to be damped [75]. This can already happen via the design of the cavity shape and during operation by so called higher order mode coupler (HOM coupler). These are bandpass filter attached to both sides of the cavity to couple out any eigenmode of the resonator except the one needed for acceleration.
To calculate the eigenmodes, a cavity is modeled with an equivalent circuit of a chain of coupled resonators [97, 98]. The cell to cell coupling might be electric, magnetic or a combination For TESLA cavities an electric coupling through the iris is the case.

A typical superconducting accelerating structure exist of a small number of cells N, with $N \leq 10$. This allows to calculate the frequencies of the resonant eigenmodes via

$$\omega_q = \omega_c \sqrt{1 - \frac{k}{1 + 2k}\left(1 + cos\left(\frac{q\pi}{N}\right)\right)} \qquad (3.7)$$

with ω_q as the frequency of the mode q, ω_c the frequency of the individual resonator and k the cell-to-cell coupling. The amplitude of the axial electric field in the cell is

$$A_{n,q} = A \cdot sin\left(\frac{\pi q \left(n - \frac{1}{2}\right)}{N}\right) \qquad (3.8)$$

with $A_{n,q}$ the electric field amplitude in cell n for mode q and N the number of cells. The notation of the modes reflects the phase shift per cell. The n-th mode has a n/N π phase advance per cell. For acceleration, the mode with maximal N, the so called π mode is used since for q = N in each cell the amplitude is maximal. Therefore the axial length of one cell is equal to one half wavelength of the accelerating wave and thereby establishing a phase velocity v_p of c. The number of cells is a trade off between a small and odd number of cells to avoid mode trapping in the cavity against the disadvantage of a fast cost increase of an accelerator based on short structures. For TESLA cavities, the number of cells was chosen to be nine. In figure 3.5 the relative field strength of the electric field per cell for each mode is shown. The group velocity, which is the slope of the dispersion function, is zero in the ideal case. Any loss in the cavity will create a small deviation of the phase shift of π per cell. Since losses are not avoidable, the π-mode will transport energy along the cavity structure [99] but for TESLA cavities this phase shift is neglectable since it is inverse proportional to the quality factor.

As already mentioned, higher order modes exists. The notation for the classification of these families of modes are TE and TM modes. TM modes mean, that $E \parallel z$ and $H \perp z$ and the opposite is true for TE modes. The passband mode used for acceleration, the π-mode, is a TM mode, or more specific, the TM_{010}, which is a monopole mode. The classification TM_{mnp}, with the integers m, n and p, describe the number of sign changes the electric field will undergo, when going in in the direction of ϕ, ρ and z in cylindrical coordinates. The TM_{1np} modes, for example, are called dipole modes and have a disruptive effect on the beam. They can be excited by an off-axis bunch traveling along the cavity. Nevertheless, these dipole modes can be used for beam positioning diagnostics if a passive cavity is inserted in the beam line [100].

The fact that different modes have different field strengths per cell is used as diagnostic method during the cavity acceptance test. By testing the cavity in different eigenmodes, the contributions of loss mechanism and local defects which may occur in individual cells are modulated with the relative amplitude of the regarding eigenmode. Since in each mode there is a set of cells which experience the highest field amplitude, these cells are considered to be the limiting cells in this mode. Hence a pairwise diagnostic of the cells is possible.
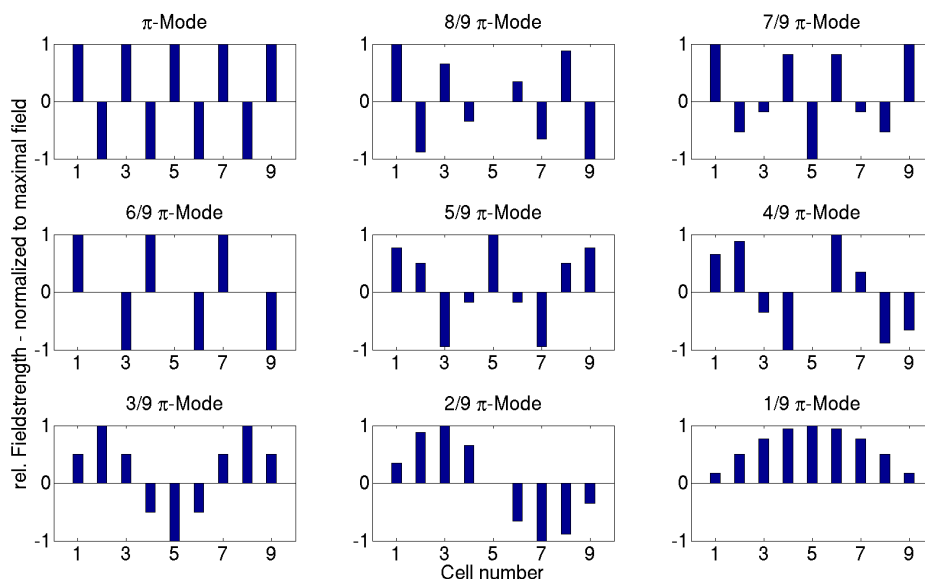
Figure 3.5: Electric field amplitudes for the passband eigenmodes of a 9-cell TESLA cavity.

3.2.4 Quality Factor and Losses

For a resonator, the quality factor is an important parameter. It is defined as

$$Q_0 = \frac{\omega U}{P} \tag{3.9}$$

with ω as the RF frequency, U represents the energy stored in the cavity and P the dissipated power into the cavity. The quality factor can be interpreted as the number of oscillations a system will perform with a given amount of energy. The total stored energy in a cavity is calculated by

$$U = \frac{\mu_0}{2} \int_V \left| \vec{H} \right|^2 dV = \frac{\varepsilon_0}{2} \int_V \left| \vec{E} \right|^2 dV \tag{3.10}$$

and the dissipated power by

$$P = \frac{R_s}{2} \int_A \left| \vec{H} \right|^2 dA \tag{3.11}$$

with R_s as the surface resistance, including all loss mechanisms, A is the cavity surface and V the cavity volume. Assuming that the surface resistance is constant over the whole surface, equation 3.9 yields to

$$Q_0 = \frac{\omega \mu_0 \int_V \left| \vec{H} \right|^2 dV}{R_s \int_A \left| \vec{H} \right|^2 dA} = \frac{G}{R_s} \tag{3.12}$$

25

with G as the geometry constant. This constant is a good parameter to compare different cavity designs since its definition is independent of material specifications and size and only depends on the shape of the cavity.

The quality factor is an important parameter, not just for cryogenic losses [101] or the low level RF (LLRF) to maintain a stable accelerating field with external perturbations [102] but also for the qualifying process of a cavity. Studying the measured Q_0 vs. E_{acc} yields a plot, which allows to extract important information about the cavity performance and its limiting process. In figure 3.6, a series of such plots with different physical limitations are given.
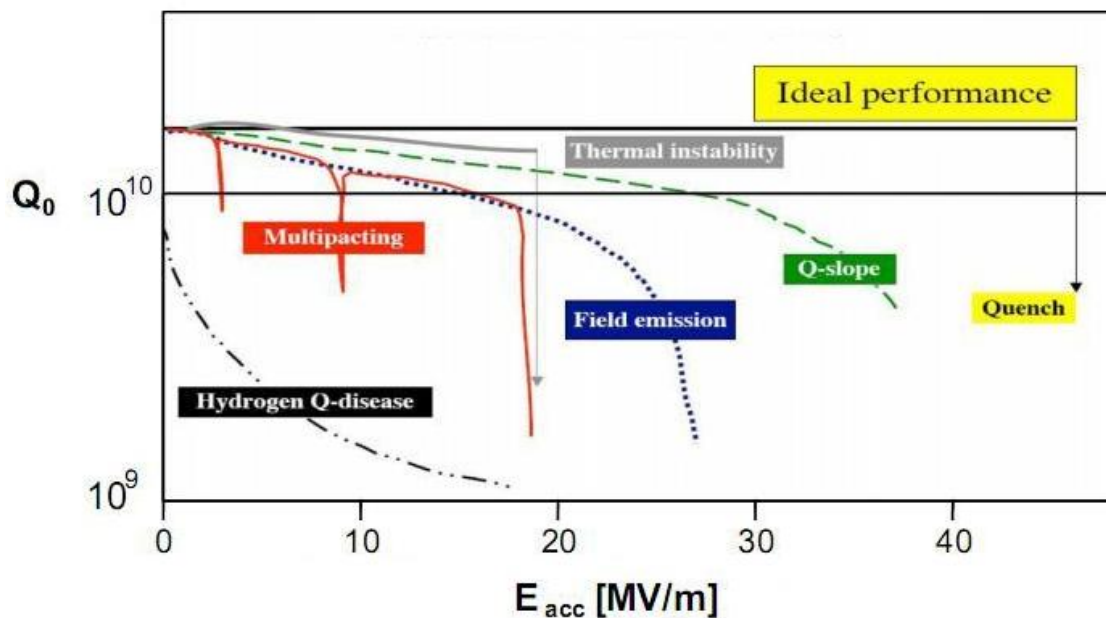

Figure 3.6: Schematic Q_0 vs. E_{acc} plot. The x-axis shows the accelerating field in MV/m and the y-axis depicts the quality factor. The theoretical performance of a TESLA cavity should be a constant quality factor up to the thermodynamical limit of 55 MV/m. This theoretical behaviour is never seen, even in a defect free cavity [103].

3.3   Performance Limitations

The RF accelerating field and the quality factor are limited by a number of mechanisms. The influence on the cavity performance of some of these mechanisms is shown in figure 3.6. An overview is given in [104, 105].

3.3.1 Multipacting

Multipacting is an abbreviation for multiple impacting and describes a resonant electron multiplication. After the impact of an electron onto the surface, one electron may create more than one secondary electron, depending on the impact energy and material. If the time of flight is a multiple integer of the RF period, an electron avalanche will be initiated. Multipacting occurs if resonant trajectories exist(c.f. figure 3.7) and if the secondary
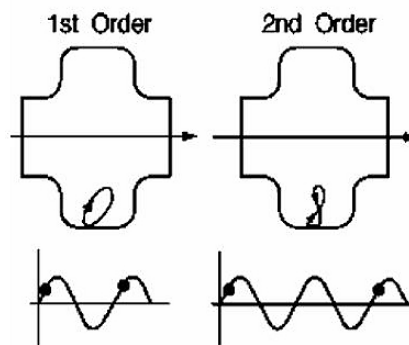
Figure 3.7: One point multipacting in a cavity of first and second order where the n-th order describes the numbers of RF periods between the impacts. Two point multipacting is the resonant travel of electrons between to distinct regions (not shown) [75].

yield δ is larger than one, which itself is a function of the impact energy and the material. The electrons absorb RF power and reduce the quality factor - furthermore the accelerating field can not be increased. To overcome this threshold and to avoid or suppress multipacting several steps are possible:

- Baking of niobium at 300 $^\circ$ C reduces the δ from 2.6 to 1.4 [106].

- An elliptical cavity design leads to a cascade of the electron along the field lines towards the equator where no further liberation of electrons will take place [107].

- Processing of the cavity during RF cold test, which means to keep the cavity at the accelerating field where the multipacting occurs and wait till this process stops. The quality factor increases to the value before multipacting.

This limitation is mostly eliminated due to the cavity design and only a minor fraction of cavities show some processing during the cold RF test.

3.3.2 Hydrogen Q-Disease

The hydrogen Q-disease is a reduction of the quality factor which starts even at low values of the applied accelerating field and is well understood [108]. The reason for this effect is a hydrogen contamination of the niobium, since niobium has a large diffusion coefficient for hydrogen [109, 110]. This contamination can be caused by many surface treatments, which is the reason why all surface chemistries are cooled to avoid a diffusion of hydrogen

into the material. Niobium and hydrogen create hydrides which lead to quality factors in the range of 10^8 which is two orders of magnitude lower than the nominal quality factor. During the RF cold test (see chapter 5.1), the cavity is kept for 10 hours in a temperature range of 80-120 K to force the creation of niobium hydrides and test for Q-Disease. This temperature range is the critical region since the hydrogen concentration and the diffusion coefficient is optimal to create hydrides [111]. If a Q-disease is detected, the cavity needs to be baked at 700-900° C and in a vacuum below 10^{-6} bar to purify the material.

3.3.3 Field Emission

Field emission (FE) is a problem, which arises when an external electric field is applied to a conducting surface. Electrons will tunnel through the surface barrier and can be captured by the applied RF field. While the tunneled electrons are accelerated, the RF field looses energy and a collision of those accelerated electrons with the cavity will deploy energy into the surface and can create a thermal breakdown of the cavity. However, the biggest problem is the occurring Bremsstrahlung, which limits the cavity performance due to safety regulations.

The theory of electron field emission was first developed for the case of DC fields [112] and is based on the quantum mechanical tunneling of conduction electrons through a modified potential barrier at an ideal and clean metal surface. As the external field is applied, the potential barrier is deformed and gains a finite thickness. The FE DC current can be expressed as

$$j(E) = C_1 \cdot \frac{E_{on}^2}{\Phi} exp\left(\frac{-C_2 \cdot \Phi^{\frac{3}{2}}}{E_{on}}\right) \tag{3.13}$$

with C_1 and C_2 as weakly material dependent constants (see [113] for the values used for analysis), E the externally field in V/m and Φ the work function of the metal in eV.

For real metal surfaces, the onset field used in this equation must be multiplied with an enhancement factor β_E [114]. The enhancement can be caused by multiple reasons like scratches and bumps, metallic or dielectric impurities, dust or grain boundary imperfections [115, 116] and lies in the range of 10-100. In [117] it is shown, that the particle size or scratch width should be smaller than 1.3 μm to reach an accelerating field of 40 MV/m, c.f. figure 3.8. To reach this goal, surface conditioning is a vital step [118]. Using ultra-clean rooms for assembly, high purity niobium for fabrication and high-pressure high-purity water rinsing for cleaning are key techniques to achieve high onset fields. During the cavity production for XFEL, field emission is the main RF limitation and reason for cavity retreatment [49].
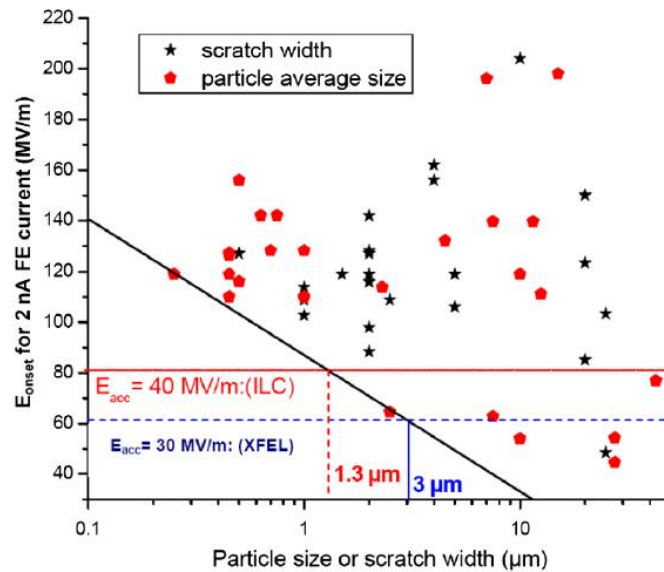
Figure 3.8: The onset electric field for 2 nA FE currents versus geometrical size of all identified emitters found on different fine grain, large grain and single crystal niobium samples [117]. The electric surface field is related to the accelerating field E_{acc} by a design depended constant, see table 4.1.

3.3.4 Thermal Breakdown

A local phase transition from the superconducting to the normal conducting phase, which triggers a global thermal breakdown is called a quench. It limits the cavity performance and can occur at any accelerating field. The mechanisms behind a quench can be classified as either a [119, 120]

- thermal quench due to resistive heating, of e.g. a normal conducting defect. The breakdown threshold is proportional to H^2 due to joule heating, see figure 3.9.

- magnetic quench due to geometrical defect which leads to a field enhancement and a local rise of the magnetic field above the critical magnetic field. The breakdown threshold is proportional to H.

Several analytical approaches to relate defect geometries and the corresponding quench field were done [121–124] and simulations of quench dynamics are described in [125–127]. It is well known, that a larger defect leads to a lower breakdown threshold [122,123], although it is not necessary to have an optical detectable large defect for a low quench field.

In general, it is more likely for quenches to occur at the equator region where magnetic field has its highest value and the welding procedure and resulting geometry fosters quench origins. A higher thermal conductivity increases the breakdown field [128] which depends on the purity of the used material. Furthermore, thermal conductivity shows a dependence on the grain size of niobium, since the grain size determines the mean free

29
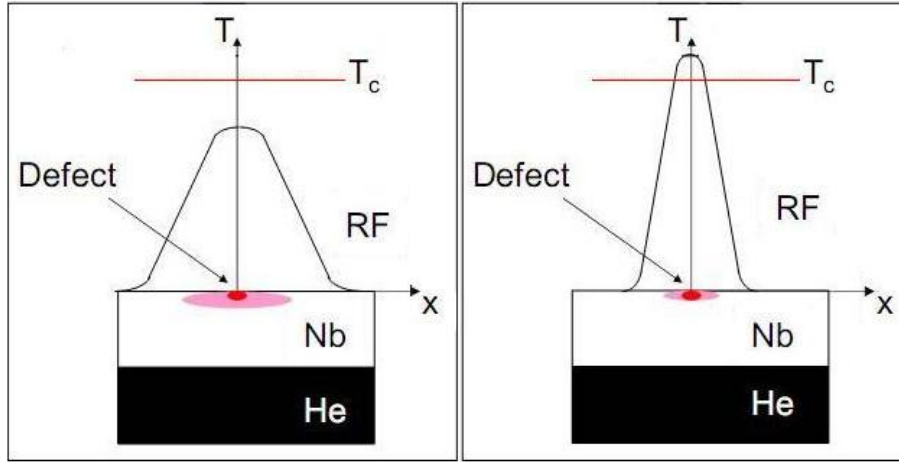
Figure 3.9: A schematic view of a thermal quench. On the left, a normal conducting defect (red) is surrounded by a heated niobium surface (light red). As long as the thermal conductivity is sufficient to dissipate the deployed energy into the helium bath (black), the cavity will not quench. At a higher field (right), the dissipation process can not transfer the amount of deployed energy and the temperature rises locally above the critical temperature. The local phase transition will now trigger a quench [75].

path for phonon scattering [129, 130]. Given the various reasons and mechanism for a quench, it is hard to single out optical properties of a region which will lead to a quench.

3.3.5 Q-slope

Besides the mentioned limitations in the cavity performance, an obvious deviation from the theoretically expected behaviour is the so called Q-slope. With given BCS-theory, a constant quality factor, independent of the applied accelerating field, is expected. But even in defect free cavities, a decrease of the quality factor with increasing accelerating field is observed. This behaviour is called Q-slope, as it can be seen in figure 3.6.
An overview of different models which try to explain the observed Q-slope, their possibilities and limitations is given in [105, 131] and in general, although the complete mechanism is not known yet, it is assumed that the grain boundaries play a crucial role in causing the Q-slope.

Magnetic Field Enhancement
The magnetic field enhancement model (MFE) assumes that the magnetic field locally exceeds the critical magnetic field due to field enhancements of the micro structures on the surface [132–134]. The magnetic field enhancement factor β_m of a step depends on the geometry and a grain boundary becomes normal conducting when $\beta_m H \geq H_{crit}$ where H is the surface magnetic field. An estimate of the power dissipated per length by this normal conducting grain boundary is

$$\dot{Q}^l_{diss} \approx -\frac{1}{2} R_{nc} w_{nc} \left(\beta_m H \right)^2 \tag{3.14}$$

if $\beta_m H \geq H_{crit}$. With R_{nc} as the surface resistance of normal conducting niobium and w_{nc} represents the width of the region of the grain boundary that is in the normal conducting state, see figure 3.10. With this model, requirements concerning the β_m can be calculated,
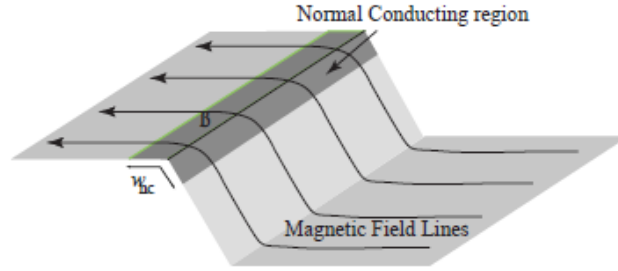

Figure 3.10: Schematic view of a quenched grain boundary due to magnetic field enhancement. The normal conducting region will decrease the quality factor, although the cavity itself will stay superconducting [132].

for the merit of achieving a certain accelerating field before the Q-slope takes place. Assuming a Gaussian distribution of the enhancement with a $\sigma \ll 1$ and a mean β_m of 2.5, an accelerating field of 20 MV/m can be reached before the Q-slope starts. With a mean value of 1.6 for β_m, an accelerating field of 30 MV/m is possible.

With the help of geometrical properties of a boundary, the magnetic enhancement factor can be calculated via

$$\beta_m = \left(\frac{r}{R}\right)^n \tag{3.15}$$

with r the bending radius of the boundary and R the radius the symmetric boundary and n $= -\frac{1}{3}$ for small r/R and -0.28 for larger values, see figure 3.11. The effective radius of the edge is limited to 2.4δ with δ as the RF skin depth [132] and is about 1 μm. This model
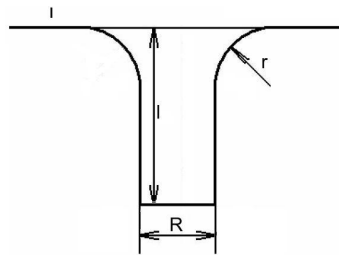
Figure 3.11: Geometrical parameters of a hole [133]. The bending radius r and the radius R are used to calculate the magnetic field enhancement.

explains in general the Q-slope appearance at cavities and the flat Q in seamless cavities. But it also predicts different Q-slopes for BCP and EP cavities, which is not the case. In [105] it is discussed, that a smaller Q-slope after mild baking can be explained with the model. And it is possible that, if the orientation of each grain and its enhancement factor is known, a better differentiation between BCP and EP cavities will be possible.

Element	O	N	C	H	Ta
$\frac{\Delta\rho}{\Delta C}\left[10^{-11}\Omega\text{m/wt.ppm}\right]$	2.64	3.49	3.33	0.8	0.12

Table 3.1: Residual resistance coefficient for different elements in niobium [147,148].

Flux Pinning

If the accelerating field is increased above a certain on-set field level, magnetic flux can penetrate the cavity and create an additional RF loss term R_{fl} [135,136]

$$R_{fl} \propto \ell^4 \rho_n B_{ext} \qquad (3.16)$$

with ℓ as the mean free path of the material, ρ_n the normal state resistivity and B_{ext} the external magnetic field. The on-set field for the penetration can be influenced and suppressed by geometrical defects and grain boundaries [137,138]. Hence, depending on the individual boundary shape, an increase in the accelerating field should create additional losses and therefore reduce the quality factor.

It is still not clear if the flux penetration is fast enough to penetrate the material during a single RF period. In [83], the penetration velocity is calculated to be in the order of 42.5 m/s. Hence, the time to penetrate the cavity with a wall thickness of 2.8 mm is 66 μm. This value is several magnitudes larger than the timescale for a RF cycle. In [139] it is argued that within a RF cycle a penetration depth of about 30 nm can be achieved, which is already in the order of λ_L could influence the cavity performance.

Diffusion at Grain Boundaries

It has been shown that impurities prefer to diffuse and aggregate at grain boundaries [140–145]. Any impurity can have a significant influence onto the cavity performance, e.g. via the electrical resistivity, which consists of two terms. A temperature independent, material dependent residual resistance ρ_{res} and a resistance based on electron-phonon scattering ρ_{phonon}.

$$\rho(T) = \rho_{res} + \rho_{phonon}(T) \qquad (3.17)$$

where $\rho_{phonon}(300K) = 1.46 \cdot 10^{-7}\Omega\text{m}$ and $\rho_{phonon}(4.2K) = 8.7 \cdot 10^{-11}\Omega\text{m}$ [146]. The residual resistance is dominated by the scattering of the electrons on interstitial atoms, where the individual element contributions can be calculated via

$$\rho_{res} = \sum_i \left(\frac{\Delta\rho}{\Delta C}\right)_i C_i \qquad (3.18)$$

with C_i as the concentration of the element in the niobium. Coefficients of the most important interstitials are given in table 3.1.

Although tantalum has the smallest influence onto the residual resistance, a locally high density would result in a normal conducting region and is a seed for a thermal breakdown. A discussion of the allowed interstitial concentrations is given in table 4.2 in section

4.1.1. The influence of interstitials on the performance has been found to be an interesting research field due to current research results [149]. But it is already known, that any change in the RRR and thereby the thermal conductivity, will influence the losses. The effective diffusion coefficient, including lattice and grain boundary diffusion, shows an inverse dependency on the grain size [144,145], which should allow to discuss differences between fine grain and large grain cavities.

Grain Boundary as Weak Link
Another possible contribution to the loss mechanisms, is the interpretation of the grain boundary as a weak link in a superconductor and that the surface would consists of many Josephson Contacts [150], where the loss term is given by

$$G = \rho_{gb}a^2 \tag{3.19}$$

with G as the specific resistance, ρ_{gb} the normal state resistivity of the grain boundaries and a as the area of the grain boundary. A dissipation will only occur above a certain critical current I_C across the junction, which is related to the specific resistance via

$$I_C = \frac{\omega h}{2eG} \tag{3.20}$$

where ω is the applied RF field frequency, e the elementary charge and h the Planck constant. Studies showed [151],that the resistance of a grain boundary is in the order of $\bar{G} = 2.10^{-13}\Omega m^2$ which is 1000 times higher than the bulk value [152], which is in agreement with the theory [153]. The current can be related to a magnetic field at which the resistance is turned on. Although this magnetic field is B_{gb} = 125 T, which is much higher than the operating field within a cavity, any contaminations at the grain boundaries can suppress this value and can lead to an additional loss mechanism and lead to a higher Q-slope.

CHAPTER 4

Cavity Fabrication and Surface Treatment

The superconducting cavity design, developed for the TESLA accelerator was adapted for XFEL with minor changes due to restrictions concerning mechanical, safety and production aspects. Detailed descriptions on each fabrication and preparation step can be found elsewhere [34, 139, 154–157] and only a short overview with important aspects for this thesis is given here.

4.1 Cavity Fabrication

The 1.3 GHz standing wave cavity is produced from solid niobium and bath-cooled with superfluid helium at 2 K. Each cavity is equipped with a helium tank, a tuning system against Lorentz Force detuning, power coupler, pick up probe and two HOM couplers. In figure 4.1 a side view of a cavity is shown and in table 4.1 the parameters of the cavity are summarized.
The fabrication and preparation process developed over years [42] has been implemented at two vendors for XFEL. An detailed overview of the complete chain is given in [34,154].

4.1.1 Niobium

Niobium was introduced as material for superconducting cavities in 1967. It has the highest critical temperature and critical magnetic field of pure metals, is chemical inert and has the needed mechanical properties for deep drawing of the half-cells. An detailed overview of the material studies performed in the light of SRF applications and the development of treatments and quality assurance of niobium is given in [158]. The production of high purity niobium begins with niobium ingots melted by electron beam or electro-arc melting. The ingot has a diameter of about 300 mm and a length between 800-2000 mm. A further refining is achieved by re-melting the niobium ingot in vacuum at $2500°$ C.
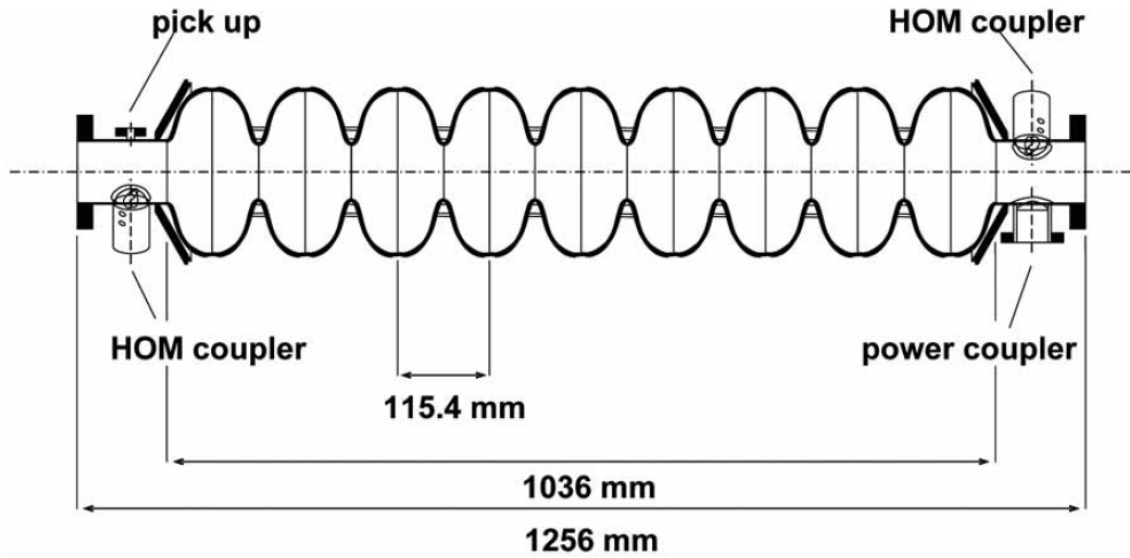
Figure 4.1: Schematic view of the nine cell cavity with main power coupler, pick up probe and two HOM couplers [34].

Type of accelerating structure		standing wave
Accelerating mode		TM_{010},π-mode
Fundamental frequency	[MHz]	1300
Thermodynamical max. Gradient	[MV/m]	≈ 55
Quality factor		$>10^{10}$
Active Length	[m]	1.038
Cell-to-cell coupling	$k_{cc}[\%]$	1.87
Iris diameter	[mm]	70
Equator diameter	[mm]	206.6
Geometry factor G	[Ω]	270
Shunt impedance R/Q	[Ω]	1024
E_{peak}/E_{acc}		2.0
B_{peak}/E_{acc}	[mT/(MV/m)]	4.26
tuning range	[kHz]	± 300
$\Delta f/\Delta L$	[kHz/mm]	315
Lorentz force detuning constant	[Hz/$((MV)/m)^2$]	1

Table 4.1: TESLA cavity design parameters [34,67]

Chemical Purity

A quantity for the purity of a material is the residual resistivity ratio (RRR). It is defined as

$$\text{RRR} = \frac{\rho\,(295K)}{\rho\,(4.2K)} \tag{4.1}$$

with ρ as the electrical resistivity at the given temperature. The electrical resistivity at temperatures close to 0 K strongly depends on impurities, lattice defects and grain boundaries while any electron-phonon scattering can be neglected [148, 159, 160]. The mean free path (mfp) is a direct consequence of the purity and therefore of the RRR and has a huge influence on the BCS resistance. In figure 4.2, the dependency of the BCS on the mfp of the electron is shown. An explanation of this behaviour can be found by studying
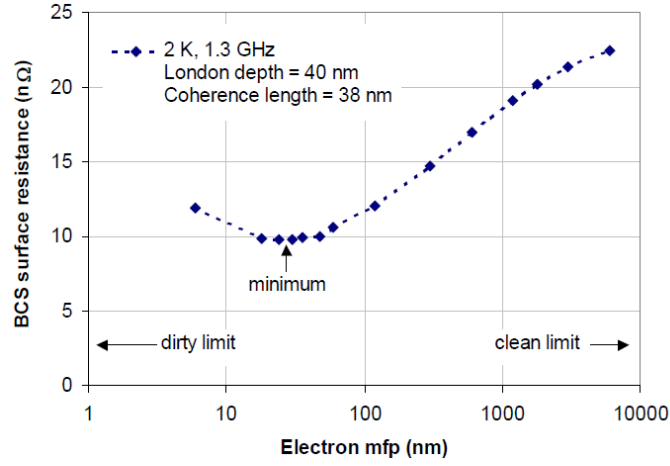
Figure 4.2: BCS resistance as a function of the mean free path. A minimum is observed at $\ell \approx \xi$ which equals and RRR of 10. [105]

the influence of two length scales, the mean free path ℓ and the coherence length ξ of the Cooper pairs, onto the BCS resistance.

- $\ell \ll \xi$, 'dirty limit':
  In the dirty limit, the surface resistance is dominated by impurity scattering. The surface resistance R_S is proportional to [75, 161]

$$R_S \propto \sigma_n \lambda^3$$

  with σ_n as normal conducting Drude resistivity, which is $\propto \ell$ and λ as penetration depth, which is $\propto \ell^{-\frac{3}{2}}$. Hence, $R_S \propto \ell \times \ell^{-\frac{3}{2}} \propto \ell^{-\frac{1}{2}}$. This means, that the surface resistance decrease with increasing mean free path and the superconductor behaves like a normal conducting material.

- $\ell \gg \xi$, 'clean limit':
  As the mean free path increase and gets larger than the coherence length, the BCS resistance becomes independent of the impurity scattering. The electrons scatters

on the penetrated magnetic field, where the relevant length scale is the London penetration depth and replaces the mean free path in the formula for the surface resistance. This means, that $\sigma_n \propto \lambda_L$ and $\lambda \propto \lambda_L$ and $R_S \propto \lambda_L^4$, which is analog to the anomalous skin effect in metals [74]. A further purification does not improve the surface resistance.

Although, a further purification of niobium does not improve the surface resistance, it has a significant influence on the thermal conductivity κ, which is proportional to the RRR [75, 162]. The RRR for SRF cavities is about 300 and the purity requirements of the interstitials are shown in table 4.2. Several remeltings of the niobium ingot in

	$[\mu g/g]$		$[\mu g/g]$
Ta	≤ 500	Ni	≤ 50
W	≤ 50	O	≤ 10
Mo	≤ 50	N	≤ 10
Ti	≤ 50	C	≤ 10
Fe	≤ 50	H	≤ 2

Table 4.2: Impurity content specifications for XFEL cavities [34].

ultra high vacuum is needed to achieve these specifications. After this step, sheets with a thickness of 2.8 mm are produced. This is either done by directly cutting of the ingot [163] which yields so called large grain material, or the ingot material undergoes a mechanical production chain like forging, rolling, folding and polishing which yields into so called fine grain material. Large grain material has grain sizes in the order of several centimeters while fine grain material will result in grain sizes in the order of a few 10 µm.

To assure the high purity after mechanical fabrication of the sheets, an eddy current scan device has been developed which scans each sheet before further fabrication steps are performed [157, 164, 165], and in general, the industry is capable to realize such high purity and to assure its quality [166]. After forging and sheet rolling, the 2.8 mm sheets are degreased, a 5 µm etching is applied and an annealing of 1-2 h at 700-800° C in a vacuum oven takes place. The latter is needed for full recrystallization and a grain size of 50 µm. The mechanical properties needed for further fabrication is sensitive to the grain size and lattice defects.

Grain Size

The grain size does not remain constant during further fabrication steps. During the welding procedure, the material will melt and new grains will form and beyond the welding seam, grain growth in the heat affected zone will occur. This means, that only the bulk region will maintain the original grain size of 50 µm, while the other regions will show larger grain sizes. The average values for the observed grain sizes in these region are given in table 4.3. Although the cavities for XFEL are fine grain cavities, an R&D program for large grain cavities at DESY was set up [169]. Large grain cavities have less

	Bulk	Heat Affected Zone	Welding Seam
Grain Size	50 μm	100-500 μm	0.1-2 mm

Table 4.3: Grain size in different regions of the cavity surface [167,168].

grain boundaries and therefore a lower probability for impurities and other loss mechanisms. Furthermore, a simple buffered chemical polishing (BCP) could be sufficient for a smoother surface [170]. To study these topics, eleven large grain cavities were produced. The resulting accelerating fields were, in average, 5-7 MV/m higher than fine grain cavities with the same treatment were able to deliver. Furthermore the quality factor was higher by a factor of two [155, 169, 171] and with AC155, the highest accelerating field of 44.5 MV/m in a 9-cell TESLA cavity was measured up to date [95]. Nevertheless, the large scale fabrication of large grain cavities has still some issues. Fine grain cavities show a random distribution of crystal orientations while this is not true at large grain cavities. This can lead to steep steps at the grain boundaries and half-cell shape deviations due to preferred slipping of the main atom planes [171].

4.1.2 Fabrication and Tuning

After quality control, the 2.8 mm thick niobium sheets are deep drawn to form half-cells. The dies are made of high yield strength aluminum alloy. Some further forming is needed to achieve the curvature needed at the iris and an tuning length of 1 mm is added at the equator for later tuning to the right frequency. The mechanical specification for the material is given in table 4.4.

Grain Size	[μm]	≈ 50
Yield Strength	[N/mm^2]	> 50
Tensile Strength	[N/mm^2]	> 140
Elongation at fracture	[%]	> 30
Hardness (Vickers)		≤ 60

Table 4.4: Mechanical specifications for XFEL cavities [34].

The shape of the half-cells is controlled by a frequency measurement [172, 173]. After cleaning of the half-cells, two of them are welded at the iris with an electronbeam weld (EBW) and form a so called dumbbell. It is preferably to do all welding from the inside if possible. Niobium is a strong oxygen getter, therefore the weldings has to be performed in a vacuum better hen $7 \cdot 10^{-8}$ bar [174]. The stiffening rings are welded after this step and the frequency of the dumbbells are measured. A way to achieve smooth welding seams at the equator, it the use of an elliptical or rhombic weave bead pattern with 50% beam power at the first pass and 100% beam power at the second pass to ensure full penetration. To achieve full penetration of a 1.6 mm thick niobium sheet, a voltage of 50

kV, a current of 37 A and a beam velocity of 46 cm/min should be used [174]. But these parameters and the weave bead can differ, which is the case for the two vendors of cavitiy for the XFEL production. The weave bead is created when the electron beam performs a side-to-side motion in addition to the linear movement to make the weld. This side-to-side motion insures a fully penetrated welding seam over the whole region and also reduces the height of the weld bead by "spreading it out" which allows the metal to cool faster than if the heat were concentrated in a straight-line stringer bead. The combination of the linear movement, with the feed rate as important parameter, and the side-to-side movement, defined by a vendor specific pattern, is the cause for the vendor specific grain boundary orientation. The properties and the microstructure of the niobium after the EBW is from uttermost significance for the cavity performance and is an important R&D topic [175, 176].

After the fabrication of a 9-cell cavity and a first surface removal, the field flatness and the operating frequency need to be assured. To reach this goal, an automating tuning machine has been developed, based on an iterative algorithm [177, 178]. It measures the field strength and frequency in each cell and by applying mechanical pressure and tension, each cell is tuned. The cavity is slightly detuned before the surface treatment since the removal of several hundreds of μm during surface polishing would change the volume and therefore the resonance frequency. This removal needs to be taken into account during tuning.

4.2   Cavity Treatment

The key to reach high accelerating fields and quality factor is a smooth and clean surface. Several techniques to achieve this goal have been developed over the past decades. The standard process flow for the XFEL can be seen in figure 4.3 and the procedure is described in [34, 154]. In a first step a layer of (110 - 140) μm of the inner surface is removed, the so called damage layer. This is done to remove any remanent scratches which occurred during machining and to remove the oxide layer of natural Nb_2O_5, which has a thickness of about 5 μm. An outside etching of the surface to improve the thermal conductivity and cooling efficiency follows. Below the Nb_2O_5 oxide layer, other oxides and sub-oxides can be found [179, 180].The standard surface polishing procedures are the buffered chemical polishing (BCP) and the electropolishing (EP). Although the set of treatment steps yield similar results and gradient spread across many laboratories, a substantial variation in details exist. In this section, the procedures as performed during the XFEL production are described.

Final EP Scheme **BCP Flash Scheme**

Cavity after equator welding

EP 110μm → Short high pressure water rinse ← EP 140μm

Outside etching by BCP 20μm

Ethanol rinse

800°C annealing

EP 40μm ← Cavity tuning → Flange assembly

Standard high pressure water rinse — Standard high pressure water rinse

Flange assembly — Assembly of accessories — Helium tank welding

Ethanol rinse — 6x standard high pressure water rinse — BCP 10μm

6x standard high pressure water rinse — 120°C baking (not for all cavities) — Standard high pressure water rinse

Helium tank welding — HOM coupler tuning

Assembly cavity to test insert

Vertical acceptance test

Figure 4.3: Process flow of surface treatment for cavities including helium vessel welding. The two different flows are for EP and for BCP preparation cycles. [154].

4.2.1 Buffered Chemical Polishing

Because Nb_2O_5 is chemically inert, only hydrofluoric acid (HF) can dissolve it. After the dissolution a re-oxidation of the niobium by an oxidizing agent is done. In this case it is nitricid acid HNO_3. The mixture of HF (mass fraction w = 40%) and HNO_3 (w = 65%) is strongly exothermic and induces a removal rate of 30 μm niobium per minute. The exothermic reaction can lead to a thermal runaway and large quantities of gases are produced. Therefore a buffer substance is added, H_3PO_4 (w = 85%) [181] and a cooling of the mixture to 15° C is performed. This reduces the migration of hydrogen into the niobium [182, 183]. The DESY standard procedure contains a mixture of 1 volumepart HF, 1 volumepart HNO_3 and 2 volumeparts H_3PO_4 and results in a removal rate of 1 μm per minute [184].

4.2.2 Electropolishing

Electropolishing (EP) of materials was introduced in 1939 [185, 186] and its first application on cavities was made at CERN together with Karlsruhe [187] using a pulsed current. The first use of EP for TESLA cavities was developed at KEK [188]. A setup for a horizontal EP was established at DESY in 2001 [139, 189]. In figure 4.4 a schematic view of a single-cell setup is shown. The acid mixture is 1 volumepart HF (w = 40%)
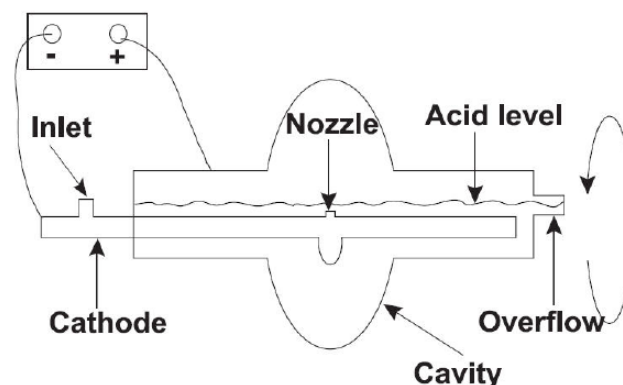
Figure 4.4: Schematic for horizontal EP. A membrane pump drives the acid mixture through a cooling and filtering system. From there it reaches the inlet in the aluminum cathode and fills the inside of the cavity. The acid flows back into the system via an overflow. At the end of the treatment, the cavity must be tilted to remove the complete acid. [189].

and 9 volumeparts H_2SO_4 (w = 98%). The chemical redox reaction (detailed discussion in [190, 191]) is driven by an external power source, where the volage is held between 15-18V and the current at 300 A. The voltage is steered to keep a temperature of 35° C. The cavity rotates with 1 rpm since the cavity is only filled till 60% of the volume, while the acid flow is 5 l/s. The resulting removal rate is about 0.5 μm. The generated hydrogen gas can flow to the surface and is swept out by a nitrogen gas flow. To prevent the

hydrogen to mix with the electrolyte, the aluminium cathode is surrounded by perforated teflon. Up till now, no complete theory of EP of niobium cavities exist, but the assumption is that since the electric field is higher at edges than in craters and therefore the removal rate is higher there. This effect smoothes steeper slopes and grain boundaries. To remove sulfur remanents, an alcohol rinsing is needed after the EP. It is general acknowledged that EP treated cavities can reach higher accelerating fields than BCP cavities and it has been found that BCP cavities show an average a maximum field of 30 MV/m - with some exceptions [184, 192]. A possible reason for this is the smaller average surface roughness of 0.5 µm at EP cavities than the 1-5 µm at BCP cavities [75], see figure 4.5. For XFEL,
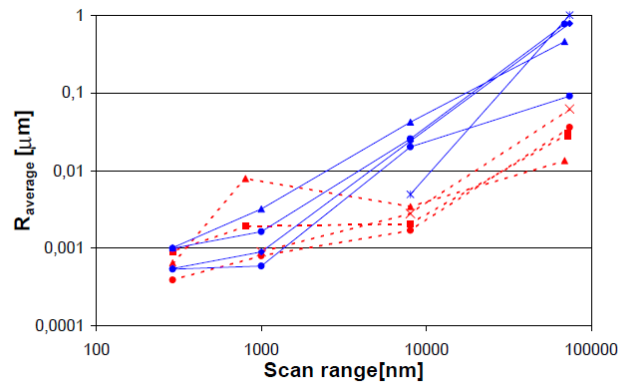
Figure 4.5: The average roughness as a function of the scan length, measured with an AFM. Cavities with EP are the red dotted lines, cavities treated with BCP are the blue full lines. The average roughness for small length scales (smaller than fine grain size) shows no difference while for larger length scales the roughness of EP cavities are about a magnitude smaller. [184].

both surface treatments are valid processes.

4.2.3   Cavity Baking

For best high field performances, cavities are 'in-situ' baked [193, 194] to further improve the chemical composition of the near-surface layer. Two kind of baking procedures are part of the standard fabrication.

800°C baking
Although the purity of the niobium sheets is thoroughly controlled, the chemical surface treatments will introduce chemical interstitials, mainly hydrogen, into the material. To degas these interstitials, the cavity is baked in an ultra high vacuum furnace at 800 °C for 2 hours. Another feature of this treatment is the release of mechanical stress introduced during the mechanical fabrication.

120°C baking

The cavity qualification procedure, see section 5.1 for details, showed exponentially increasing RF losses above 20 MV/m [195], see figure 4.6 for an example. This effect is named Q-drop and up till now, no complete understanding of this effect has been achieved. To reduce this problem, an empirical solution has been found. Baking a cavity for 48 h at 120 °C has been proven to cure this problem most effectively. The most likely reason, why this works is the decrease of the mfp due to a diffusion of oxygen from near the surface (penetration depth of about 10 nm before baking) into the material (penetration depth of about 40 nm after baking) which result in a lower surface resistance and with it a reduction of the Q-drop.
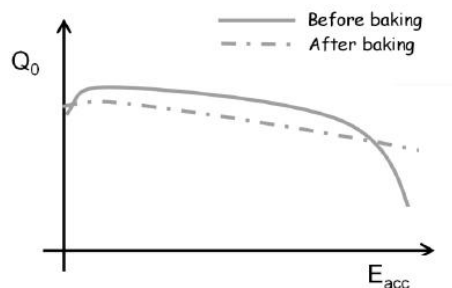
Figure 4.6: This schematic sketch shows two Q vs E curves of the same cavity. One depicts the curve progression before and one after baking [168]. A sudden increase of losses at high fields is visible, which is then removed after baking.

4.2.4 High Pressure Rinsing

A simple step but effective in improving the surface cleanliness is high pressure rinsing. A lance is inserted into the cavity with eight nozzles in a rotational symmetric pattern. Through these nozzles, high pressure water jets with ultra pure water and a pressure in the order of 100 bar are directed onto the inner cavity surface [196]. This procedure is proved to remove dust and particles from the inner surface of the cavity, which can be proven by particle counters in the used water. The standard fabrication procedure includes repeating the HPR for four times to reduce the particles counts inside the cavity. Up till now, HPR has been proven to be the most effective retreatment in the XFEL production scheme [49].

CHAPTER 5

Cavity Performance Diagnostics

This chapter describes the diagnostic standard methods available for a nondestructive analysis of SRF cavities. The most crucial method is the so called cold RF test in which a cavity is cooled down to the operational temperature and its reaction to RF signals are studied. To expand the information gained by this method, additional methods were developed, which run in parallel during the cold RF test.

All those methods will be introduced and several aspects, which will be needed for this thesis, will be discussed in detail.

5.1   Cold RF Test

The aim of such a test, is to measure the losses of a cavity as a function of the applied accelerating field, since they are of crucial interest for the diagnostics and understanding of cavity behaviour. A schematic drawing of a vertical test stand at DESY can be seen in figure 5.1. The cavity is mounted into a test insert, which consists of a support frame with vacuum connectors and feedthroughs for RF cables. The insert is installed into a cryostat, which shields the earth magnetic field. Inside the cryostat, the vacuum is tested and afterwards the cavity is cooled down with liquid helium to 2 K [197, 198].

45

Figure 5.1: Schematic view of the vertical test stand at DESY [96]. For a better overview, only a single cell cavity is shown.

The measurement system is driven by a frequency generator, which is set to the resonant frequency of the mode under investigation. The driving signal is controlled with a pin diode, to toggle the input power, and fed into a continuous wave amplifier. The amplified signal P_{for} is transmitted to the cavity, where a certain fraction of the signal is reflected at the cavity input P_{ref}. As the standing wave inside the cavity builds up, a fraction of this power is coupled out, P_{trans}, and is used for the phase locked loop (PLL). The need for a PLL is due to the sharp resonance peak of only a few hundred Hz. The exact position of this sharp resonance can change by mechanical vibrations, so called microphonics, which are transfered to the cavity by pressure waves in the liquid helium. Hence the generated frequency is adjusted dynamically to follow these deviations via the PLL. An overview of the RF circuit is given in figure 5.2.
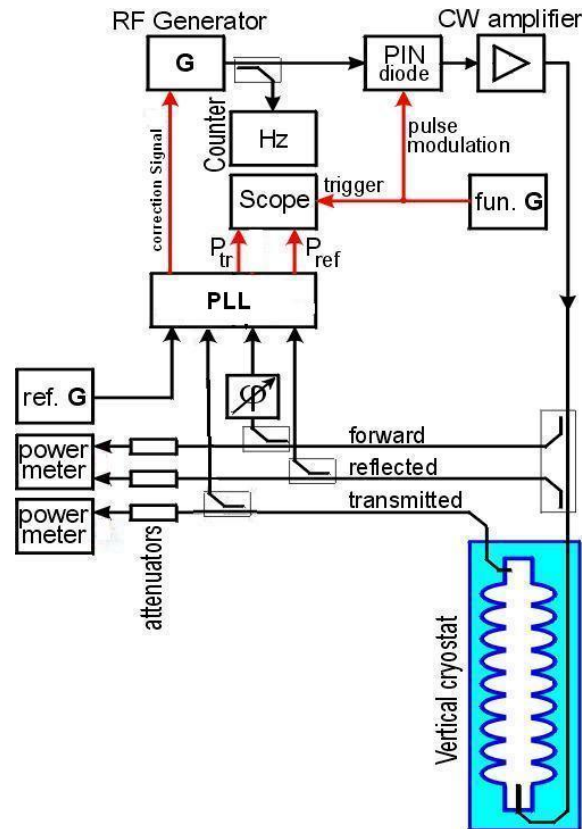
Figure 5.2: Schematic RF circuit of the vertical test stand at DESY [199].

As the rectangular shaped forward power P_{for} is feed to the cavity, the cavity reacts to the signal. The reflected power P_{ref} in figure 5.3 shows different matchings of the transmission lines to the cavity. The transformation ratio is described by the coupling factor β. This factor β is the ratio of the resistor R in the LCR-cavity-equivalent circuit to the external load. Several formulas to calculate the coupling exist [75, 200]. For the case that

the field within the cavity saturates, β can be calculated via

$$\beta = \frac{1 - \sqrt{\frac{P_{ref}}{P_{for}}}}{1 + \sqrt{\frac{P_{ref}}{P_{for}}}}. \tag{5.1}$$

The cavity transient time τ_L is the time response of the cavity and defines the time needed for the filling of the cavity as well as the power decay after switching off the RF signal. This process shows an exponential behaviour and τ_L is defined as that time, in which the reference signal decays to P_{ref}/e. The power dissipated inside the cavity P_{diss}, which is needed to calculate the accelerating field, can be derived by simple power balance

$$P_{diss} = P_{for} - P_{ref} - P_{trans}. \tag{5.2}$$

The decay time of the cavity is directly related to the losses of the cavity and therefore to the quality factor of the system Q_L, including all antennas and couplers. The quality factor Q_L is related to the transient time via

$$Q_L = \frac{1}{2}\omega\tau_L \tag{5.3}$$

with ω as the resonance frequency of the cavity. The decay time is found by an exponential fit to the decaying power. The unloaded quality factor Q_0 of the cavity, which contains only surface loss mechanisms and is the variable of interest, is related to Q_L via

$$Q_0 = (1 + \beta) Q_L. \tag{5.4}$$

The corresponding accelerating field E_{acc} can be calculated with the following equation

$$E_{acc} = \frac{\sqrt{\frac{R}{Q} \cdot Q_0 \cdot P_{Diss}}}{nl} \tag{5.5}$$

with l as active acceleration length of a cell, n as the number of cells and $\frac{R}{Q}$ as the shunt impedance of the cavity which is a measure of how effective the applied energy is translated into an accelerating field. An detailed estimation of the systematic uncertainties can be found in [201–203], but in general, the relative uncertainty for the unloaded quality factor is in the order of 5% and the relative uncertainty for the accelerating field is in the order of 10%.

5.2 Temperature Mapping

For a spatial investigation of thermal breakdowns, a temperature mapping (T-map) system was developed at KEK [204]. It consists of small thermal dependent resistors attached to the cavity surface with a spring connected to a DAQ-system. If a thermal breakdown occurs, it leads to a local heating of the inner cavity surface and dissipated to the outer
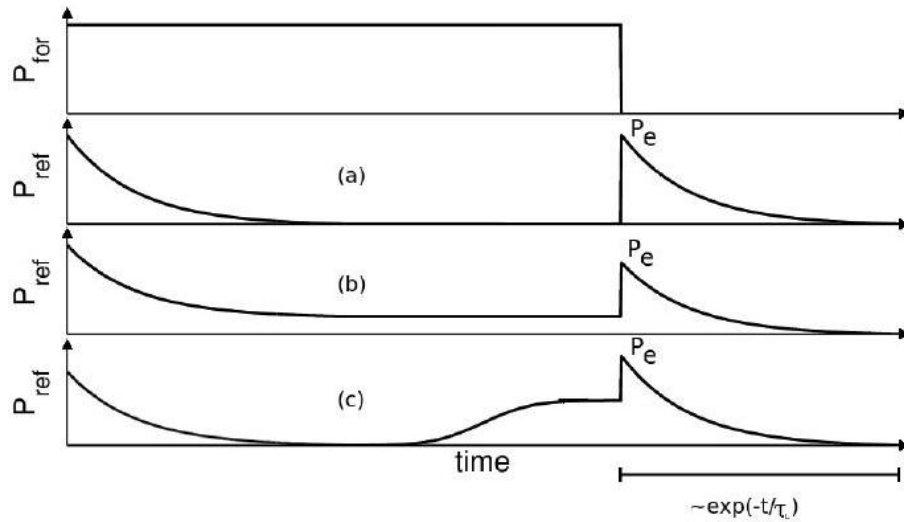
Figure 5.3: The plots show the power signals as a function of time. The upper plot shows the forward power on the same time scale as the reflecting powers in (a-c). The first peak in the reflected power is the complete reflection of the incoming forward power signal. The second peak is the leakage of the standing wave out of the cavity after the forward power is turned off. (a) shows the critical coupling with $\beta = 1$. The peaks have equal height. (b) is the undercoupled and (c) the overcoupled case. [75].
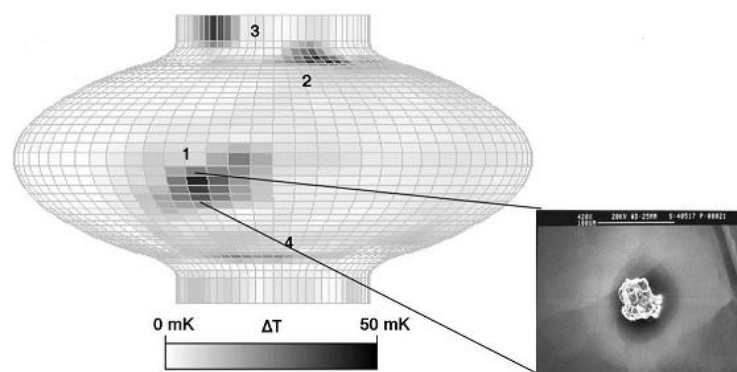
Figure 5.4: Temperature map of a 1.5 GHz single cell cavity. The heating at the quench site (1) and field emissions at (2-4) is shown. A SEM picture of the RF surface taken at the quench site is shown at the right [205].

surface. The thermal resistors will change its signal output and this signal can be temporarily and spatially resolved. An example is shown in 5.4. The spatial resolution of T-map systems is given by resistor size and spacing and is in the order of 1 cm. The assembly of the T-map system is time consuming and is only done after a quench occurred at a previous RF test. The benefit of this method, to have a spatial and temporal study of the quench behaviour, comes with the disadvantage of a time consuming preparation and testing procedure. To overcome this and increase the efficiency in detecting the origin of a quench, another method was developed and is described next.

5.3   Second Sound

The aim of the second sound method, is to reduce the time consuming process to detect a quench origin with T-map. This method was developed in 2009 at Cornell [206]. It is based on an effect in superfluid helium, the so called second sound, predicted and described in the early 1940s [207–209]. In the two fluid model of superfluid medias, a local hot spot on a cavity surface will create besides the normal pressure wave (the first sound) a second wave, which will have no net mass flow. The net mass flow for the second sound wave is given as

$$\rho v = \rho_n v_n + \rho_s v_s = 0 \tag{5.6}$$

where ρ_i is the density of the normal- or superfluid component and v_i the corresponding velocity. The energy deposited by the quench in the liquid helium causes a break up of the superfluid components and therefore change the density ratio locally and a counterflow of superfluid and normal fluid components to reestablish the equilibrium is induced. This counterflow can only change the local density ratio but no mass flow will take place and hence, the pressure can not change. Nevertheless the entropy, which depends on the density ratio, has to change locally and this entropy wave travels through the helium and can be measured. The velocity C of this entropy wave can be calculated to

$$C^2 = \left(\frac{\rho_s}{\rho_n}\right) S^2 \left(\frac{\partial T}{\partial S}\right)_p = \left(\frac{\rho_s}{\rho_n}\right) S^2 \left(\frac{T}{c_v}\right) \tag{5.7}$$

where c_v is the specific heat at constant volume, S the entropy of the system and T the temperature of the system. Since the densities of the components are also temperature dependent, a rather flat maximum of the velocity at around 1.8 K with 20 m/s exist.
In figure 5.5 a visualization of the process is given. The first experimental verification of this process was done in 1946 [210]. A measurement system to detect the second sound waves are so called oscillating superleak transducer (OST) [211, 212]. The working principle is analog of a condenser microphone. The local ratio of normal- and superfluid ratio varies as the second sound waves enters the microphone, and therefore the permittivity. Since the membrane is coated with a conducting material and a voltage is applied onto the electrode behind the membrane, the capacity changes as the permittivity within the capacitor is changed.
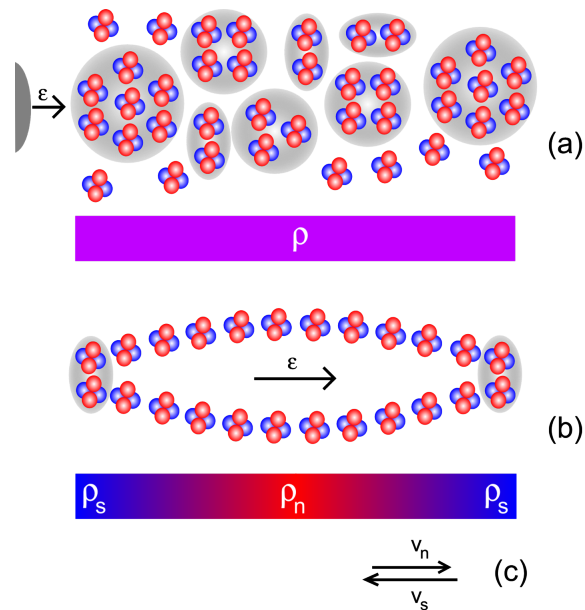
Figure 5.5: Energy propagation in superfluid helium. In (a) the density equilibrium of the two fluid-components is distorted by the deploying of an amount of energy ε into the superfluid. The energy leads to a break up of superfluid components and a local rise of the normal fluid. Therefore a superfluid counterflow takes place, and the two flows cancel out each other concerning a net mass flow but the entropy will spatially oscillate [201].

Since the OSTs are permanently installed at the inserts of the RF test stand, this measurement can run parasitic during normal RF cold test. This reduces the total time for detecting a quench spot during a RF test and further research is carried out at DESY to improve this method [213, 214].

5.4 Optical Surface Inspection

Another possibility to investigate the RF performance is to inspect the inner surface of the cavity, which is exposed to the RF field. For this purpose, a dedicated optical inspection tool have been developed at KEK [215] and further improved at DESY, to meet the industrial standard during the XFEL fabrication [216, 217]. The robot developed for this purpose is the main tool for this thesis. It will be described in detail in the next chapter, chapter 6. The images taken at this robot and how they will be processed will be described in chapter 7. Results of this analysis, how the surface can be characterized, surface properties depending on vendor specific fabrication and the influence of optical surface properties onto the RF performance are the main topic of this thesis.

CHAPTER 6

Optical Surface Inspection

For a better understanding of the RF behavior of cavities, a surface inspection was developed at KEK [215, 218]. The intention is, that an optical inspection of the inner surface, which is exposed to the RF field, leads to a better understanding of limitations observed during RF tests. While a general correlation was found between low field quenches and localized defects seen in optical inspections [119, 219–222], the interplay of global surface properties and RF performance still needs to be investigated. A method to study possible relations between the surface properties and the RF performance was developed within this thesis. It is based on a high resolution optical system with individual controllable LED stripes for illumination. The combination of a linear and a rotational movement facilitates the complete inspection of the inner cavity surface. This so called "Kyoto camera" system is now an established tool in several institutes [219].

A first setup of the Kyoto camera system was implemented at DESY, where optical inspections of pre-series XFEL cavities, large grain cavities and other cavity test series were performed [217]. The sliding table, the camera rotation and the data handling were completely manually operated. A single inspection took up to several days until it was finished. The examination of the images were partially done while they were taken by the operator.

To establish the optical inspection as a quality management tool during the production of 824 SRF cavities for XFEL, an automated optical inspection tool with automatic data management was developed at DESY as a successor of the original Kyoto camera setup. The aim of this project was to reduce the total time of an optical inspection as well as the time which an operator has to actively monitor the process. This was vital since a tool for qualification management needs short times between receiving a cavity and reporting a feedback to the production line. The automated optical inspection has already proven its potential as a tool for quality control for the vendors producing cavities for XFEL.

6.1 OBACHT

The result of the above mentioned development is the "**O**ptical **B**ench for **A**utomated **C**avity inspection with **H**igh resolution on short **T**imescales" (OBACHT). A short description of the mechanics and control software is given, along with a brief overview of the data handling. A more detailed discussion of the camera, the optical system and the illumination system follows, since limitations and requirements of the image processing algorithm, described in the next chapter, can be formulated from these system parts.

6.1.1 Mechanical Setup and Motor Properties

In figure 6.1, a 3D sketch of OBACHT is shown. The 9-cell-cavity is mounted on a movable sled. To have also the option to inspect cavities dressed with a helium tank, the decision was made to rotate the rod in which the camera system is installed, instead of the cavity. Otherwise, the helium-pipe of the tank would increase the complexity of the machine.
The linear motor, which drives the movable sled, has a positioning precision of ± 2 μm. The torque motor for the rotation of the camera rod has a positioning precision of ± 40 μdegree. A more detailed description of all mechanical and sensor components can be found in [216].
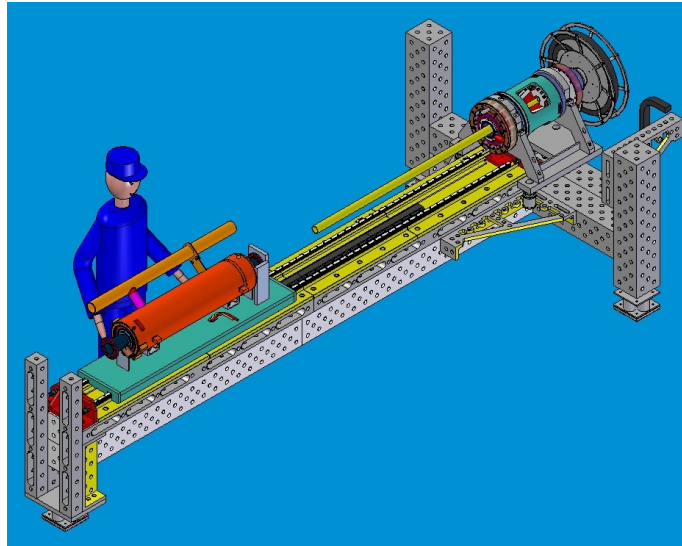
Figure 6.1: 3D sketch of the OBACHT set up. A cavity with helium tank (orange) is mounted on the movable sled (turquoise), which is located at the mounting position. The camera rod (yellow) can be rotated with the torque motor (turqoise/gray).

6.1.2 Motor Control

The motors are steered and controlled by a Programmable Logic Controller (PLC). The parameters for the motor movements are directly set within the PLC. The communication between the user PC and the PLC is done via the Windows-Interface "OLE for Process Control" (OPC). The OPC provides logical blocks for a programming of the motors. An access to program and control the PLC was necessary in the beginning to develop the measurement procedure as well as to investigate optimal motor settings and to include a machine protection system [223]. To ensure safety, light curtains are installed around OBACHT during operation.

6.1.3 Front End GUI

To reduce the complexity of the inspection process and the training needed to operate the machine, a Graphical User Interface (GUI) was developed. This was done using the graphical programming software LabVIEW and the logical blocks provided by the OPC. A set of default values for the illumination, the camera system and the PLC are provided by this environment. The operator has to calibrate the cavity-OBACHT system in terms of longitudinal deviations from the cell-to-cell distance and control the angular reference point with respect to the cavity power coupler. In addition, a focal calibration is performed. Cavity information is entered into a template, from which the relevant data and folder structures for later data management are generated [224].

A calibration is necessary because of two reasons. With the given precision of the longitudinal motor and camera system, OBACHT is sensitive to the longitudinal deformation of the cavity introduced during RF tuning. The deviations of these cell-to-cell distance are on the order of millimeters. To make sure that the images taken show the complete welding seam, these deviations need to be adjusted for each equator. This is done by moving the camera within the rod until the welding seam is in the image center. The second calibration concerns the optical system and maintaining a focused image throughout the complete inspection. The procedure is described in section 6.2.2.

6.1.4 Inspection Parameters

The camera covers an angle of five degrees in ϕ of the cavity surface at the equator and about 14 degrees at the irides. To have a small overlap at the image edges, the equator and cell images are taken with an angular spacing of 4.8 degree while the iris images are taken with an angular spacing of twelve degree. Additionally, there is an overlap along the cavity z-axis, see figure 6.2.

Each position has an optimized illumination pattern, accounting for the individual surface geometry and reflectivity, and focus settings. With given angular and longitudinal spacing, a total of 2325 images per automated inspection are taken. If needed, individual images of the cavity surface with manual controllable settings can also be taken.
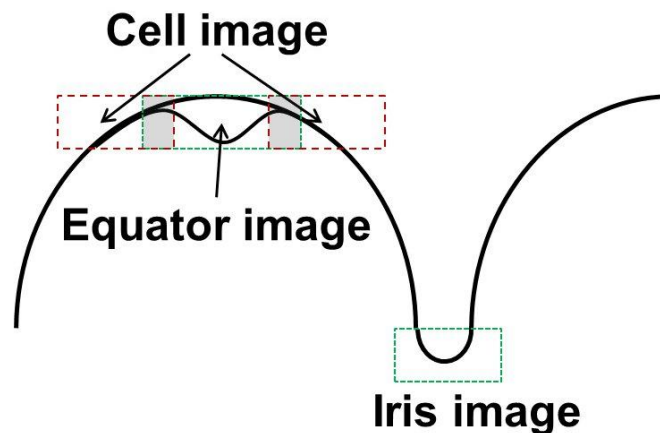
Figure 6.2: Image positions in a cavity. At the equators, the welding seam itself is in the central axis of the image - depicted by the green box. The cell images are taken with an offset of $\pm$ 8 mm relative to the equator position - depicted by the red boxes. The overlap region is shaded. The iris image is taken between the cells and at the beam pipe weldings. Sketch is not to scale.

The image format used at present is JPEG, which is a widely used image compression format. The equator and cell images have a size of the order of 5MB.

6.1.5 Data Handling

Although the details of the data handling procedure have evolved with increased experience over the years, the principles remain the same. The images taken by the system are labeled with cavity name, inspection number, longitudinal and axial position of the camera, illumination pattern and whether the image is an iris, equator or cell image. They are copied from the local data acquisition PC to a distributed file system. To check this process, the MD5 sum is used which may indicate a loss of data during the copy procedure.

For image analysis, the original images are then processed. To reduce the storage space, this step is done parallel to the running inspection or shortly after. The processing of all equator images, generating a data sheet including figures of merit of the optical surface properties of the cavity and a list of images, showing possible problematic cavity surfaces, takes about three hours. Afterwards, the original images are archived.

6.2 Camera and Optical System

The camera system developed at KEK and Kyoto in 2008 [215, 218] was implemented at DESY [217] and had a major upgrade in 2009 [217, 225]. An overview of the camera system is given in figure 6.3.

It consists of a camera rod with a diameter of 50 mm to fit into the cavity without colliding

with the irides or HOM antennas protruding into the cavity volume. In this rod, the camera together with a c-mounted low-distortion lens (LM75JC by Kowa Industrial) are installed. The camera system images the surface via a 45°-tilted half mirror which can be continuously adjusted to other angles in order to inspect other cavity regions. The distance of the camera system to the mirror and therefore the focus is controlled by a motor driven lead screw. For illumination, acrylic strips (two LEDs per strip) are attached to the camera rod around the camera opening are installed, together with three additional LEDs behind the half mirror inside the camera rod.
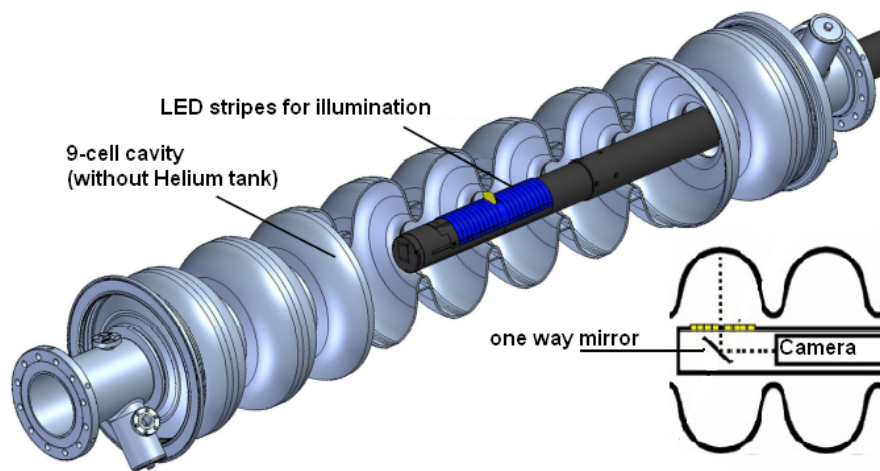
Figure 6.3: Drawing of the Kyoto Camera System used at DESY. The camera is viewing the inner surface via a 45° tilted half mirror. The distance to the mirror can be controlled for focusing. Behind this half mirror, three LEDs are mounted for the central illumination. 2×10 acrylic strips with LEDs are mounted left and right from the opening in the rod for a more detailed illumination [216].

6.2.1 Camera Hardware and Shot Noise

Within the rod, a digital camera (Artray MI900) is installed and connected via USB to the PC. The camera sensor is a CMOS Bayer pattern [226] with 3488×2616 pixels on a sensor area of 6.17×4.55 mm^2. It has a theoretical signal to noise ratio (SNR) of 35dB. An investigation with a noise estimator [227] at OBACHT showed that the effective SNR is 32dB. The primary source of noise in this imaging system is shot noise, which is an intrinsic property of the CMOS sensor. Shot noise is a direct consequence of the digitization process of the signal and the quantized nature of light. It is a stochastic process and creates random fluctuations of the signal strength from each pixel. The way in which shot noise is addressed during processing will be described later.

6.2.2 Resolution and Depth of Field

Important properties of an optical system are the resolution and the depth of field (DOF). The optical system is a diffraction limited lense system which further is projected onto a digital camera sensor. A rough estimation of the resolution d of the camera system can be done via the Abbe diffraction limit

$$d = \frac{\lambda}{NA} \tag{6.1}$$

with NA as the numerical aperture and λ the wavelength of the used light. The numerical aperture NA of the system is 0.4, the wavelength of optical light varies between 400 - 800 nm. This yields to a resolution of the lense system of $d = 1$ - 2 µm. The digital camera further decreases the resolution of the whole optical system. A more precises calculation of the theoretical limit of the resolution can be deduced with the Point Spread Function (PSF) of the system. The PSF describes the behaviour of the light, emitted from a point-like light source, as it is transfered through the optical system and finally detected at the imaging plane. The calculation of the theoretical PSF was done with a Java implementation of a PSF Generator [228, 229] and MATLAB to control and analyze the process. The Born-Wolf Model [230, 231] was chosen as suitable for the setup since this model describes the diffraction of a spherical wave by a circular aperture when the point light source is in focus and no immersion oils are used. The minimum distance which is needed to resolve two distinct objects is given via the Full-Width-Half-Maximum (FWHM) of the PSF, if the detector is in the imaging plane.

With the values of the system a theoretical resolution of OBACHT of $d = 11.7 \pm 0.9$ µm can be achieved, if the object is in focus.

The effective resolution of OBACHT was investigated using a dedicated test pattern, namely the USAF 1951 Resolution Test Chart [232]. It is a set of well defined separate lines with decreasing distance and thickness. The smallest distance between objects, which were still resolved as an array of separate lines, is the effective resolution of the system. For OBACHT, these were the elements of group number five, element number three. This results in an effective resolution of $d = 12.4$ µm at OBACHT. This is in agreement with the theoretical limit, since the next finer group of elements is below the theoretical resolution.

The magnification M can be calculated from the given projected cavity surface seen in the image (12×9 mm^2) and sensor dimensions (6.1×4.58 mm^2). Basically, it is the projection ratio between the sensor dimension and the image dimension. Since the image is larger than the sensor, the magnification has to be smaller than unity.

$$M = \frac{6.1\text{mm}}{12\text{mm}} = \frac{4.58\text{mm}}{9\text{mm}} = 0.51$$

With given magnification M and object resolution, the camera resolution can be calculated to be 6.31 µm. With the given pixel sensor size of 1.75 µm, the smallest resolvable objects have a size of four pixels. This is in agreement with the theoretical resolution, where the maximum of the PSF distribution covers four pixels.

The DOF is defined as the distance between the nearest and farthest objects in an image, which are still in focus. Figure 6.4 illustrates the DOF. In general, the DOF is controlled
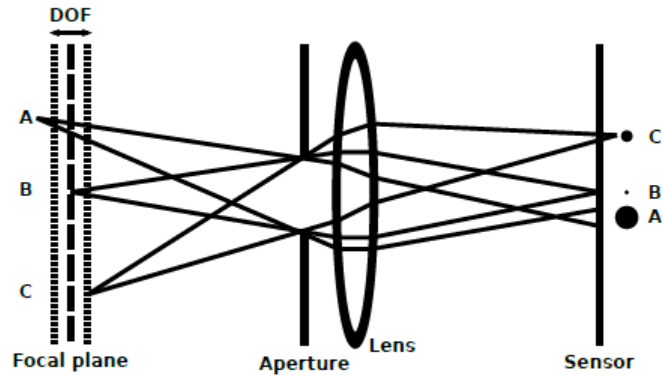
Figure 6.4: The points on the left side of the image (A,B,C) are projected onto the camera sensor by the lense and aperture. Depending on the position of the observed points, whether within our outside the finite DOF, they appear as bigger points on the camera sensor [217].

with the F-number of the lens, because the DOF is inverse proportional to the relative aperture. The aperture is set manually at the lense, and a disassembly of the camera rod is necessary to change it. The original DOF was less than 0.1 mm [217], but experience showed that a DOF of 2.8 mm is necessary for an automated optical inspection in order to achieve sharp images. The equatorial welding seam region has a W-like cross section. The welding seam itself rises up to 0.3 mm above the surrounding cavity surface. Although a small DOF gives the possibility to make a profile scan along the lateral axis and create a height map of the welding seam via focal stacking [233], it would also increase the amount of unfocused regions in a single image and decrease the spatial resolution in these regions, see figure 6.5.
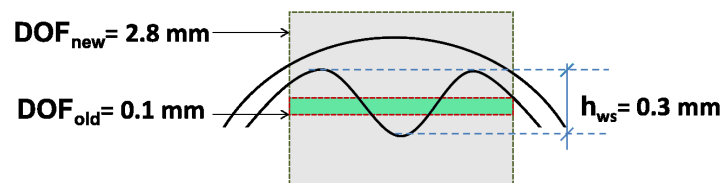
Figure 6.5: A schematic cross section of the welding seam surface. The old DOF was less than one third of the welding seam height and enabled the system to perform height map scans but led to blurry regions. The new DOF covers the whole range of the surface profile and each part of the image is in focus.

To control the center plane of the DOF, the camera focus, the camera is moved with a lead screw in the camera rod, see figure 6.6. It is driven by a torque motor and has a precision of 4 μm. The optical system has a focal length of $f = 150$ mm and the surface-mirror
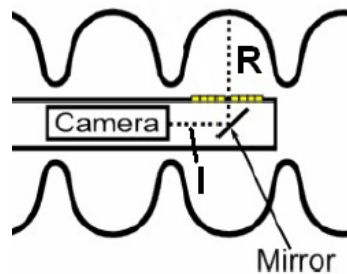
Figure 6.6: The focal length of the optical system f is the sum of the cell radius R and the camera-mirror distance l. The latter has to be adjusted to correct for deviations of the surface-mirror distance to keep the inner cavity surface in focus.

distance equals the cell radius R and is in the order of 103 ± 0.3 mm. The offset of 0.3 mm is found to be the average deviation for XFEL production and is measured w.r.t. to the cavity geometrical axis defined by the centers of two reference rings [46, 47].

Before an inspection can be started, the optimal camera position for each cell has to be determined. This calibration is performed since the distance between the surface and the camera is not constant, see figure 6.7. The optical position for a specific cell can
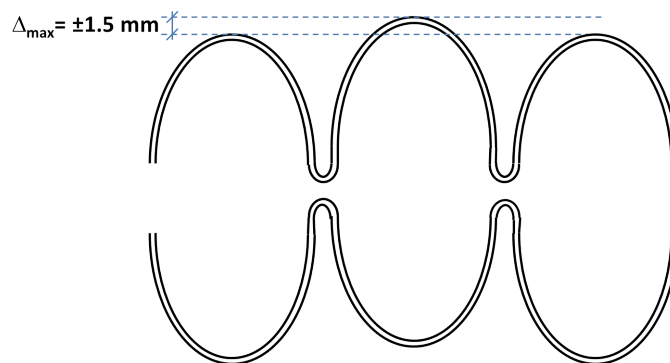
Figure 6.7: A cell symmetry axis can deviate from the geometrical axis up to 1.5 mm. The deviations are randomly angular distributed and each cell can be affected, leading to a individual camera position for each cell.

be deduced by finding the best camera position at four different angles around the cell, each 90 degrees apart, and calculate the average position in which each image at the four angles is in focus. This procedure is repeated for the first, the fifth and the ninth cell. With these three positions along the cavity, a linear fit, the optical axis, is derived. The camera can now be set to the best position for each cell deduced from this optical axis. Additionally with a DOF of 2.8 mm, the need for a manual adjustment of the camera position to compensate offsets to the optical axis is reduced.

6.3   Illumination System

The purpose of the illumination system is to guarantee an intensity distribution over the image which enhances surface structures like grain boundaries but minimizes shadows. At OBACHT, three LEDs are installed behind the half mirror, together with 2×10 acrylic strips, with two LEDs per strip, left and right of the rod opening for the camera. The acrylic strips have a width of 7 mm and can be individually turned on and off. The three LEDs behind the half mirror are used to compensate the missing LED strip at the camera opening.
The capability to adapt the image illumination system to the surface geometry to achieve the optimized intensity distribution over the image is limited. Due to the cross section of the welding seam, it is unavoidable to have shadows and illumination pattern introduced by the LED strips in the image. The default setting of the illumination pattern at OBACHT, shown in figure 6.8, is based on experience. While adapting the illumination for each image might improve the quality of the image even further, those above mentioned patterns have proven to give satisfying illumination in almost all cases. In
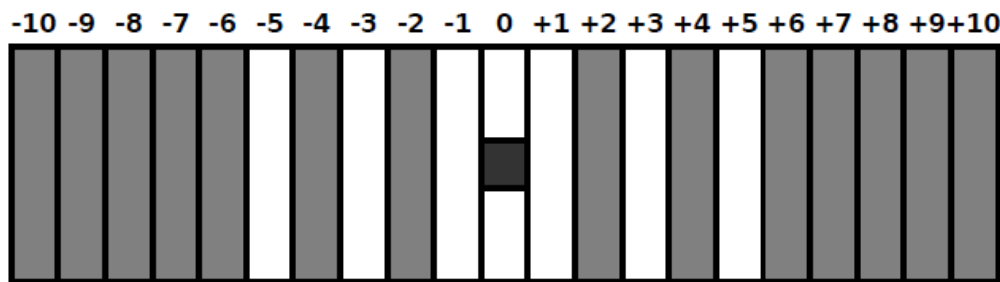
Figure 6.8: Default illumination pattern for images at the equator [217]. Stripes are numbered from left to right, starting with -10 and ending with +10. Grey stripes are switched off, white stripes are switched on. The dark square in the center indicates the opening for the camera.

the following, a simple calculation is presented to estimate the slope of grain boundaries at which the boundary can be directly seen with a given illumination system assuming specular reflection. The detection of a given surface feature at an angle θ to the nominal surface plane is determine by the geometry shown in figure 6.9. This incident angle depends on the slope of the boundary and the distance to the LED stripe and the camera. With the given geometry, a maximum boundary slope of 20 degrees can be resolved. This value was also derived in [234]. Any boundary with a slope above 20 degrees will be darker than its surroundings and will be still detected as boundary, but the accurate determination of the boundary slope is impossible.

61
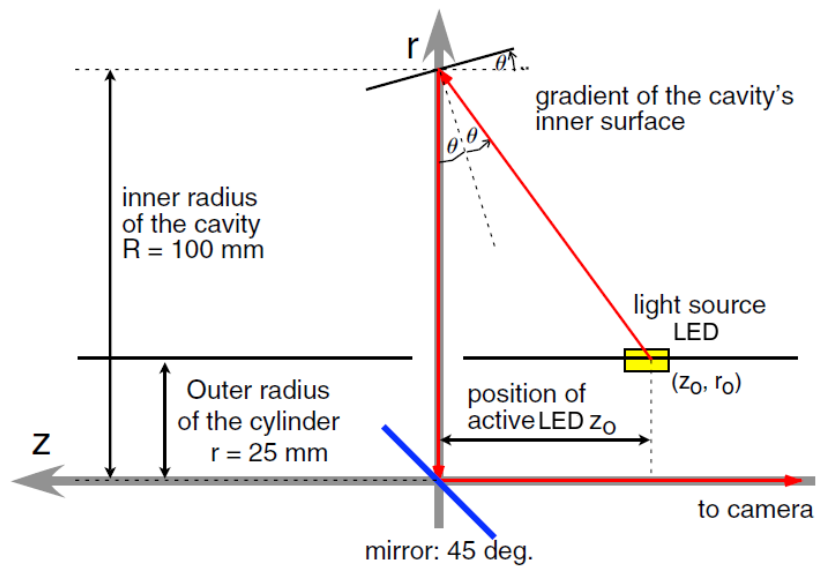
Figure 6.9: Schematic view of the illumination model [215]. With given properties of the cavity and acquisition geometry, the incident angle θ of the grain boundary can be calculated.

CHAPTER 7

Image Processing Algorithm

This chapter describes the image processing algorithm, given the restrictions and requirements discussed in the chapter of the optical system of OBACHT. The description will include parameters, which where chosen from a heuristic point of view, and properties of the algorithm.

Image analysis as a quality management tool will be introduced in chapter 8 and 9. Image understanding is used to correlate RF test performance with optical properties, and is discussed in chapter 10.

7.1   Image Processing

OBACHT provides visible information on the cavity surface structure which includes grain boundaries, defects and the welding seam. These have to be characterized in terms of geometrical properties and location within the image by means of the analysis algorithm. To improve the detectability of the grain boundaries, the image has to be processed. A combination of global and local operators acting on the image was developed in the scope of this thesis, where the goal is to enhance features in the image. A flowchart of the processing steps is shown in 7.1.

7.1.1   Digital Image and Objects of Interest

The presentation of the digital image taken by OBACHT, as used as an input to the algorithm, is a $3488 \times 2616 \times 3$ matrix. The first two dimensions represent the spatial dimension of the image. The third dimension represents the color information in the image. The three color layers are red (R), green (G) and blue (B). The objects of interest are the grain boundaries of the niobium crystal. An optical boundary in an image is defined as a contour with finite width of up to several pixels that represents a continuous change of intensity. In contrast, an edge is the border of a boundary. In [235] it is stated, that "edge detection can be a low-level technique towards the goal of boundary detection". Those two definitions, that of an edge and that of a boundary, should not be confused.

The physical grain boundary is used synonymously with the image boundary in this thesis. The motivation for this is that any intensity gradient, which is in an image boundary, can only be caused by a geometric gradient or by a change in reflectivity. The first is a grain boundary, the latter can be caused by impurities or different surface structures.

7.1.2 Processing Algorithm
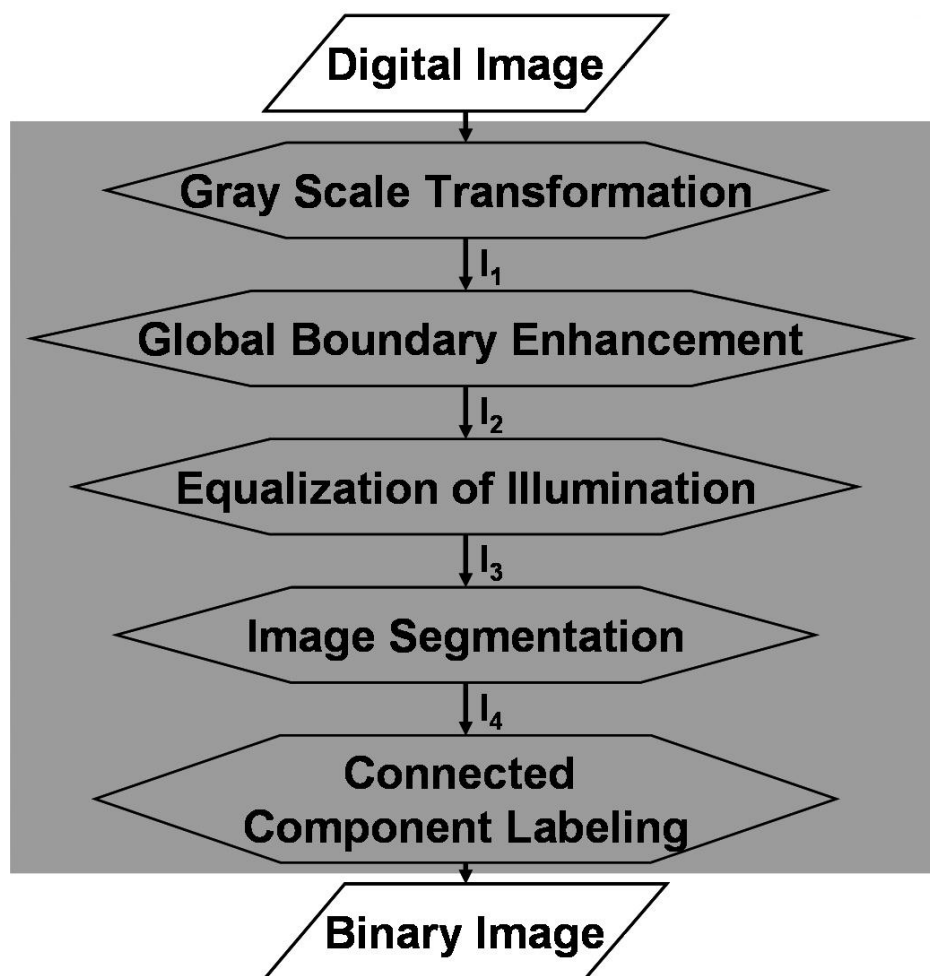
Figure 7.1: Flowchart of the developed algorithm for image processing. The output of the algorithm is a binary image. The image processing algorithm is depicted by the gray rectangle. The indices 'I_i' refer to intermediate pictures. Both, the binary image and the original digital image is used for further image analysis.

7.1.2.1 Gray scale transformation

Since the physical objects of interest are the grain boundaries, the objects of interest for the image processing algorithm are the image boundaries. To simplify the operators used in the algorithm, the color image is transformed into a gray scale image. Mathematically, the image matrix is reduced from three color to one intensity dimension. To achieve this, a weighted sum of the color components for each pixel is calculated via

$$I_1 = 0.2989 \cdot R + 0.5870 \cdot G + 0.1140 \cdot B \tag{7.1}$$

with R, G and B stand for the respective color layer and I_1 the intensity for the pixel. The weights are taken from the CIE1931 standard color space transformations [236, 237]. This transformation causes no loss of relevant information although the color is neglected. The intensity information is conserved during this transformation which carries all information about relevant gradients and connectivity of pixel. The color on the other hand can be a powerful descriptor that often simplifies object identification and is preserved in the original image and available for further image analysis steps.

7.1.2.2 Global boundary enhancement

As a second step, all pixels with intensity gradients will be enhanced, regardless of the origin of their gradients. This is done by generating an intermediate image which is obtained after applying a Gaussian low-pass filter to the gray scale image I_1. This intermediate image is inverted and added to the gray scale image. Since the intermediate image will only contain low spatial frequency parts and the intensity values are inverted, those pixel intensities will be reduced. The resulting image I_2 will contain pixels with high gradients and high intensities and pixels with low gradients and low intensities. This step simplifies the further detection of boundaries.

Using a Gaussian filter before edge detection reduces the noise level in the image by smoothing the fluctuations, which improves the result of the following edge-detection algorithm. The kernel of the low pass filter h is a $n_x \times n_y = 5 \times 5$ pixels matrix with a standard deviation σ of five, where the entries are calculated via

$$h_g(n_x, n_y) = e^{\frac{-\left(n_x^2 + n_y^2\right)}{2\sigma^2}} \tag{7.2}$$

$$h(n_x, n_y) = \frac{h_g(n_x, n_y)}{\sum_{n_x} \sum_{n_y} h_g}. \tag{7.3}$$

Notice that the kernel is center originated, which means the center point of the kernel is $h(0,0)$. Since the kernel size is five, the array index of five elements will be the integers in the interval [-2, 2]. The origin is located at the middle of kernel. The value for σ and the kernel was chosen to be suitable with the given OBACHT resolution. If σ and the kernel size would be larger, the overlapping of neighboring objects would increase and the topology could be changed. A smaller value of the kernel would not be enough to cover noise objects, since OBACHT has a resolution in the order of 4 pixel. A smaller value

of σ would create a steeper Gaussian filter and the effectiveness of the noise reduction would decrease. Hence, the smallest odd integer which fulfill these criteria is five.

The resulting Gaussian filter is convoluted with the intermediate image. Each pixels new value is set to a weighted average of that pixels neighborhood. The original pixel value receives the heaviest weight (having the highest Gaussian value) and neighboring pixels receive smaller weights as their distance to the original pixel increases. Since the neighborhood of each pixel is used in this filter, the boundaries and edges are preserved better than other, more uniform blurring filters. The convolution is calculated with the formula

$$\mathrm{I}_{\text{intermediate}}(\mathrm{x},\mathrm{y}) = \mathrm{I}_1(\mathrm{x},\mathrm{y}) * h(x,y) = \sum_{k_1=-2}^{2} \sum_{k_2=-2}^{2} h(k_1,k_2) I_1(x-k_1,y-k_2). \qquad (7.4)$$

If the kernel is applied to pixels close to the image edges and leaps over the image, the algorithm will pad zeros where the input values are not defined.

7.1.2.3   Local Contrast Enhancement

The image processing algorithm has to even out the illumination pattern (see section 6.3) in order to detect boundaries regardless their position in the image. To achieve this, a local approach has to be chosen. Not the complete image but rather a local pixel neighborhood should be processed to even out the differences and hence to improve the detection probability. The so called contrast limited adaptive histogram equalization (CLAHE) algorithm is used, which prevents an overamplification of noise [238, 239].

In figure 7.2, the image histogram H describes the gray value distribution in an image region and, if normalized by the pixel count in this very image region, can be interpreted as the local probability distribution (PDF) of gray values. Hence, the PDF is defined as

$$\mathrm{PDF}(x) = \frac{\mathrm{H}(\mathrm{x})}{N_x \times N_y} \qquad (7.5)$$

with x as gray value, $H(x)$ as the number of pixels with the specific gray value, and $N_x \times N_y$ the number of pixels in the image region. Furthermore, the cumulative distribution function (CDF) can be defined as

$$\mathrm{CDF}(x) = \int_0^x \mathrm{PDF}(x)dx. \qquad (7.6)$$

 To equalize the histogram, a transfer function which linearizes the CDF over a given range is defined. This procedure is called adaptive histogram equalization (AHE). This means, a mapping function T which produces a new image I_3 after applying onto the original image I_2

$$\mathrm{I}_3 = \mathrm{T} \cdot \mathrm{I}_2 \qquad (7.7)$$

is defined in such a way, that the CDF of the image I_3 can be written as

$$\mathrm{CDF}_3(x_3) = x_3 \cdot K \qquad (7.8)$$
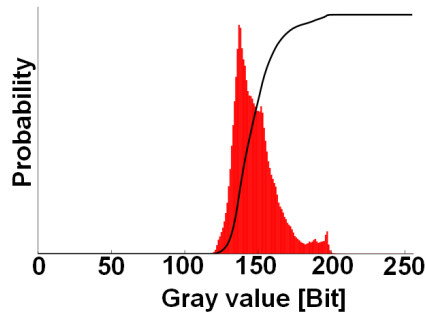
Figure 7.2: Gray scale histogram with low contrast. The red histogram represents the local probability density function (PDF), the black line the cumulative distribution function (CDF).

with some constant K and x_3 as pixel value in image I_3. Making the assumption, that CDF_3 is on the same range than CDF_2 and the number of pixels are not changed, it can be written

$$PDF_3(x_3)dx_3 = PDF_2(x_2)dx_2 \qquad (7.9)$$

and with the output histogram is equalized to one, $PDF_3(x) = 1$, it can be written

$$dx_3 = PDF_2(x)dx_2 \qquad (7.10)$$

Integrating both sides, the mapping function T is obtained.

$$x_3 = T(x_2) = \int_0^x PDF_2(x)dx_2 = CDF_2(x) - CDF_2(0) = CDF_2(x). \qquad (7.11)$$

T is the CDF of the image I_2. Applying this mapping function to the original PDF will lead to a linearized CDF_3, cf. figure 7.3.
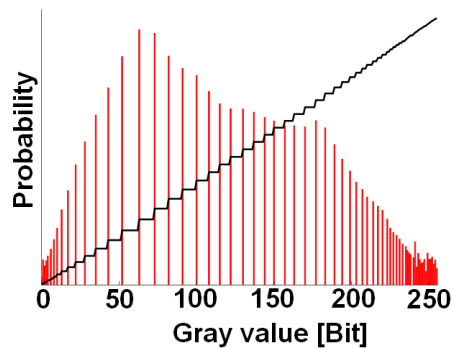
Figure 7.3: Contrast enhanced histogram (original figure 7.2). The CDF is linearized via adaptive binning of the PDF.

67

This AHE method applied onto a narrow PDF would have the tendency to over amplify noise. The mapping function will map the narrow range of pixel values to the whole range of the target histogram [238]. To prevent the over amplification of noise, a limiting form of the mapping function is used, where a cutoff in the counts on the PDF, the so called clipping limit, is introduced. If a part of the PDF exceeds a certain value, this part is equally distributed across all the histogram bins. This again pushes some bins above the clipping limit, which leads to a modification of the original clipping limit and an effective limit is used. This clipping of the PDF leads to a smaller slope of the CDF and therefore to a weaker local amplification of the contrast. This method is highly desired since a large illumination spread within the image and narrow peaks within the PDF are observed.
The CLAHE algorithm is applied onto a local 9×9 pixels neighborhood.
For further reduction of noise in the resulting image, a median filter [240] for smoothing is applied, where the idea of a median filter is to replace each pixel value with the median of its local neighborhood of 3×3 pixels. It preserves edges and outperforms linear filters at low noise levels [241]. Summing up, the CLAHE algorithm is of vital interest, since it achieves a contrast independent object detection. The downside of this local enhancement is the amplification of noise throughout the image. This issue is addressed by the clipping limit within the method and median filtering afterwards, but will not be solved completely with these steps.

7.1.2.4 Image Segmentation

Image segmentation is a partitioning process that divides an image into regions. The method used here is a histogram based segmentation, called Otsu's method [242]. The underlying assumption for this method is that the image consists of two pixel classes, class 0 are background pixels and class 1 are foreground pixels with a bimodal distribution in the gray scale PDF as in figure 7.4.
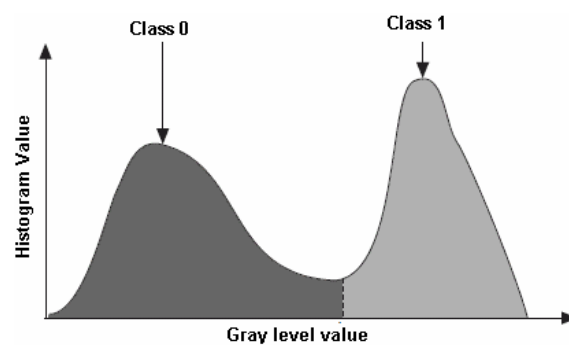
Figure 7.4: Gray scale histogram. Two classes of pixels can be identified in the histogram [243]. Class 0 are background pixels and class 1 are foreground pixels. The optimal threshold to separate these classes can be found by calculating the intra-class variances as a function of the threshold. The optimal threshold is the one which minimizes these variances.

68

In this case the foreground objects are the boundaries and the background homogeneous regions in the image. Otsu's method searches for an optimal threshold t which separates the classes and minimizes the intra-class variance and maximizes the inter-class variance. $\overline{g}$ is the arithmetic mean of the gray values in the complete image, $\overline{g}_0$ and $\overline{g}_1$ the arithmetic mean values of the individual classes, then the variances within the classes are

$$\sigma_0^2(t) = \sum_{g=0}^{t} (g - \overline{g}_0)^2 \cdot PDF_0(g) \tag{7.12}$$

and

$$\sigma_1^2(t) = \sum_{g=t+1}^{G} (g - \overline{g}_1)^2 \cdot PDF_1(g). \tag{7.13}$$

Furthermore, the intra-class variance is

$$\sigma_{intra}^2(t) = PDF_0(t) \cdot \sigma_0^2(t) + PDF_1(t) \cdot \sigma_1^2(t) \tag{7.14}$$

and the inter-class variance

$$\sigma_{inter}^2(t) = PDF_0(t) \cdot (\overline{g}_0 - \overline{g})^2 + PDF_1(t) \cdot (\overline{g}_1 - \overline{g})^2. \tag{7.15}$$

With the quotient Q, defined as

$$Q(t) = \frac{\sigma_{inter}^2(t)}{\sigma_{intra}^2(t)}, \tag{7.16}$$

the optimal threshold can be found via

$$\left. \frac{dQ(t)}{dt} \right|_{t,opt} = 0, \tag{7.17}$$

since the optimal threshold t maximizes the quotient Q. All pixels with gray values above this threshold are considered to be foreground. The output of this algorithm is a binary image of the same size as the input image. Every foreground pixel will have the value 1 and the background pixels have the value 0.

7.1.2.5 Connected Component Labeling

The final processing step is the so called connected component labeling. The aim of this step is to decide which pixels are connected and form a single object, like a grain boundary. The method used here is the run-length encoding described in [244]. A row (or column) in a binary image can be represented as a sequence of ones and zeros, where a connected sequence of ones is called a run. Each single run can be represented by a starting pixel and by the number of pixels in this run, which is called run-length. Based on the multiple runs in a binary image, an adjacency matrix is created, in which the spatial

connections in rows and columns between several runs is encoded. A graph theoretical approach to this adjacency matrix [245,246] is used to compute the connected components of the corresponding graph and labels each run in the output label matrix according to the adjacency matrix. Runs with same labels are considered as connected components and the output label matrix is a binary image. This binary image is the key for the image analysis algorithm since it contains the information which pixel is part of a grain boundary.

7.1.2.6 Pixel Noise Reduction

The final binary image will contain unphysical objects due to shot noise fluctuations which were enhanced during the image processing. The following possible consequences of pixel noise must be considered:

1. *Unphysical object generation*: If single or clusters of pixels exceed a certain intensity difference w.r.t. its local neighborhood solely because of shot noise, they are enhanced throughout the processing and would be identified as surface features.

2. *Topological errors*: In regions with high object densities and small object distances, it is possible that two distinct objects are connected to one single object because of shot noise.

3. *Classification errors*: Intensities along boundaries of objects vary because of the shot noise. This would lead to a misclassification of individual pixels, if they falsely undershoot a threshold.

Although many steps were performed to minimize the influence of shot noise in the image, the CLAHE algorithm will enhance the noise and the final binary image will contain several of these pixel noise objects. A statistical approach to analyze the area distribution of these pixel noise objects was performed in this thesis.
Starting with a black 2616×3488 image, a fraction of white pixels was randomly inserted. This fraction was observed to be $25 \pm 2\%$ as the average amount of white pixels in a typical processed OBACHT image after image processing and is used as an input for this method. Although this fraction overestimates the total amount of noise, it gives a reasonable starting point for the following procedure.
After generating 1000 images with the random distributed white pixels and applying the image processing algorithm, the accumulated area distribution of the detected objects is derived, see figure 7.5.
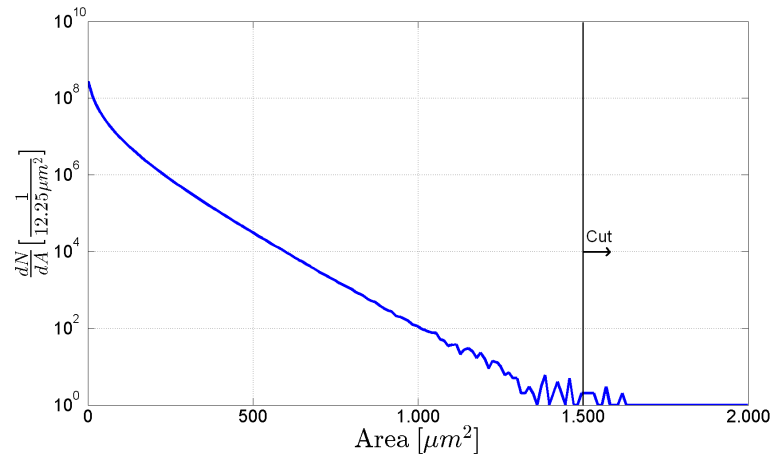
Figure 7.5: Pixel noise distribution. On the x-axis the area of the objects found in the binary images is shown. On the y-axis the counts per bin are displayed on logarithmic scale. This histogram contains the sum of 1000 images. Objects below an area of 1500 μm^2 are cut.

Given the area distribution, a threshold value of 1500 μm^2 or 122 pixels was identified by choosing the largest artificial created object by shot noise. Any objects generated by shot noise are smaller than this value. A comparison of an image section before and after the area cut on this threshold value is shown in figure 7.6. Some small remains of noisy
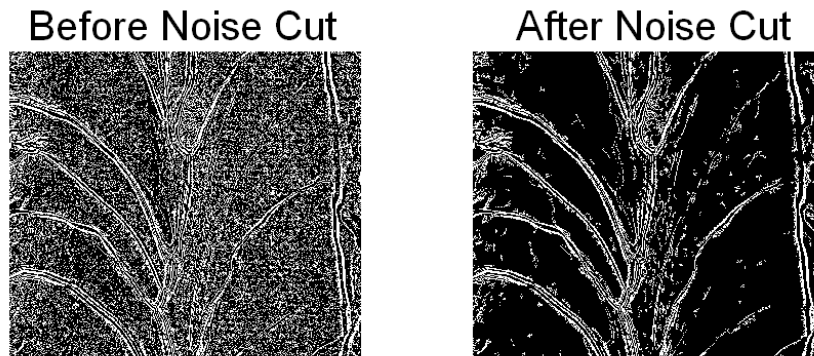
Figure 7.6: The left image shows an image section of the binary representation before the area cut to remove the noise, the right image the same image section after objects with an area smaller than 1500 μm^2 are removed. More than 99.8 % of objects in the image was removed.

objects can be seen in figure 7.6 on the right, but more than 99.8 % of the objects in an image are removed on average. This reduces the number of objects, which need to be analyzed to the order of several hundreds.

For comparison, a heuristic method to find a threshold value was performed. The approach was to find a value for the threshold which removes as many noise objects as possible before removing the first objects representing grain boundaries.

The threshold value found by this heuristic approach fluctuates strongly for individual images, but on average it was found to be four times larger than the statistical approach, which yields 6000 μm^2 or 490 pixels. A comparison of the absolute numbers of objects which remained after the cut showed a non-significant improvement of the higher threshold value. Of the remaining objects, only 0.5 % were found to be still noise objects, which could be removed by the higher threshold value. Summing up, the remaining noise objects do not significantly contribute to the optical properties found by the image processing algorithm. In addition, defects with an equivalent diameter below 43 μm would be filtered out with the larger empirically derived value. Therefore the 1500 μm^2 threshold was chosen for the algorithm.

7.1.3 Summary of the Processing Algorithm

The output of the image processing algorithm is a binary image (see figure 7.1 for process flow). In figure 7.7, an example of an input image as taken by OBACHT is shown. The output of the algorithm, for this example image, is shown in figure 7.8. Both images are transfered to the image analysis code.
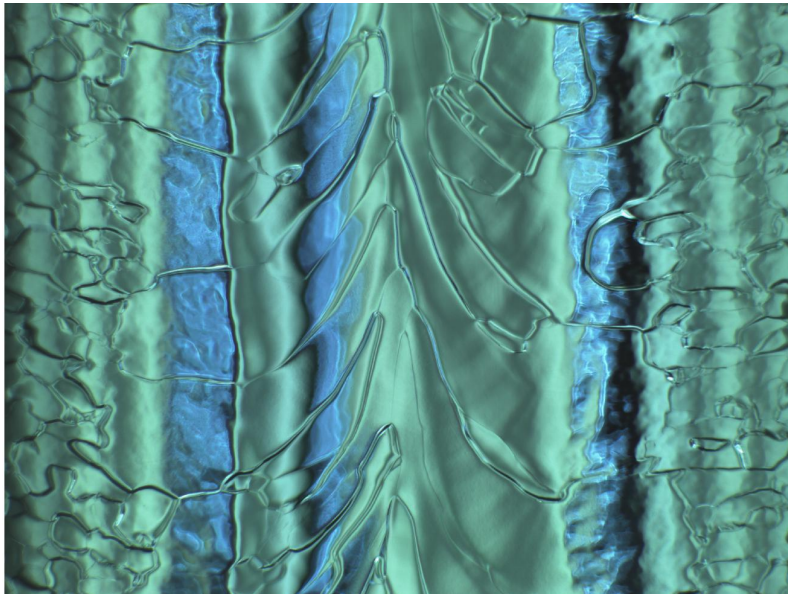
Figure 7.7: Digital image of a treated cavity as taken with OBACHT.

Figure 7.8: The binary image of the image shown in the previous figure, derived with the image processing algorithm.

The pixels in the binary image are obtained by applying the image processing algorithm on the digital image taken with OBACHT. A set of local and global operators are applied which are optimized to achieve both: Enhancing of intensity variations but minimizes noise fluctuations. After these operations, an image segmentation method and a method to detect connected regions is applied. The output is a binary image, which includes detailed information of the state of each pixel in the image. The bit value of each pixel carries the information whether it is a foreground or a background pixel. In addition, each foreground pixel carries a linking information which associates each pixel to a run from the connected component labeling and hence form grain boundaries and other surface structures.

7.2   Algorithm Benchmark

To discuss and interpret results obtained by use of the presented algorithm, its performance is explored. Several benchmark scenarios were used to gain more information about the performance.

7.2.1   Resolution

To investigate the resolution limit of the image processing algorithm, a set of well known test images was used to identify the smallest distance still resolved.
The benchmark pattern was the the USAF 1951 test chart, the same image as used for the optical resolution in section 6.2.2 on page 58. The image is processed with the algorithm and the boundary pixels of the detected group elements are shown in figure 7.9. The smallest objects, which are still detected as individual stripes, are part of group five,
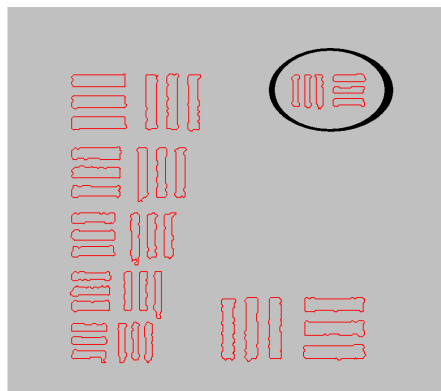
Figure 7.9: USAF 1951 test chart after image processing. The red lines show the edges of the detected elements. The smallest separated group elements - encircled - are the elements of group five, elements one. This results in an resolution of 15.63 μm.

element one. This results in a algorithm resolution of 15.63 μm with good contrast. The algorithm resolution is slightly below the resolution of the optical system (12.4 μm). This is because of the filtering and smoothing procedure, which tends to connect large objects with a distance smaller than four pixels.
Additionally, a contrast dependent resolution check was performed. A series of white lines with a thickness of ten pixels and a distance of 5-15 pixels was placed on 16 different backgrounds. The background intensity was increased in 16 Bit steps from [0, 240] to test the contrast dependence of the resolution. Lines, spaced by a distance of 10 pixels or more, which equals 35 μm or more on the cavity surface or twice the algorithm resolution, have been resolved independently of the contrast. This contrast independent resolution is based on the CLAHE algorithm, introduced in section 7.1.2.3.

7.2.2 Accuracy

The image processing algorithm can be interpreted as a classifier, since the binary image classifies each pixel either as a background (no boundary) or a foreground (boundary) pixel. The accuracy is defined as

$$\text{Accuracy} = \frac{\sum \text{true positive} + \sum \text{true negative}}{\sum \text{All pixels}} \tag{7.18}$$

with true negatives or true positives as pixels which are correctly identified as background or foreground pixels. Also interesting is the positive predictive value (PPV). The definition is

$$\text{PPV} = \frac{\sum \text{true positive}}{\sum \text{true positive} + \sum \text{false positive}} \tag{7.19}$$

and gives a measure of the probability that a pixel identified as boundary pixel is truly a boundary pixel. This value can be used to correct the derived object area from the algorithm.

In order to have the ability to decide whether a pixel is rightly or wrongly classified, a test image with known properties is used. Here, the Jaehne test image g_1 [247], shown in figure 7.10, is used. It can be calculated via

$$g_0 = \frac{\sin(\pi r^2)}{r_{max}}; g_1 = \frac{(g_0 + 1)}{2}. \tag{7.20}$$

With g_i the gray scale test image, r as the radius of the circle and r_{max} the maximum radius, 283 pixels in this case. The latter equation is used to scale and shift the image to the interval [0,1] Bit, which allows a direct comparison of g_1 to the binary image.
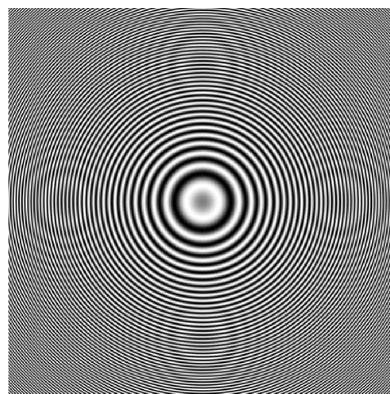
Figure 7.10: The Jaehne test image: A set of concentric rings. Any other pattern seen is due to the aliasing artifact in the low resolution printing.

The ring cross sections can be approximated with Gaussian profiles. With this knowledge, the $\pm 1\sigma$ region of the Gaussian profile is defined as ring width, resulting in the classification that any pixel with a value between [0.46, 1] Bit is part of the ring, see figure 7.11.
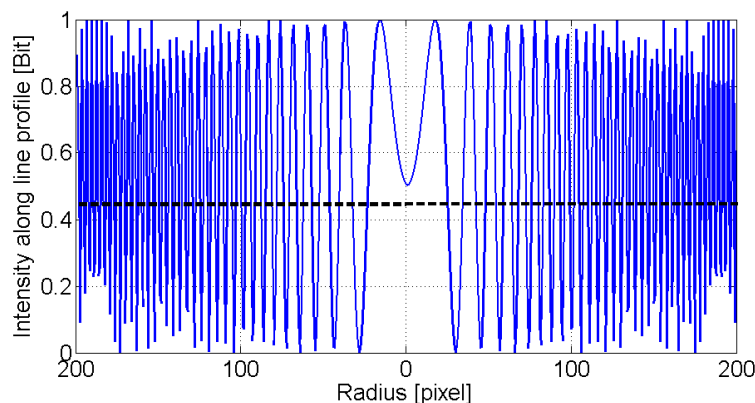
Figure 7.11: Line profile across the Jaehne test image g. The threshold of 0.46 Bit is represented by the black dashed line. Each boundary pixel above this line is considered as a boundary pixel. Note the center disk at r<16, which is defined as boundary pixel, although it is a diffuse background region. This will lead to false positives for small r and drop the accuracy within this region.

The image is processed and the resulting binary image is subtracted from the original image. The resulting difference image is shown in figure 7.12. To interpret the difference image, it has to be kept in mind that:

- The image is the difference between a continuous Gaussian value ([0,1] Bit) and a discrete step function (0 or 1 Bit) for each pixel.

- A true ring pixel has a Gaussian value larger than 0.46 Bit, a true background pixel a value smaller than 0.46 Bit.

There are four classifications possible, each identifiable with a distinct intensity interval, see table 7.1.

	Positive	**Negative**
True	F / F = [-0.54,0] Bit	B /B = [0,0.46] Bit
False	B / F = [-1,-0.54] Bit	F /B = [0.46,1] Bit

Table 7.1: Contingency table with corresponding intensity regions in difference image. F = Foreground, B = Background.

With the given contingency table, it is now possible to calculate the mentioned performance characteristics of the algorithm. The histogram of the intensity distribution of the difference image is shown in figure 7.13. The peaks observed in the histogram at ± 1 and
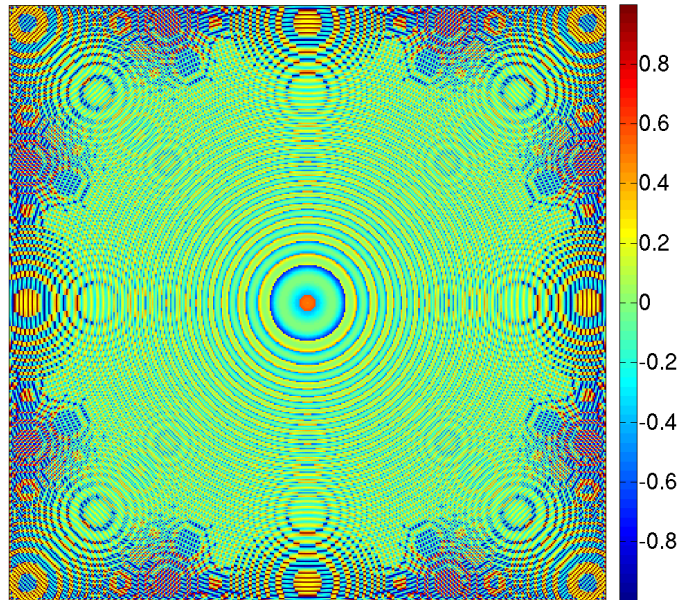
Figure 7.12: Difference image of Jaehne image and binary image. For each pixel, a difference between the intensity value of each pixel in the Jaehne image and the binary image is calculated and assigned to the pixel. The resulting image is color coded.
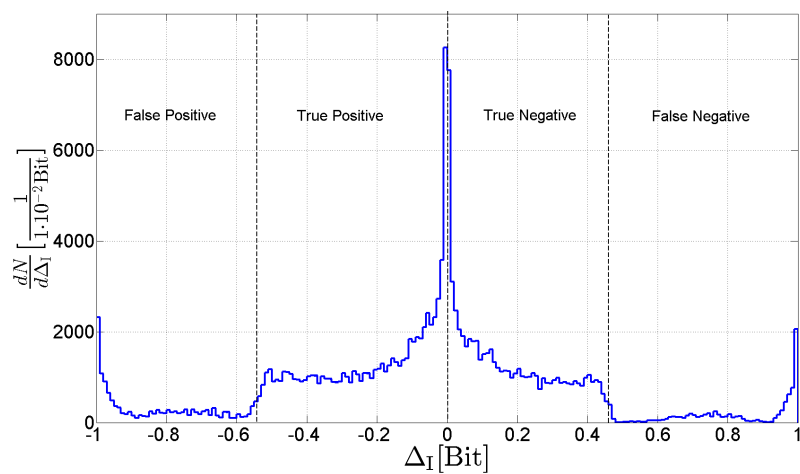
Figure 7.13: The plot shows the histogram of the pixel value distribution of the difference image. The corresponding classification intervals are depicted by dashed black lines.

77

0 Bit is due to the circular shape of the test pattern. With the given intensity distribution, the relative probabilities of the classification cases can be calculated, see table 7.2. The accuracy and the PPV of the algorithm can be calculated to be 85 % respectivly 84 %. But as it can be seen in figure 7.12, these values show a dependency on the radius. Rings

	Positive	Negative
True	47 %	38 %
False	9 %	6 %

Table 7.2: Contingency table with relative probability.

with a large radius have a small distance to the neighboring rings by definition. This can lead to two problems in the processing

1. The slope of the Gaussian profile is too steep. This will introduce an aliasing effect due to the sampling of the profile on a discrete grid. This leads to a wrong classification of the pixel, either false positive or false negative depending on the phase between the slope and the grid and the value of the slope.

2. The distance between two rings is to small. The filtering and smoothing procedure during image processing merges rings and result in a false positive classification.

In figure 7.14, the accuracy is plotted as a function of the radius. There accuracy clearly decreases above a radius of 160 pixels. Within this region with r = 160 pixels, the accuracy is 97 %. Rings with a radius larger than 160 pixels have a distance of four pixels or less and therefore also a high slope. This is the reason for the decrease of accuracy and shows a resolution limitation similar to the result in section 7.2.1, where the USAF test chart shows also a drop in resolution if edges are closer than four pixels. There are two reasons for an accuracy below 100 % at a radius below 160 pixels where both are caused by the very test pattern. The first reason is the region with a radius below 18 pixels. This region is identified as background with image processing code, but defined as foreground since its intensity values are above 0.46 Bit and leads to a false positive classification. The second reason, which is also the cause for the drop in the accuracy at 26 pixels, is the region between the radius of 20 to 30 pixels. A sudden increase in pixels classified as false positive is visible.

Figure 7.15 shows the PPV of the algorithm as a function of the radius. The PPV within a radius of 160 pixels is 97%. In the following, the derived area of each object will be corrected by this constant factor by dividing the calculated area with 0.97. The developed image processing algorithm, optimized for OBACHT images, shows a maximal resolution of 15.63 µm close to the optical system, which is 12.4 µm. Considering the illumination and the resulting contrast variations in the image, the resolution decreases to 35 µm. The accuracy within the resolution limit of the algorithm is 97 %, PPV 99 %. The actual values for the PPV and the sensitiviy for an OBACHT image is reduced by the shot noise. The number of false positives will increase, especially at short distances between two grain boundaries.
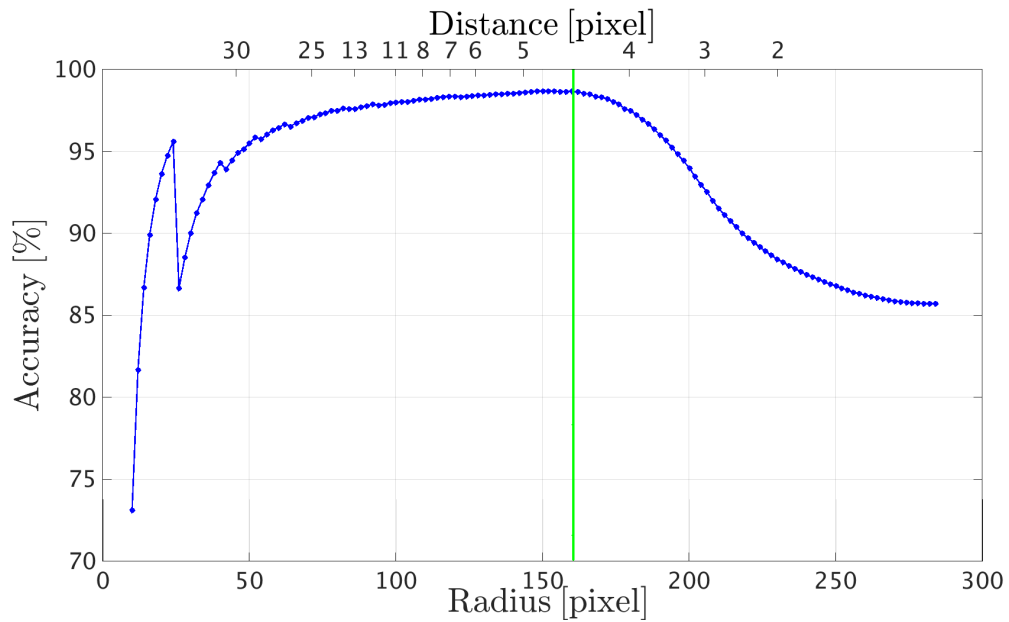
Figure 7.14: Accuracy as a function of the radius. On the lower x-axis the radius r is shown, while the y-axis shows the accuracy for the corresponding circular region with radius r. The upper x-axis shows the distance between two consecutive boundaries at the corresponding radius. The green line depicts the best value and its corresponding radius.
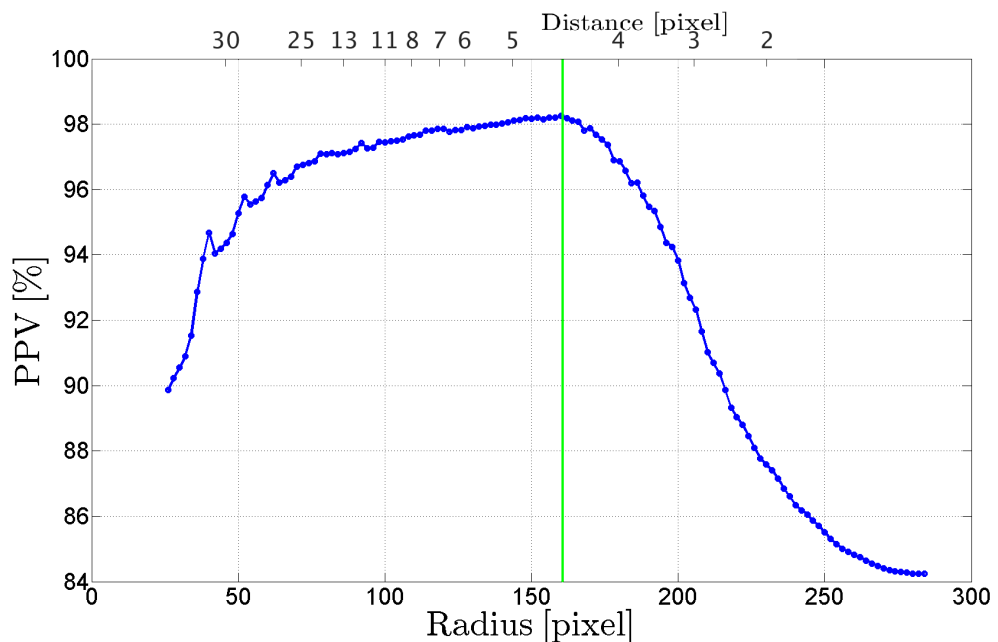
Figure 7.15: PPV as a function of the radius. On the lower x-axis the radius r is shown, while the y-axis shows the PPV for the corresponding circular region with radius r. The upper x-axis shows the distance between two consecutive boundaries at the corresponding radius. The green line depicts the best value and its corresponding radius.

7.3 Definition of Variables

After processing the images, the characteristics of the boundaries can be measured. This procedure is part of the image analysis algorithm. The input of this algorithm is the binary image, including the linked map, produced by the image processing algorithm and the original image. The variables for measurements, used in this thesis, are explained in the following.

7.3.1 Boundary Area

First, the area projected on a single pixel has to be calculated. This is quite simple, since the pixel length on sensor is known to be 1.75 μm and the magnification M was calculated to be 0.51, see section 6.2.2 on page 58. This means, that a surface length of 3.5 μm is projected on a single pixel. The area seen per pixel, or simple "pixel area", is 3.5×3.5 μm^2.

The area of a boundary is simply the number of pixels of this object times the area of a pixel. A more elaborate definition can be found using the image moment $m_{p,q,i}$ [248]

$$m_{p,q,i} = \sum_{x=1}^{M} \sum_{y=1}^{N} x^p y^q ImF(x,y,i) \tag{7.21}$$

where $ImF(x,y,i)$ is the image function, which defines whether a pixel at coordinates (x,y) is part of the boundary with the label i or not, where the value of this function is zero or one respectively. M is the number of columns and N the number of rows of the image. The parameters p, q are any positive integers and define the order of the moment as $(p+q)$. The coordinate origin is the lower left corner of the image. In this notation, the area A of the boundary i is simply the zero-th order moment $m_{0,0,i}$ times the pixel area. Although, this notation seems artificially complicated for this situation, its use will be seen in the context of the other variables described later.

The systematic uncertainty of the grain boundary area converges with $\frac{1}{n^2}$, while n gives the number of pixels of an object. With the given resolution at OBACHT, the experimentally obtained relative error for grain boundaries with 122 pixels is about 1 % , similar to [249].

7.3.2 Boundary Centroid and Density

The centroid position of an object, using the image moment notation, is

$$\vec{R} = \left(\frac{m_{1,0}}{m_{0,0}}, \frac{m_{0,1}}{m_{0,0}} \right). \tag{7.22}$$

with the components

$$\bar{x} = \frac{m_{1,0}}{m_{0,0}} \ , \bar{y} = \frac{m_{0,1}}{m_{0,0}}. \tag{7.23}$$

The component $\bar{x}$ is used to derive the distance of the object from the welding seam and also to classify an object as part of the welding seam, the HAZ or the bulk niobium. The $\bar{y}$ component represents the azimuthal position of an object in the cavity coordinate system. The uncertainty of the centroid under pixel noise is quite stable. With the given resolution at OBACHT, it converges with $\frac{1}{n^2}$, with n being the number of consisting pixels. With the formalism developed in [250], an upper limit of the systematic uncertainty of 2 pixels of the centroid is obtained.

With given centroids of the boundaries in the image, another variable is deduced, the so called object density ρ. It is defined as

$$\rho_i = \frac{n_i}{1\mathrm{mm}^2}$$

with n_i as number of boundaries per square millimeter. Given the image dimensions, 108 squares per image exist and the corresponding densities are calculated. The centroid of a boundary is only counted once, the boundary itself may lie in several squares.

7.3.3 Boundary Orientation

Objects are not 'a priori' symmetric. Hence, it is nontrivial to define properties like diameter or major axis length, eccentricity and orientation of an object. One method to do this, is to define an ellipse which has the same second central moment as the pixel distribution of the pixels [244], which the object consists of, cf. figure 7.16.
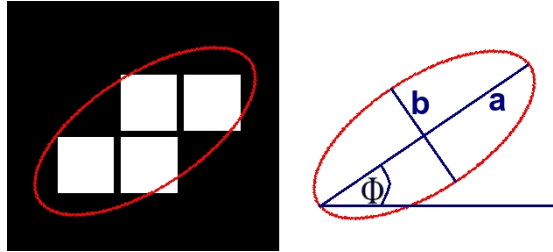
Figure 7.16: On the left side, a four pixel object and the ellipse with the same second central moment is shown. On the right side, the ellipse with its major axis a and minor axis b and the horizontal z-axis for the angle assignment is shown.

To calculate the variables mentioned above, the central moments $\mu_{p,q}$ of the object need to be calculated

$$\mu_{p,q,i} = \sum_{x=1}^{M}\sum_{y=1}^{N}(x-\bar{x})^p (y-\bar{y})^q ImF(x,y,i) \tag{7.24}$$

with $\bar{x}$ and $\bar{y}$ as the x- and y-component of the centroid and $ImF(x,y,i)$ as the image function. Defining a matrix for an object as

$$\begin{bmatrix} \mu'_{2,0} & \mu'_{1,1} \\ \mu'_{1,1} & \mu'_{0,2} \end{bmatrix} \tag{7.25}$$

with

$$\mu'_{p,q} = \mu_{p,q}/\mu_{0,0}. \tag{7.26}$$

The eigenvalues λ_1 and λ_2 of this matrix are the squared lengths of major and minor axis of the object. The central moments are related to the image moments via

$$\mu'_{2,0} = \frac{m_{2,0}}{m_{0,0}} - \bar{x}^2 \tag{7.27}$$

$$\mu'_{0,2} = \frac{m_{0,2}}{m_{0,0}} - \bar{y}^2 \tag{7.28}$$

$$\mu'_{1,1} = \frac{m_{1,1}}{m_{0,0}} - \bar{x}\bar{y}. \tag{7.29}$$

The orientation of an object with respect to the x-axis is calculated via

$$\Theta = \frac{1}{2}\arctan\left(\frac{2\mu'_{1,1}}{\mu'_{2,0} - \mu'_{0,2}}\right). \tag{7.30}$$

With the formalism in [250, 251], an upper limit of the systematic uncertainty of 5 degree is derived. Although it is possible to derive a systematic uncertainty for each object, the upper limit gives enough precision for the needs of this thesis. A circle, with equal moments $\mu'_{2,0}$ and $\mu'_{0,2}$ would lead to an ill-defined angle since the denominator becomes zero. For this case the orientation is defined as 0°.

The numerical eccentricity ϵ is calculated via

$$\epsilon = \sqrt{1 - \left(\frac{\lambda_2}{\lambda_1}\right)}, \lambda_2 < \lambda_1. \tag{7.31}$$

7.3.4 Boundary Roughness

The surface roughness should be reflected in the intensity variations observed in the image. Hence the intensity gradient can be used as a measure for the surface roughness.

Intensity Gradient

The intensity gradient Δ for the gray scale image matrix is calculated for each dimension, z and y using the finite differences:

$$\Delta_{forward,y}(v,w) = I(v,w) - I(v,w+1) \tag{7.32}$$
$$\Delta_{backward,y}(m,n) = I(m,n) - I(m,n-1) \tag{7.33}$$
$$\Delta_{central,y}(s,t) = I(s,t+1) - I(s,t-1) \tag{7.34}$$

and in the same manner for x with I being the gray scale image were v,w, m,n and s,t are particular values of the pixel coordinates in x and y direction. . The finite difference is divided by the step size, and the unit for this obtained variable is $\frac{\text{Bit}}{\mu\text{m}}$. The intensity is
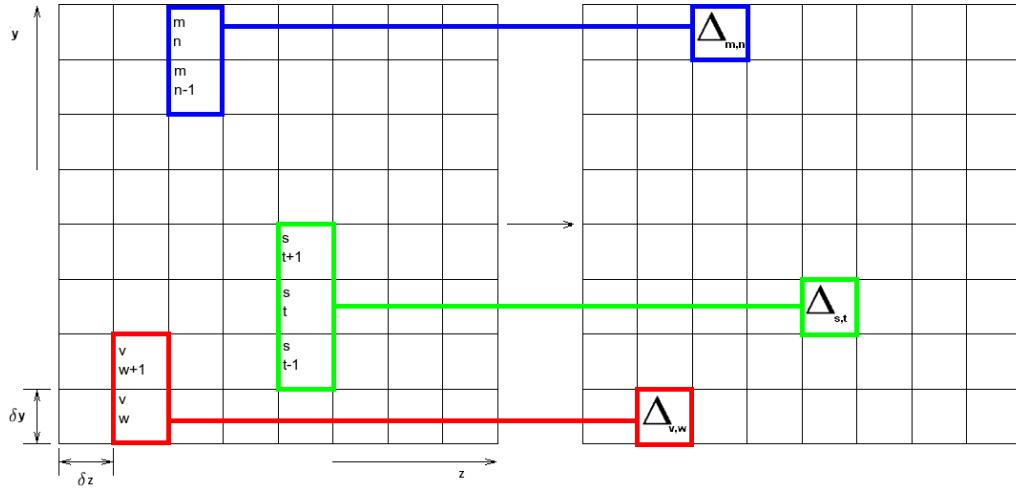
Figure 7.17: Left: Original image with intensity values per pixel. The finite differences in y direction are calculated, from top to bottom. The red box shows the pixels used for the forward difference, the blue box the pixels used for the backward difference and the green box the pixels used for the central difference. Right: The calculated gradient image. The finite differences are assigned to the corresponding central pixel. Applying the algorithm to each pixel in the grid would yield the image matrix g_y.

represented in 256 Bit while the step size from pixel to pixel is 3.5 μm. In figure 7.17 the application of the finite differences on a 8×8 pixels image is shown. This operation generates two new image matrices, g_y and g_y. These images have the same dimension as I and contain the gradient values in x and y direction. To obtain the absolute gradient image G these two images are squared and added

$$G = \sqrt{g_z^2 + g_y^2}. \tag{7.35}$$

Surface slope

Starting with the intensity gradient, a quantity called R_{dq} is introduced. It is based on ISO 25178 for surface texture [252] and represents the RMS of the slope of the profile within the sampling length. R_{dq} is the root mean square of the intensity gradient within the sampled area of the boundary. A steeper slope of a boundary or surface would imply a larger intensity gradient and hence a larger R_{dq}. The R_{dq} can be calculated for each identified bounded object from:

$$R_{dq} = \sqrt{\frac{1}{n}\sum_{x=1}^{M}\sum_{y=1}^{N} G^2\left(x,y\right) ImF\left(x,y,i\right)} \tag{7.36}$$

with $ImF(x,y,i)$ the image function (see equation 7.21) and n the number of pixels of the boundary.

Uncertainty

A statistical noise arises from the *SNR* of the image sensor in the camera, which is 32 dB (see section 6.2.1). The *SNR* of a digital image can be calculated with [253]

$$SNR = 20\log_{10}\left(\frac{I_{max} - I_{min}}{\sigma_{bg}}\right) \tag{7.37}$$

with σ_{bg} as the standard deviation of the noise and I_{max} and I_{min} the highest and lowest intensity value within the image. I_{max} is on the order of 0.9 Bit and I_{min} on the order of 0.1. Hence, σ_{bg} is 0.02 Bit. With given definition of the intensity gradient in equation 7.34, its uncertainty σ_I can be calculated and yields to $\sigma_I = 8.2 \cdot 10^{-4} \frac{\text{Bit}}{\mu\text{m}}$. This leads to a uncertainty for R_{dq} of about $\frac{0.011}{\sqrt{n}}\frac{\text{Bit}}{\mu\text{m}}$ where n is the number of pixels enclosed in a given object.

Systematic noise contributions were identified by performing a systematic study of illumination and focus settings. The influence of different focus settings was shown to introduce a relative uncertainty of 3% of R_{dq}. A much bigger influence of the illumination settings was expected. Six illumination settings, including the default setting, were tested.

- Default Pattern as shown in section 6.3.

- LEDs behind half mirror (Central Illumination) turned off

- All LEDs and LED behind the half mirror turned on

- All LED stripes on the left side of the image turned on

- All LED stripes on the right side of the image turned on

- Only central illumination

Although, these changes are extreme and are not used during the optical inspection, it sets the constraints on the measured variable. To quantify the uncertainty, the average value of the R_{dq} distribution are taken for each illumination setting. The results are shown in figure 7.18. The main contribution to the average of the distribution should arise from the welding seam. Neglecting this area (equal to turning the central illumination off) results in the second data point in figure 7.18. With full illumination , the absolute intensity and therefore the intensity gradient is increased and therefore R_{dq} is also slightly larger. Nevertheless, small details are hard to identify since the image is overexposed, which was reflected in the corresponding area histogram.

With an illumination from only one side, strong uneven shadow patterns are introduced. This is due to the W-cross section of the welding seam. This results in a larger average R_{dq}. The test picture itself was not symmetric due to machining remnants on one side of the cavity, which where further enhanced by the uneven illumination.

The default illumination setup with the sides turned off has an average value close to the normal illumination. This verifies the statement above, that the main contribution of the surface roughness in the image arises from the welding seam region. An upper limit of the systematic error of R_{dq} of 17% due to changes in the illumination pattern was found.
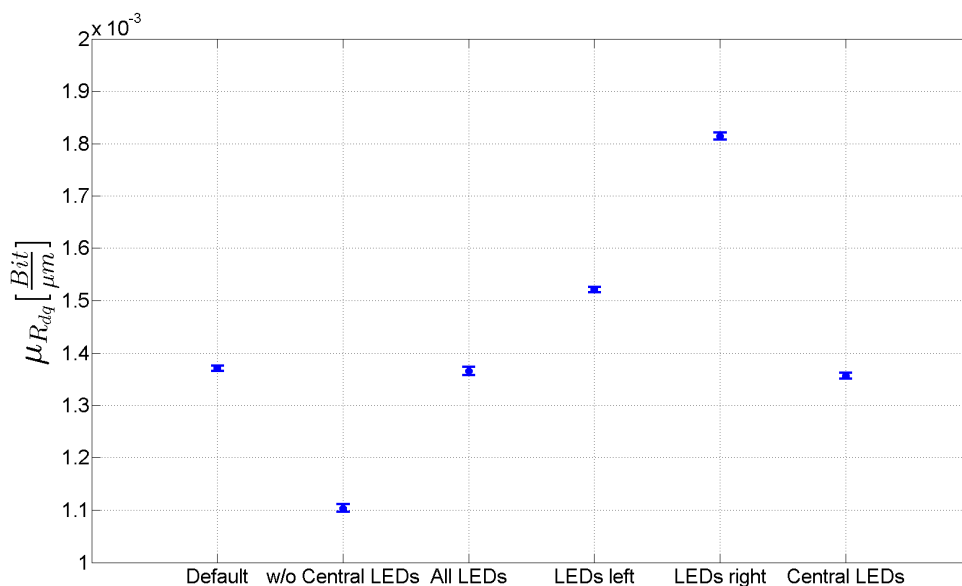
Figure 7.18: The plot shows the µ component of the later defined EMG distribution, see equation 8.2, of the R_{dq} values with a 95% c.i. versus the illumination setup.

7.4 Plausibility Considerations of Variables

Two variables introduced to asses the SRF performance from measurements of surface images, namely boundary area and boundary roughness, are now discussed concerning their effectiveness and plausibility.

7.4.1 Boundary Area

As defined in section 7.3.1, the area of a boundary is simply the number of pixels of this object times the area of a pixel. Since the artificial test patterns are not images taken with OBACHT, the area of a pixel would be an artificial number and is neglected. Hence, the area of a boundary is just a number of pixels for this consideration. For the grain boundary area observed in an OBACHT image, the grain boundary area is the pixel number multiplied with the pixel area.

Test Pattern

The used test patterns can be seen in figures 7.19 and 7.20, left the 25 pixels grid, right the 50 pixels grid. Given the geometry of the test pattern - total area of 300×300 pixels, boundaries with a thickness of 3 pixels and squares with a side length of 22 and 47 pixels respectively - the area of each object can be calculated. The area of a square is $22^2 = 484$ pixels respectively $47^2 = 2209$ pixels. The average area of a square, as found by the algorithms, is 483 pixels and 2204 pixels. The slightly smaller numbers found by the algorithm can be explained with the design of the image processing algorithm. The
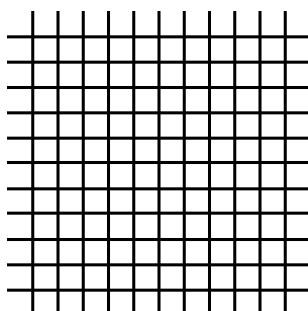
Figure 7.19: Test pattern with squares of a side length of 22 pixels and 3 pixels thick boundaries and a total area of 300 × 300 pixels.
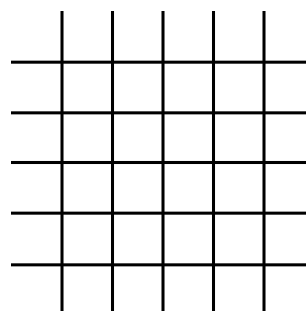
Figure 7.20: Test pattern with squares of a side length of 47 pixels and 3 pixels thick boundaries and a total area of 300 × 300 pixels.

algorithm was designed to detect the boundaries in an image, which are defined as pixels with an intensity gradient above a local threshold. Some pixels close to a crossing of two boundaries can be falsely identified as part of the boundary, as shown in figure 7.21. The formula for the boundary area A is

$$A = 2 \cdot (n \cdot 3 \cdot 300) - (n^2 \cdot 9) + (300 \cdot 2) - (2 \cdot n \cdot 3) \qquad (7.38)$$

where n represents the number of lines in one direction. The first term describes the total area covered by the lines. The second term corrects the area for the double-counted area of the intersections of the grid lines. The third term adds the 2 pixels thick line at the right and bottom edge. The fourth term corrects the area for the double counted area of the intersection between the grid lines and the lines at the two edges. The area of the boundary can be calculated to be 9345 pixels respectively 19245 pixels.

The area of the boundary, as found by the algorithms, is 9487 pixels and 19819 pixels. The values are 1.8 % and 2.9 % respectively above the true area or 143 pixels and 575 pixels in absolute numbers. With the arguments mentioned above, that boundary pixels are pixel above a certain intensity gradient, this observed difference can be calculated for the test pattern. The false positive pixels are the outer corner pixels at the intersections of lines or with an edge, c.f. figure 7.21. The total number of false positive pixels can be calculated via

$$A = (n^2 \cdot 4) + (2 \cdot n \cdot 2) + (2 \cdot n \cdot 2) + 3 \qquad (7.39)$$

where n represents the number of lines in one direction. The first term are the false positive pixels at the intersections of two grid lines. The second and third term represents the false positive pixels created at the intersection of the grid lines with the edges of the image. The fourth, constant, term is the contribution of the 2 pixels thick lines at the right and bottom image edge. For the 25 and 50 pixels grid, the number of false positive pixels are 143 and 575 pixels, which equals the difference of the area found by the algorithm and the true area.

Summing up, the boundary area as derived by the image processing algorithm behaves as
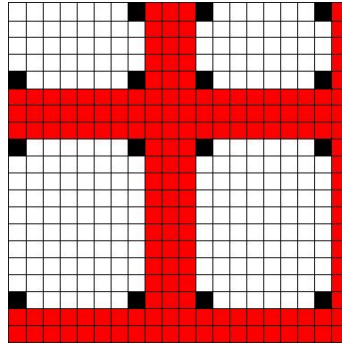
Figure 7.21: Test pattern with false positive pixels. The red pixels are true boundary pixels. Black pixels are false positive pixels of the boundary because of a higher intensity gradient than the average background pixels.

expected. The relative error is in the same order of magnitude as found with the image processing accuracy benchmark in section 7.2.2.

Grain Boundary

The area of the same grain boundary with different visibility due to different surface treatments [217, 254], as shown in figure 7.22, is calculated. The single grain boundary under investigation is running from the lower left to the upper right corner. After the
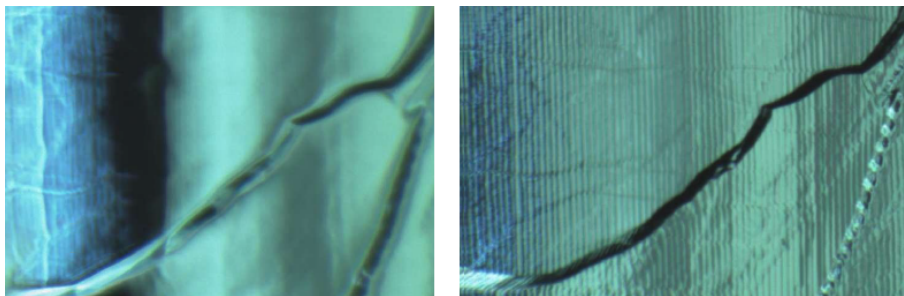
Figure 7.22: OBACHT image of the same boundary after EP (left) and BCP (right) [217].

image processing, the area of the boundary was derived and can be seen in table 7.3. The grain boundary area between the two surface treatments differ by almost a factor

	EP	BCP
Area $\left[\text{mm}^2\right]$	0.05	0.10

Table 7.3: Area of the same grain boundary after different treatments as found by the algorithm.

two. The different surface treatments result in different grain boundary slopes. With the given illumination system, this influences the optical visibility of the boundary, see

section 6.3. As the boundary slope gets smoother, more of the boundary area is visible. Hence, a connection between the boundary roughness and the visible boundary area exist. However they are not exchangeable variables, since the visible boundary area is a function of the boundary slope as well as its width and length.

7.4.2 Boundary Roughness

The variable R_{dq} defined in section 7.3.4 represents one aspect of the general property of surface roughness, namely the local slope of a grain boundary step. This definition of surface roughness is often used to describe repetitive roughness profiles, which is the case for the grain boundary structure.

Empirical Interpretation

The derived boundary roughness parameter R_{dq} is only an indirect measurement of the surface slope. Hence, only a general statement on the surface texture can be given with this parameter. As an example, the boundary which was already shown in figure 7.22 is used and R_{dq} has been calculated, and results are given in table 7.4. The boundary slope

	EP	BCP
$R_{dq} \left[10^{-3} \frac{\text{Bit}}{\mu\text{m}} \right]$	7.3	11.6

Table 7.4: Roughness parameter of the same grain boundary after different treatments as found by the algorithm.

for the EP treated grain step was found to be 37% smaller than the slope for the BCP treated grain step. This is in agreement with the expected surface topography after such treatments, see chapter 8 for details.

Comparison with Profilometric Results

If the assumption that R_{dq} is proportional to the surface roughness is true, a correlation between profilometric and optical roughness measurements should be found. To deduce a conversion factor, a replica of a cavity surface was made in the course of this thesis and afterwards scanned with a laser profilometer (UBM Microfocus Expert). The step size of the profilometric scan was 3.5 μm in x- and 12.5 μm in y-direction. The lateral resolution is 0.06 μm. A set of 934 × 334 data points were taken and an area of 3269 × 4175 μm^2 was covered. Four edges were identified in the area scanned with the laser profilometer. The gradient was measured for each pixel and averaged for the whole boundary. The same edges were located and the intensity gradient was measured with the help of only the optical image. In figure 7.23 the measured edge gradient and the by the algorithm deduced intensity gradient are compared, together with a linear fit for calibration.
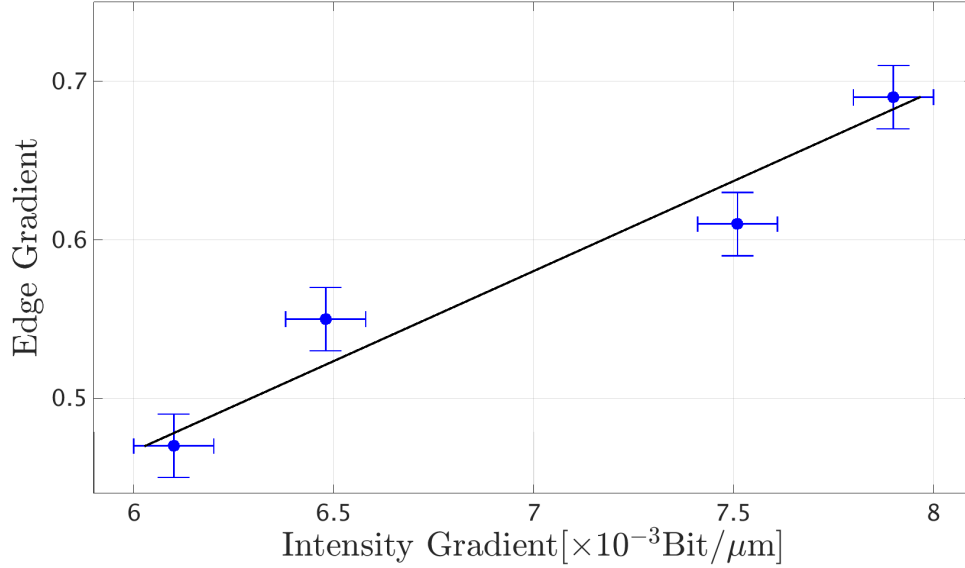
Figure 7.23: The x-axis shows the intensity gradient of a boundary derived from the image and the y-axis the geometrical gradient measured with the profilometer. The linear fit with the equation is shown.

A conversion function f was derived:

$$f(x) = (113.58 \pm 9.95)\frac{\text{μm}}{\text{Bit}} \times x - (0.06 \pm 0.07)\frac{\text{Bit}}{\text{μm}} \qquad (7.40)$$

With this fit, the geometrical slope of the boundaries in the image can be calculated. The slope histogram for a sample using the above fit and compare it with a measured slope histogram of another sample.

In figure 7.24 such a comparison is shown. The histogram in the left is taken from [132]. It was derived from a height profile along a line of a niobium sample, after the removal of 120 μm with BCP. The histogram on the right depicts a single image of a cavity with the same treatment as the sample in the paper taken with OBACHT and analyzed with the algorithm. Although the peak of both distributions are in the same bin and the distributions look similar, the relative counts are different. The different magnitudes of the absolute counts are due to the different sample sizes. The rather hard cut-off at 20 degrees on the right histogram can be explained with the resolution limit of OBACHT with given illumination set up, see section 6.3 for details.

The reason for the different relative counts is the different sensitivity of the two approaches for small angles with respect to each other. As mentioned in the paper [132], describing the profilometric approach, only steps larger than a few micrometers were considered. This means, a general underestimation of the amount of small angles is inherent in the method. On the other hand, an overestimation of the amount of small angles in the here discussed optical approach is inherent due to shot noise. Shot noise creates intensity fluctuations, even in homogeneous intensity regions and therefore an increase in the
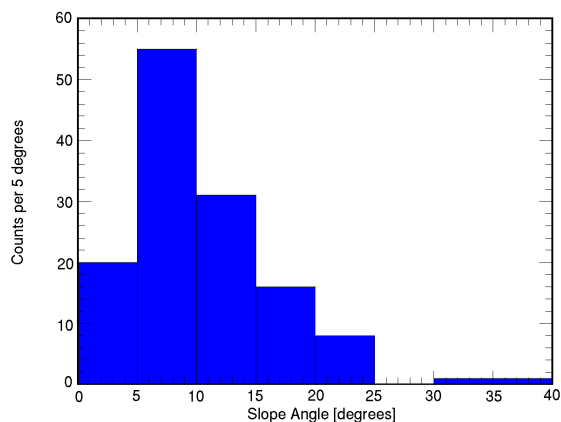
Figure 7.24: Slope angle histogram obtained from a height profile along a line [132].
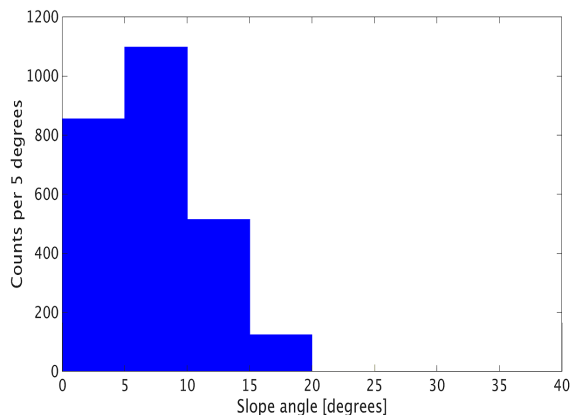
Figure 7.25: Slope angle histogram obtained from the intensity gradient distribution.

amount of small angles.

Still, the most likely value and the maximum value are in good agreement. This is quite remarkable since the conversion factor was measured with an independent sample and R_{dq} is deduced only with optical methods. With given results, the assumption that R_{dq} is a variable which is proportional to the cavity surface roughness is justified and that R_{dq} should be sensitive to the difference in the surface roughness due to different surface treatments.

Furthermore, this resolution is sufficient for the analysis of a possible magnetic field enhancement mechanism, described in [132]. Figure 7.26 shows the field enhancement factor β as a function of the slope angle. With the angle resolution of OBACHT, bound-
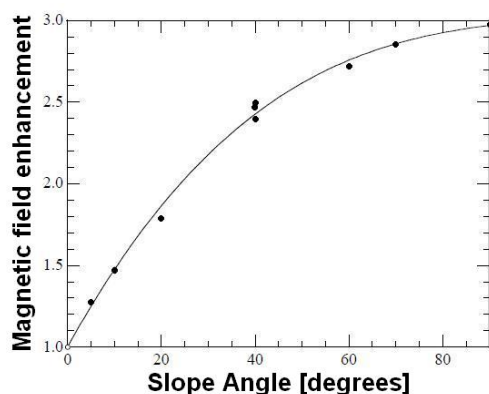
Figure 7.26: Magnetic field enhancement factor β versus the slope angle [132].

aries with an enhancement of the magnetic field of about 80% can be resolved. Hence, OBACHT is sensitive to investigate a possible limitation of the cavity generated by this mechanism.

CHAPTER 8

Surface Characterization by means of Optical Surface Properties

The image processing and analysis algorithm is now applied to the niobium surface after various chemistry treatment steps. Since the surface characteristics before and after the application of surface chemistry is well known, its evolution is an useful test case for the image analysis approach.

First, the well known surface states will be described and how those should be reflected in the images. Then, variables in which these surface properties should be seen are analyzed and discussed and a comparison between the expected outcome of the algorithm and standard measurements is done. This will asses the ability of the image processing code and in addition, a characterization of the cavity surface is achieved. To reduce the systematic uncertainties, the illumination pattern kept the same for all. Thus, a surface characterization of the treated inner cavity surface is derived.

8.1 Description of Surface Topography

After the removal of a 140 µm thick surface layer by chemical treatment, the surface characteristics change drastically. A visualization of two atomic force microscope (AFM) scans of a niobium sample before and after surface chemistry is shown in figure 8.1. In general, the average surface roughness decreases by three orders of magnitude as the grains emerge owing to the surface chemistry [255]. On the other hand, because of the emergence of the grain boundaries, more pronounced height steps on the surface occur. Since R_{dq} is a local property of a boundary, it is expected that it increases due to the treatment. In [256], the R_{dq} of the surface topography of niobium samples with different surface states was measured with an AFM. In all cases, R_{dq} increased significantly in comparison to the untreated sample, but less for the EP treated samples as compared to the BCP samples.

91
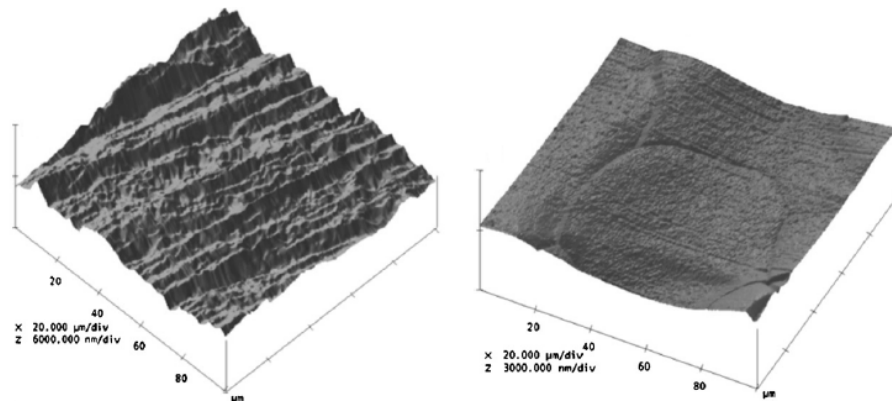
Figure 8.1: AFM images from niobium samples with a scanning area of 100×100 μm^2 [255]. Left: Untreated surface sample. Right: Electropolished surface sample. A decrease in roughness but an enhancement of grain boundaries can be seen.

The welding seam region needs to be investigated separately, since the heating due to the electron beam welding allows a recrystallization of the material. In an untreated cavity, the fishbone pattern dominates the optical characteristics of the welding seam, while after the surface treatment, the underlying crystal structure emerges, as can be seen in figure 8.2.
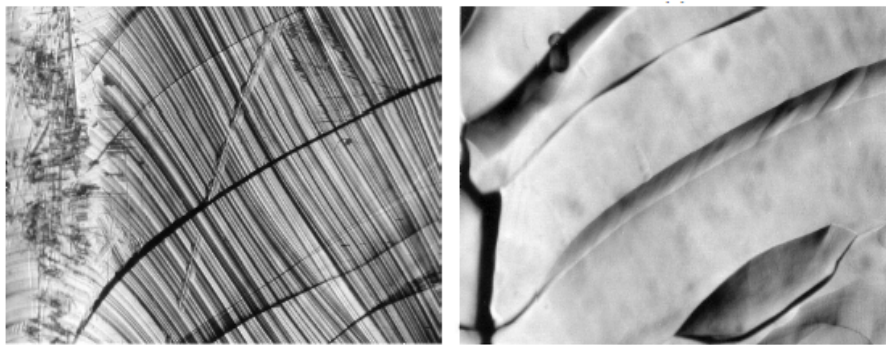
Figure 8.2: Optical microscope image of the same welding seam surface (1770×1370 μm^2) [176]. Left: Untreated cavity. Right: BCP treated surface. The fishbone pattern (left image) are thin lines going from top left to bottom right. The grain boundaries are also visible but not dominant. The grain boundaries (right image), going from bottom left to top right, show a preferred orientation.

The fishbone pattern forms during the welding procedure as a consequence of the electron beam moving pattern called weave bead. Below this surface layer, the niobium crystals have elongated dimensions, with a length of the order of the half width of the welding seam. As a consequence of the melting and recrystallization of the niobium grains, the boundaries show a preferred orientation w.r.t. the horizontal image axis. The exact angle depends on the feed rate and current of the electron beam.

8.2   Optical Dataset

Two cavities were inspected before and after surface chemistry. After a first inspection, they were sent back to Ettore Zanon and underwent the BCP Flash scheme [154] with a total removal of a 150 μm thick surface layer.

During the inspection of the first untreated cavity at OBACHT, a problem arose with the image positions, mentioned in section 6.1.3. Due to the cavity tuning before chemistry, a longitudinal offset between the true equator welding seams and the intended position was introduced. This led to an offset of the image axis and the equatorial welding seam. After the experience with this cavity, a calibration procedure for OBACHT was implemented. An example of the offset can be seen in figure 8.3. It had to be manually corrected for each equator for the first inspection of the cavity to enable a comparison between the subsequent inspections.
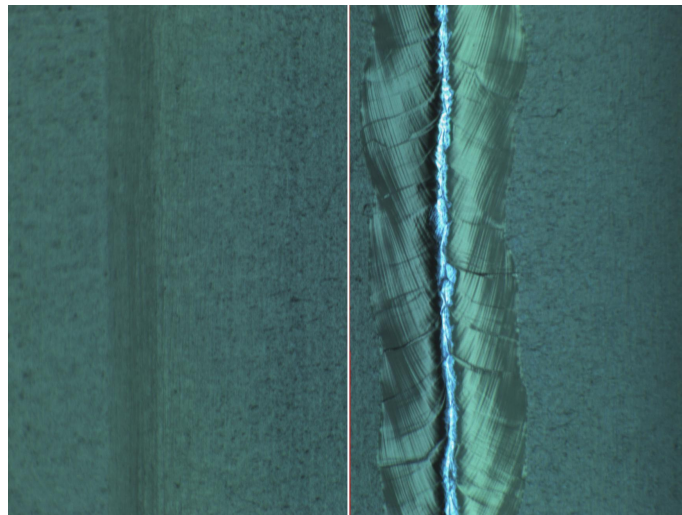
Figure 8.3: Image of the untreated cavity surface, equator 9. An offset between the image axis (white line) and the welding seam ridge of 1.8 mm is visible.

8.3   Results

The variables, which will be discussed, are retrieved individually for each boundary in the OBACHT image. As previously mentioned, the welding seam region shows other properties than the heat affected zone. Therefore, in general the variables will be discussed separately for those regions. Objects are associated with the welding seam if their centroid is within a region of $\pm 2\,\text{mm}$ from the calibrated image center axis.

8.3.1 Total Number of Boundaries

As seen in figure 8.1, the surface structure changes drastically during the surface chemistry. It is obvious that the untreated niobium surface has a significantly larger number of boundaries than the treated sample. OBACHT will average out some of these structures, since the scanned area of 100×100 µm^2 is projected onto 30×30 pixels, see section 6.2.2. Still, the amount of boundaries before any surface treatment is expected to be significantly larger than after a treatment. In table 8.1 the average number of boundaries per equator is shown. Although those are just average values, the trend is visible for all individual equators and the total amount of boundaries is reduced by 49% due to the surface treatment.

	WS	HAZ
Untreated	163250 ± 26280	248850 ± 27278
Treated	58020 ± 4676	149050 ± 5757
Change	$-64 \pm 6\,\%$	$-40 \pm 7\%$

Table 8.1: Average number of boundaries found in the welding seam region and the heat affected zone of 18 equators with 95% c.i..

8.3.2 Boundary Density

As shown, the total amount of boundaries found by the algorithm after treatment decreases as expected. In this context, the development of the boundary density is of interest. The density is defined in section 7.3.2 and is the total number of boundary centroids in a unit square with an area of 1 mm^2.

The fabrication procedure of niobium sheets produces an uniform grain size [257]. This should lead to a Gaussian distribution of the density after treatment. The melting and recrystallization procedure during EBW introduces a grain size in the welding seam region different from the heat affected zone, but again with a uniform grain size. Hence, the total boundary density should be a composition of two Gaussian distributions.

In an untreated cavity, the regular fishbone pattern of the welding seam should create a distinct density. Also, the heat affected zone looks like a homogeneous region because of the optical resolution, since the microstructure is averaged out. This leads to a uniform looking surface with artificial and rather small boundaries. This means that the density before the treatment should also be the sum of two Gaussian distributions. The measured average boundary densities of the two treated cavities are shown in figure 8.4.

For a quantitative statement, each density of the 18 untreated and 18 treated equators was fitted with a sum of two Gaussian distributions.

$$\rho(n) = A_1 \cdot e^{-\frac{1}{2}\left(\frac{n-n_{0,1}}{\sigma_1}\right)^2} + A_2 \cdot e^{-\frac{1}{2}\left(\frac{n-n_{0,2}}{\sigma_2}\right)^2} \tag{8.1}$$
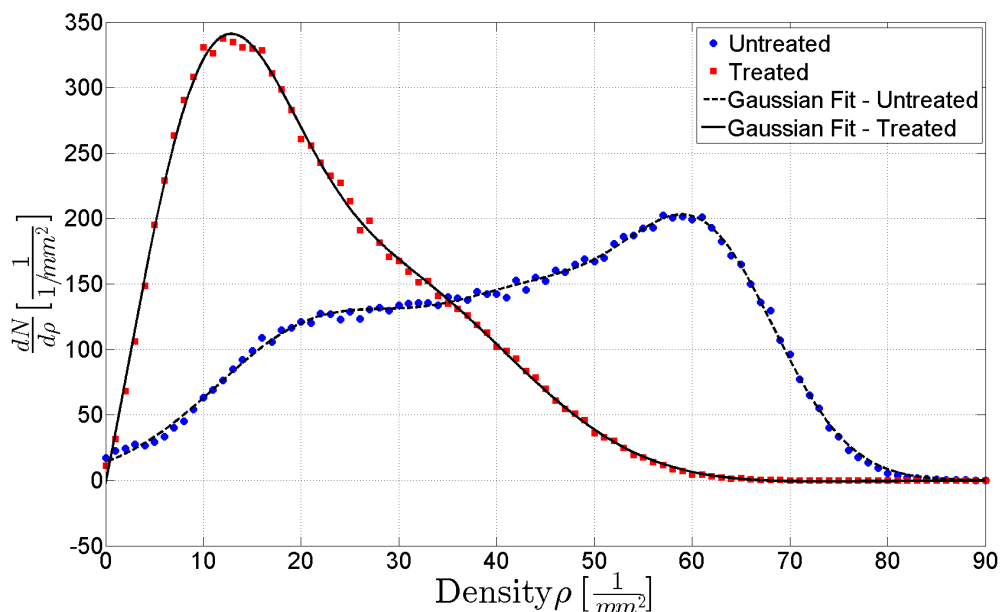
Figure 8.4: Grain Boundary density distribution. The x-axis shows the boundary density. The y-axis shows the amount of squares found with the respective density per equator. The blue dots describes the distribution before, the red squares after surface treatment. The distributions are sums of two Gaussian distributions, which are depicted by black lines. See figure 8.5 for the spatial distribution.

with A_i as the amplitude for the individual component, $n_{0,i}$ the average density and σ_i the standard deviation. The weighted average fit parameters are given in table 8.2. To further understand the measured distribution and confirm the assumption of two Gaussian distributions, the spatial distribution of the density over a typical OBACHT picture is shown in figure 8.5 as color-coded two dimensional histograms. The spatial distribution of the boundary densities supports the model that each of the two distinct regions has an individual Gaussian distribution. The deficiency visible on the right side of the upper histogram is a consequence of the missing image parts after the offset correction.

$\left[\frac{1}{mm^2}\right]$	WS		HAZ	
	n_0	σ	n_0	σ
Untreated	25.23 ± 0.42	22.85 ± 0.67	65.54 ± 0.34	13.85 ± 1.07
Treated	13.16 ± 0.05	9.15 ± 0.22	25.72 ± 0.05	17.65 ± 0.70

Table 8.2: Results of the fit, with n_0 as the mean and σ as the variance of the Gaussian distribution for the boundary densities in the welding seam region and the heat affected zone with 95% confidence intervals.

The highest densities with a rather narrow width, before and after treatment, are found in the heat affected zone. This reflects the uniform surface before the treatment and the
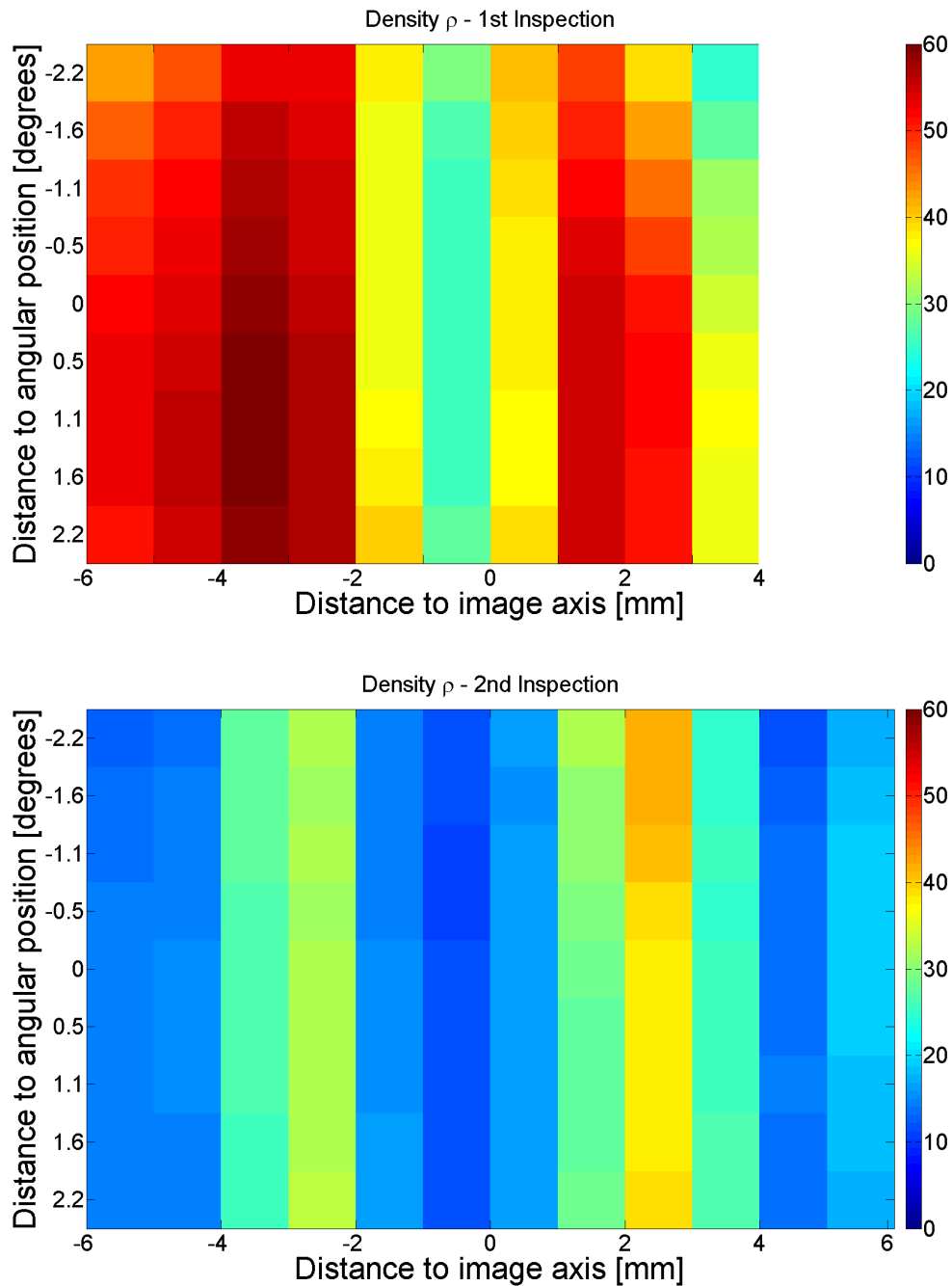
Figure 8.5: Spatial grain boundary density distribution. The x-axis shows the position of the square w.r.t. the image symmetry axis. The y-axis shows the position of the square w.r.t. the angular image position. The color represents the density in $[\frac{1}{mm^2}]$. The upper histogram shows the density before the surface treatment, the lower histogram after the surface treatment. In each histogram, the welding seam ($\leq \pm 2mm$) and the heat affected zone ($> \pm 2mm$) can be identified as zone with distinctive densities.

96

uniform grain structure after the treatment. The welding seam with the fishbone pattern shows a large standard deviation. This is a consequence of the shot noise, see section 6.2.1. Single bones of the fishbone pattern can be connected during the image processing. Hence, multiple fishbone lines fuse into a single boundary, so that the density fluctuates drastically and introduce this large spread in the density. This is due to the limited resolution of the algorithm, described in section 7.2. The grains in the treated welding seam region are larger than the grains in the HAZ. Therefore, the density in the welding seam must be smaller, which is observed.

A plausibility check of the values for the grain boundary density ρ can be performed by obtaining an estimate of the grain size from this data. The area of a square is $1mm^2$. Dividing this area by the observed density yields to an average grain boundary area. With this value an average grain size can be calculated. This grain size, given in diameter, is about 150 μm for the heat affected zone and about 400 μm for the welding seam region. Those values are in agreement with observed grain sizes in the heat affected zone and the welding seam after fabrication, see table 4.3 on page 39. In conclusion, the observed grain boundary density ρ is within reasonable limits.

Summing up, it has been shown that the boundary density is a surface property which behaves as expected and is a simple classifier whether the surface underwent a chemical treatment or not. The average boundary density decreases by 60% in the heat affected zone and by 47% in the welding seam region due to surface treatment.

8.3.3 Boundary Area

As seen in figure 8.1, small structures vanish and the grain structure evolves during the surface treatments. This is reflected in the boundary density, but should also be visible in the boundary area found by the algorithm. Less small boundaries and more large boundaries should be visible after the chemical treatment.

In figure 8.6, the area distributions before and after the treatment are shown. The binning value of 980 μm^2 is chosen because it is exactly divisible by the pixel area and pixel number, equaling a square with a side length of twice the OBACHT resolutions. This bin size allows good visualization. As can be seen in the plot, depicted by the gray shaded area, additional large boundaries evolve. On average, the integrated area of all evolving grain boundaries is 1 ± 0.4 mm^2 per image. At the same time, a reduction of small boundaries is seen, with a corresponding average of the integrated area of all removed grain boundaries of 7.1 ± 0.5 mm^2 per image. This observation is again in agreement with the expectation, since the grain structure evolves and the microstructure vanishes or gets smoother.

To quantify the observed distribution, more information is needed. Experimental and numerical studies have shown an inverse correlation between the population densities of boundaries $\frac{dN}{dE}$ and the grain boundary energy E [258–261]

$$\frac{dN}{dE} \propto E^{-\alpha}.$$
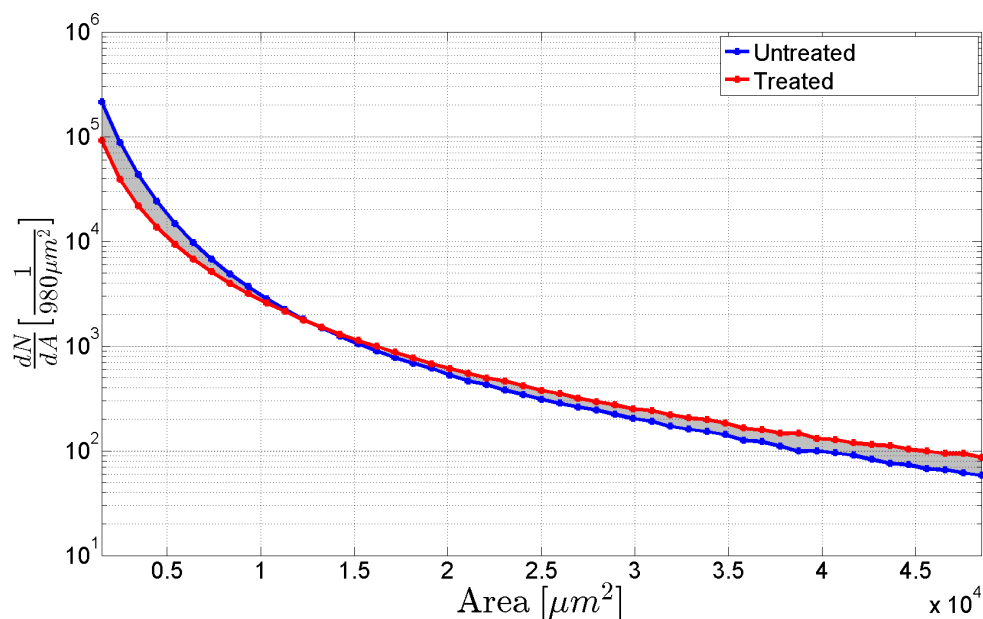
Figure 8.6: Grain boundary area distribution. The x-axis shows the boundary area, while the y-axis shows the count per 980μm^2. The area distribution before (blue) and after (red) the surface treatment is shown.

Results from experiments and simulations suggest that there is a relationship between the energy of a grain boundary and its total area A [262–265]. The physical reason for this correlation is the misfit between atoms across the boundary. The deviation of atom positions from the perfect lattice leads to a higher energy state. Hence, a larger grain boundary area implies more deviations and a higher energy of the grain boundary

$$E \propto A.$$

And even though the observed grain boundary structure is only a cut through the three dimensional grain boundary network, it is possible to relate the observed surface area to the grain boundary [259, 266]. Hence the correlation between population densities and the grain boundary area can be expected to be

$$\frac{dN}{dA} \propto A^{-\alpha}$$

where the scaling coefficient α remains to be determined. The simplest approach to quantify this coefficient are inverse power law distributions. The scheme to derive the power law coefficients, evaluate the uncertainties and check the plausibility of the model is described in detail in [267–269].

An example of a fit can be seen in figure 8.7, which shows the theoretical power law distribution and the experimentally found distribution for an untreated equator. A good agreement was found over three orders of magnitude. In table 8.3, the average scaling
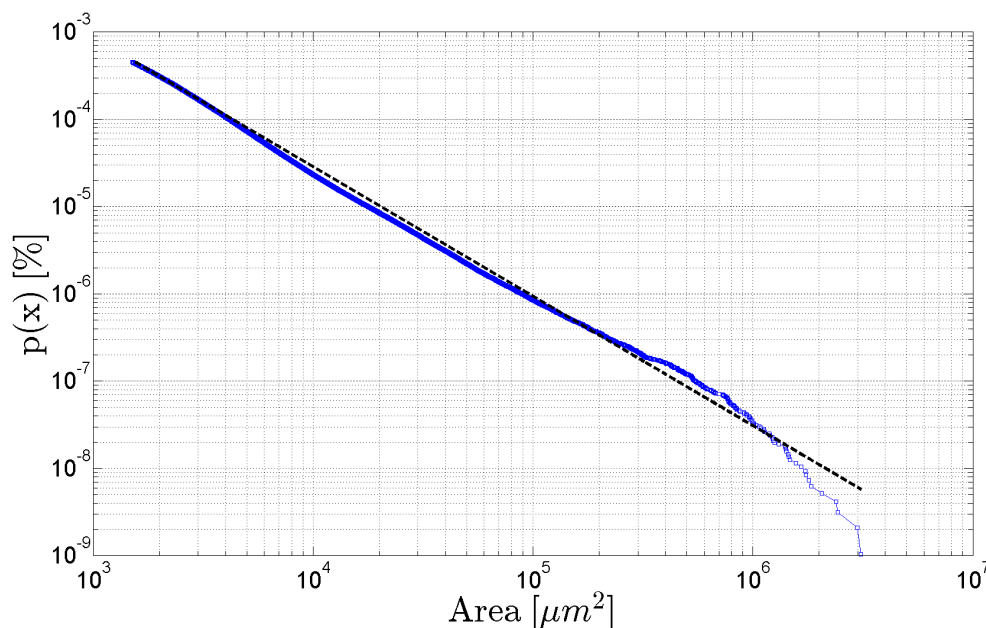
Figure 8.7: This double logarithmic plot shows the probability of occurrence of a grain boundary area versus the very grain boundary area. The blue squares depict the experimental found distribution, the black dashed line the power law fit.

coefficients, distinguished for the zones, for the 18 treated and 18 untreated equators are shown. The standard error on the estimated α is $\frac{\alpha-1}{\sqrt{n}} + \mathscr{O}(\frac{1}{n})$ [267]. With given boundary counts, the uncertainty is in the order of $\mathscr{O}\left(10^{-3}\right)$ and can be neglected since it is smaller than the cell-to-cell deviations. The scaling coefficients from table 8.3 decrease on aver-

	α	α_{WS}	α_{HAZ}
Untreated	2.30 ± 0.09	2.63 ± 0.09	2.51 ± 0.13
Treated	2.03 ± 0.03	2.17 ± 0.02	2.18 ± 0.03

Table 8.3: Fit parameter α for the power law distribution with 95 % confidence interval for the whole image and for the welding seam region and the heat affected zone.

age by 11% during the surface treatment, as a consequence of the emergence of the larger grain boundaries. The welding seam is more affected than the heat affected zone. This is due to the small fishbone boundaries which vanish and the much larger grain boundaries appear.

A good agreement between the experimental and the power law distribution was found, which allows a simpler and better defined characterization of the surface state. Accompanying the theoretical description, the behaviour of the variable meets the expected outcome of the measurement.

8.3.4 Orientation of Welding Seam Boundaries

The orientation of the boundaries is measured w.r.t. the horizontal images axis. The welding seam of the untreated cavity is dominated by the fishbone pattern which has a preferred angle, depending on the electron beam weave bead. The histogram of the boundary orientation of an untreated equator as found by the algorithm is shown in figure 8.8. It includes only welding seam objects with a high numerical eccentricity $\varepsilon \geq 0.95$, because they represent thin, elongated boundaries of the fishbone pattern.
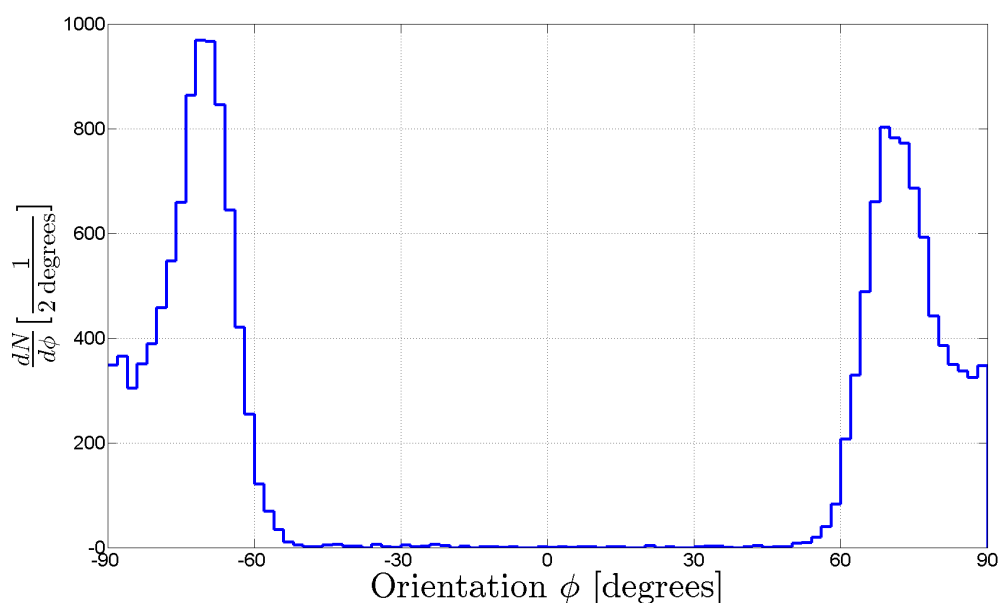
Figure 8.8: The x-axis shows the orientation of the boundaries in degrees. The y-axis shows the counts per 2 degree. The values used here are from the first equator of an untreated cavity.

In the histogram, two peaks at $\pm 70^{\mathrm{o}}$ can be seen, where those arise solely from the fishbone pattern. In addition, a valuable classifier can be constructed with this variable: If the individual boundary orientation is combined with the boundary centroid $\vec{R}$ (see section 7.3.2) two types of fishbone pattern can be identified, see figure 8.9. With the known characteristics of the fishbone pattern types, it is possible to identify those types automatically. As an example, a two dimensional histogram of the boundary orientations and centroids is shown in figure 8.10.

A-like Pattern V-Like Pattern
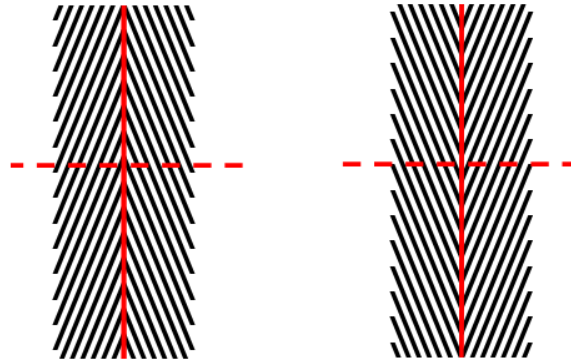
Figure 8.9: A schematic drawing of the two possible fishbone patterns. An A-like pattern will have boundaries left of the image axis with a positive angle w.r.t. the dotted line and the boundaries on the right will have a negative angle. The V-like pattern has mirrored characteristics.
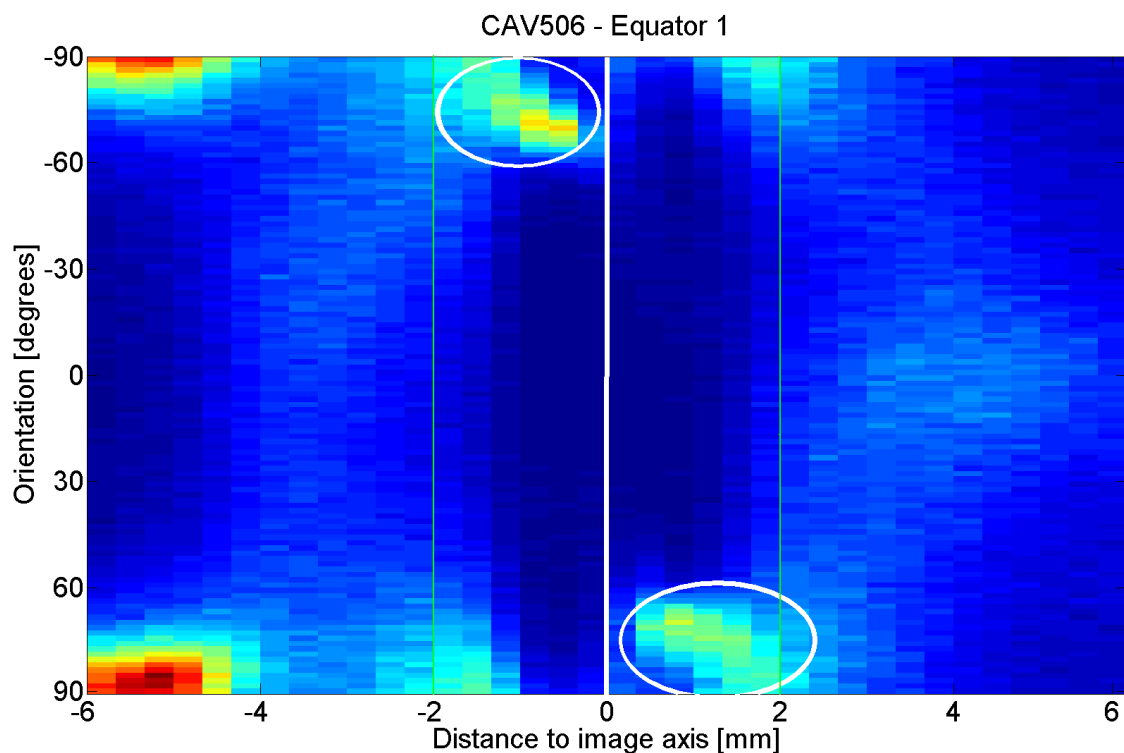
Figure 8.10: The x-axis shows the boundary centroid in millimeter with respect to the image axis. The y-axis shows the boundary orientation in degrees w.r.t. an axis perpendicular to the welding seam. The white line depicts the image axis. The V-like fishbone pattern can be clearly identified in the histogram as islands (encircled). The two peaks at (-6 mm, $\pm 90°$) in the histogram are remains of the machining of the dumbbells. The thin green lines at ± 2mm show the defined welding seam region.

101

The V-like fishbone pattern can be easily identified with the given variables. The combination of orientation and centroid as a classifier will be used in detail for a comparison of the vendors in section 9.2.4.

After the surface treatment, the fishbone pattern vanishes and the grain boundaries become visible. The boundary orientation is a consequence of the electron beam welding. Figure 8.11 shows the histogram of the boundary orientations in the welding seam region after the surface treatment. The histogram includes boundaries from the welding seam region with a numerical eccentricity $\varepsilon \geq 0.95$.
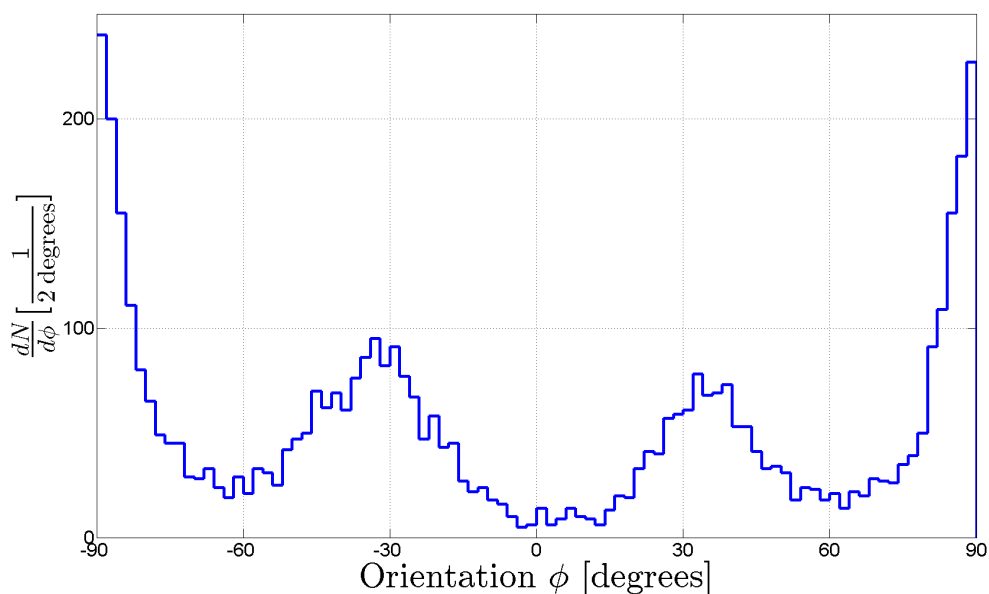
Figure 8.11: The x-axis shows the orientation of the boundaries in degrees. The y-axis shows the counts per 2 degree. The values used here are from the first equator of a treated cavity.

Two peaks at $\sim \pm 32^o$ can be seen. Those peaks arise from the grain boundaries in the welding seam region. The peaks at $\pm 90^o$ represent the welding seam borders.

In summary, the orientation of the boundaries is an obvious property and a simple test case for the algorithm. The resolution of individual boundaries by the algorithm as well as the elliptical fit approach to derive the orientation (see section 7.3.3) perform as expected. In addition, the orientation/centroid classifier introduced will allow detailed analysis of the welding process.

8.3.5 Boundary Roughness

Since surface chemistry reduces the amount of boundaries in terms of absolute numbers, density and total covered area, the average roughness decreases. But R_{dq} is a measure of the average local gradient which depends on the local slope of a boundary. An enhancement of grain boundaries should increase the geometric gradients on the surface. Figure 8.12 shows the change of the R_{dq} distribution due to surface chemistry. While the distri-
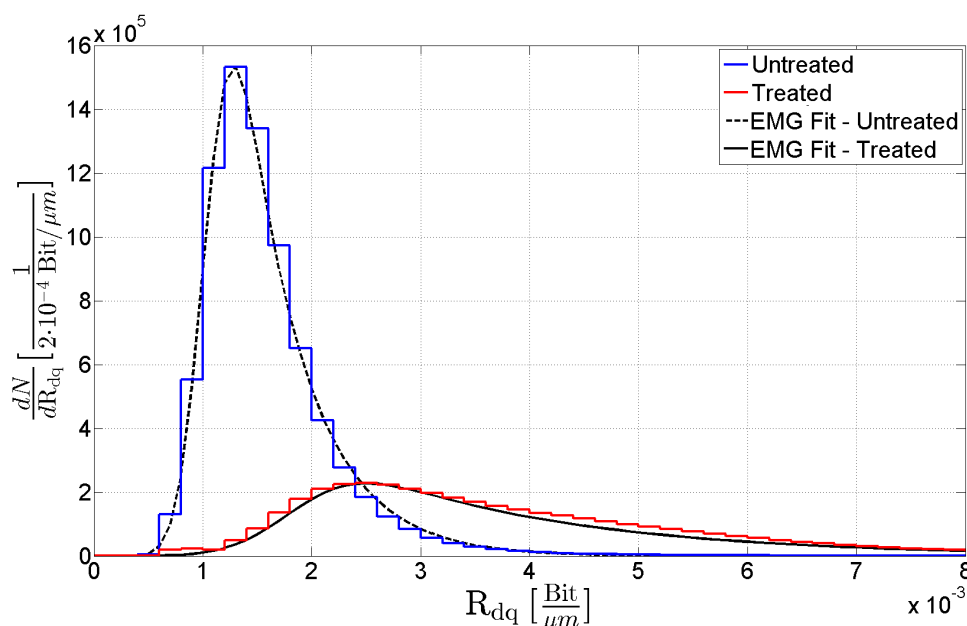
Figure 8.12: The x-axis shows the average boundary gradient R_{dq} measured with the algorithm and the y-axis shows the counts per bin.

bution before the surface treatment (blue) shows a Gaussian like profile with a small tail to higher values, the shape changes significantly due to surface chemistry. The average value of the treated surface (red) increases in comparison to the untreated surface. Additionally, the number of boundaries with large gradients increases.

The shape of the distribution can be modeled with an exponentially modified Gaussian distribution (EMG), which can be interpreted as a weighted shifted exponential distribution, where the weights are a function of the Gaussian distribution.

Mathematically, the EMG distribution is the convolution of a normal and exponential distribution, which results in

$$p(x) = \frac{\lambda}{2} e^{\frac{\lambda}{2}(2\mu + \lambda\sigma^2 - 2x)} \operatorname{erfc}\left(\frac{\mu + \lambda\sigma^2 - x}{\sqrt{2}\sigma}\right) \tag{8.2}$$

where erfc(x) as the complementary error function

$$\operatorname{erfc}(x) = 1 - \operatorname{erf}(x) = \frac{2}{\sqrt{\pi}} \int_x^\infty e^{-t^2}\, dt \tag{8.3}$$

103

and μ is the mean, σ the variance of the Gaussian component, and λ is rate of the exponential component. The average value of the EMG distribution is defined as

$$\bar{x} = \mu + \lambda^{-1} \tag{8.4}$$

Although no complete reasoning for the correctness of this distribution is achieved, there are some arguments to justify this choice. A decrease of the distribution for higher R_{dq} can be expected from surface topology [132] as well as little or no contributions at small values of R_{dq}. A symmetric distribution is not expected, since smaller values are more likely than higher values for the gradient. With these assumptions and the given measured distributions, the EMG meets these boundary conditions. The experimental data in figure 8.12 were fitted with the model given [270,271] and to get an estimate of the uncertainties, the bootstrap method [272] was applied and the error for the parameters was found to be in the order of $\mathcal{O}\left(10^{-6}\right)$ for each parameter.

The fitting parameters for the 18 treated and 18 untreated equators are given in table 8.4 and the average values are given in table 8.5.

$\left[\times 10^{-3} \frac{\text{Bit}}{\mu\text{m}}\right]$	WS			HAZ		
	μ	σ	λ^{-1}	μ	σ	λ^{-1}
Untreated	1.2 ± 0.1	0.2 ± 0.02	0.66 ± 0.03	1.1 ± 0.1	0.2 ± 0.01	0.3 ± 0.02
Treated	2.3 ± 0.1	1.0 ± 0.07	1.9 ± 0.04	1.9 ± 0.1	0.5 ± 0.02	1.8 ± 0.06

Table 8.4: The fit parameters μ is the mean, σ the variance of the Gaussian component and λ^{-1} the exponential decay rate of the EMG distribution in the welding seam region and the heat affected zone with the 95% confidence interval.

$\left[\times 10^{-3} \frac{\text{Bit}}{\mu\text{m}}\right]$	WS	HAZ
Untreated	1.8 ± 0.1	1.4 ± 0.1
Treated	4.2 ± 0.1	3.7 ± 0.1

Table 8.5: The average R_{dq} derived by the EMG fit with the 95% confidence interval.

The average value of R_{dq} described by the EMG distribution increases by 33% in the welding seam region and by 64% in the heat affected zone. Especially grain boundaries with large geometrical gradients, as described by λ^{-1}, evolve during surface treatment. This is due the effect, that grains in the niobium etch at slightly different rates due to differences in lattice orientation [75] and the grain boundaries starts evolving as steps on the surface. Those grain boundaries are more pronounced than the observed surface structures before the treatment and hence show a larger value for R_{dq}.

8.4 Summary

Two cavities were inspected, both before and after the surface treatment. For each of the 18 equators, the optical surface properties distributions were derived. Assumptions on the origin of all distributions were made, which lead to a set of models to quantify the observed distributions and figures of merit for these properties were obtained. The observed behaviour of the development of the variables were found to be in agreement with the physical processes occurring during the surface treatment.

A decrease of 49% of the total numbers of grain boundaries during the treatment was observed. The grain boundary area distribution describes the evolution of large boundaries and a reduction of small boundaries during the surface chemistry. The observed grain boundary density ρ decreases significantly during the treatment and differs for the welding seam and the heat affected zone by a factor of two. The boundary roughness, described as a local property of the grain boundary, increases by 33% due to the treatment. These observations are consistent with the appearance of the grain structure after the removal of a damaged layer of 150 μm. The welding seam specific grain boundary structure, namely the fishbone pattern, and the underlying recrystalized niobium grains show a prefered boundary orientation which were correctly identified.

Hence all the obtained variables enable a characterization of the inner cavity surface by means of an optical inspection. They allow for an automated distinction of treated and untreated cavities and the identification of the welding seam and heat affected zone.

CHAPTER 9

Vendor Specific Optical Surface Properties

Two different vendors produce cavities for XFEL: Ettore Zanon (E.Z.) [273] and Research Instruments (RI) [274]. Each vendor was certified to perform one of two surface chemistries, see [154] for details. In addition, electron beam welding (EBW) parameters like feed rate, weave bead, beam power and the sequence of equatorial welds are vendor specific. The analysis in this chapter will show that, with the formalism introduced in the last chapter, these vendor specific fabrication steps can be identified and quantified using OBACHT.

9.1   Optical dataset

At the time of the analysis, nine ILC-HiGrade cavities from RI were inspected, where each underwent as a finale surface treatment an EP treatment and seven ILC-HiGrade cavities from Ettore Zanon, which received a BCP Flash as final surface treatment. In addition, four cavities from the XFEL production from Ettore Zanon were inspected. This provides a dataset of nine EP cavities and eleven BCP Flash cavities.

9.2   Results

The aim of this chapter is to trace and quantify optical differences as a consequence of the different fabrication procedures. To achieve this, the experimental results for each variable from the image analysis will be shown and a detailed discussion of the results in context of vendor specific fabrication steps will follow.

107

9.2.1 Total Number of Boundaries

In table 9.1 the average total numbers of boundaries is given, as found by the algorithm. They are shown for two separate regions, the welding seam region and the heat affected zone.

	WS	HAZ
RI	35243 ± 1149	96921 ± 2031
E.Z.	44105 ± 981	121170 ± 1545
Difference	$25.14 \pm 5\,\%$	$25.02 \pm 3\%$

Table 9.1: Average number of boundaries found in the welding seam region and the heat affected zone per equator with 95% c.i..

As can be seen, the RI cavities show an average of $\sim$25% less grain boundaries than the Ettore Zanon cavities. This difference can be caused by two mechanisms: First by the different EBW parameters, since the welding melts the niobium, which has to recrystalize. The different parameters, like feed rate, beam current and wave bead, will create different spatial and temporal heat distributions and therefore different dynamics of grain growth. Hence, a different number of grain boundaries is not unexpected. Second, the chemical treatment will influence the visible grain boundaries. BCP enhances grain boundaries in comparison to EP, which increases the optical visibility of the boundaries, see figure 9.1. Hence, the total number of observed grain boundaries should differ for cavities treated
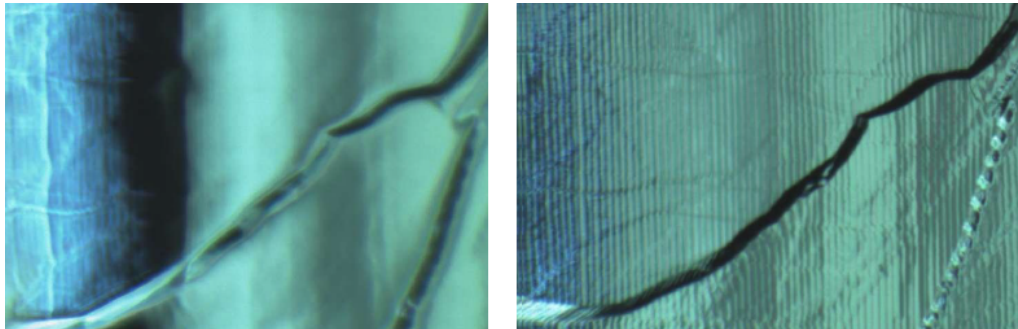
Figure 9.1: OBACHT image of the same boundary after EP (left) and BCP (right) [217,254]. The observable boundary area changed due to the treatment.

with EP in comparison to cavities treated with BCP.

9.2.2 Boundary Density

As discussed in section 8.3.2, the boundaries are equally distributed over the respective regions. Hence, the average difference of 25% between the vendors of the total numbers of boundaries should result in a difference of 25% in the mean density n_0 between the vendors. The density distributions for the two vendors and regions are shown in figures
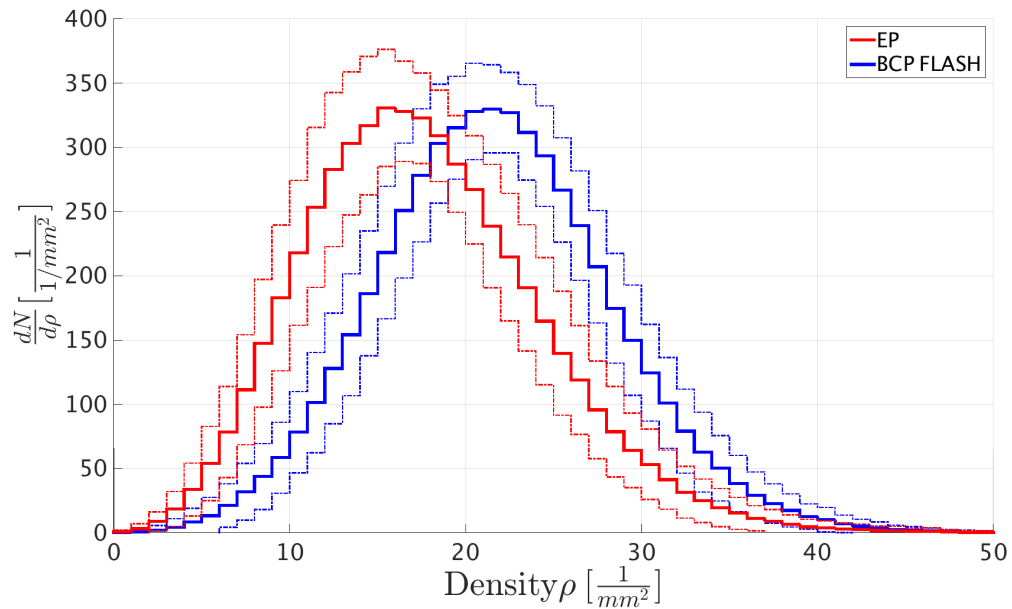
Figure 9.2: The x-axis shows the boundary density in the heat affected zone (HAZ), the y-axis the amounts of squares with a certain density. The plots show the average density distribution for all cells with a one σ interval.
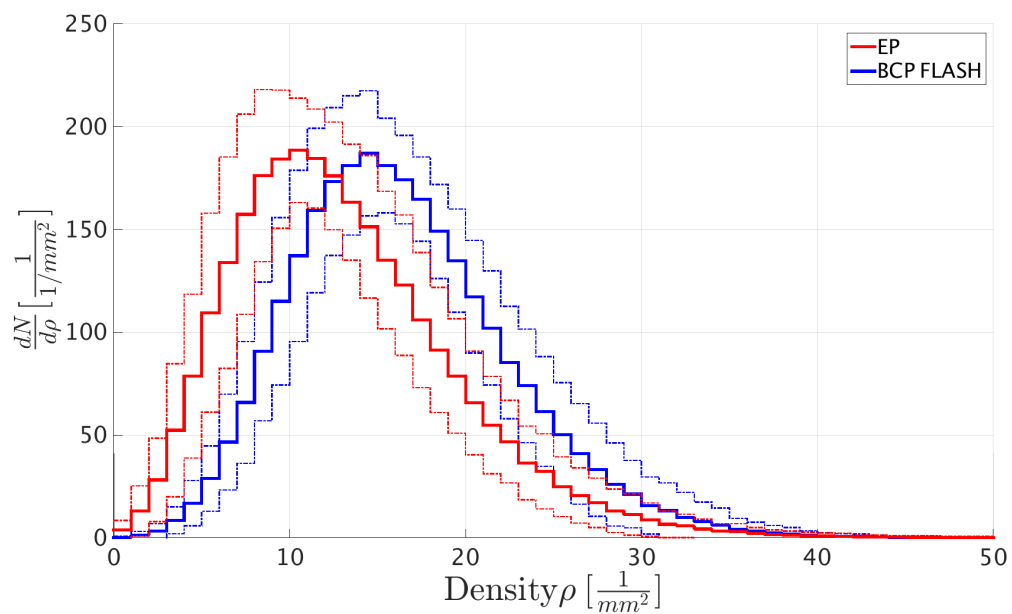
Figure 9.3: The x-axis shows the boundary density in the welding seam region, the y-axis the amounts of squares with a certain density. The plots show the average density distribution for all cells with a one σ interval.

9.2 and 9.3.

In table 9.2, the Gaussian fit parameters of the boundary densities are given. A difference in the order of $\sim 25\%$ between the average densities n_0 of the vendors is visible, while the general shape of the distributions are nearly identical.

$\left[\frac{1}{\text{mm}^2}\right]$	WS		HAZ	
	n_0	σ	n_0	σ
RI	12.6 ± 0.2	5.9 ± 0.1	17.1 ± 0.1	6.4 ± 0.1
E.Z.	15.8 ± 0.2	5.7 ± 0.1	21.1 ± 0.1	6.4 ± 0.1

Table 9.2: Result of the fit, with n_0 as the mean and σ as the variance of the Gaussian distribution, see equation 8.1, for the boundary densities in the welding seam region and the heat affected zone with 95% confidence intervals.

The boundary density behaves as expected from the total amounts. The Gaussian shape of the regional distributions reflects the fact, that the boundaries are equally distributed. And additionally, a clear distinction between the two vendors chemical treatments is observed.

9.2.3 Boundary Area

The boundary area distributions can be seen in figure 9.4.
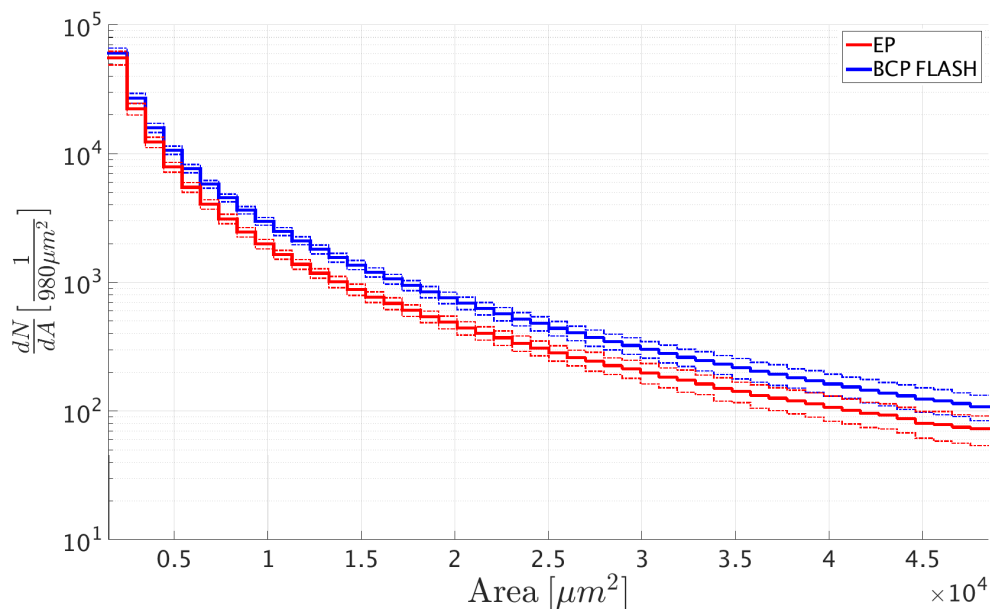
Figure 9.4: The x-axis shows the boundary area, while the y-axis shows the count per 980μm². The area distribution for each cell of RI (red) and Ettore Zanon (blue) are shown. The plots show the average area distribution for all cells with a one σ interval.

In general, EP cavities further decreases the number of boundaries with an area above

$5 \cdot 10^3$ μm^2 in comparison to BCP cavities. For a quantitative comparison, the scaling coefficients α[1] of the distributions are shown in table 9.3. The scaling coefficients differ

	α	α_{WS}	α_{HAZ}
RI	2.09 ± 0.01	2.09 ± 0.01	2.09 ± 0.01
E.Z.	1.97 ± 0.01	2.01 ± 0.01	1.95 ± 0.01

Table 9.3: Fit parameter α for the power law distribution in the whole image and for the welding seam region and the heat affected zone with 95% confidence interval.

for the vendors, where this effect is explained by the different surface treatments, see section 7.4.1.

9.2.4 Orientation of Welding Seam Boundaries

Another expected clear difference between the two vendors is the orientation angle of the welding seam boundaries, because it is influenced by the EBW parameters. Moreover, the orientation patterns along the equators should be different in their type since both vendors follow a different sequence of assembling and welding of the dumbbells. Figure 9.5 shows the orientation pattern in the welding seam region which is typical for each vendor.

As it can be seen, the boundaries in the welding seam region of Ettore Zanon have angles of $\pm 32^o$. The peaks at $\pm 90^o$ result from the welding seam ridge, where the ridge itself can vary in its position of up to 1 mm in a cell. The angles of the boundaries in the welding seam region of a RI cavity show a complete different distribution. Although they tend to have an average angle of $\pm 60^o$, a rather wide spread of the angles is observed.

The different angles observed are caused by the different weave bead and feed rate of the electron beam and in which position the cavity has been welded, which also differs for the vendors.

To understand the wide spread distribution of the boundaries within a RI cavity, the cavity orientation during welding has to be considered. The cavity is lying horizontally during welding at Ettore Zanon, while it is upright standing at RI [156]. Hence, the geometry of the bead is affected by the gravity acting on the recrystallization process [275]. The boundaries of the bead will be skewed due to this effect, and this generates this partially asymmetric and wide spread distribution of the boundary angles.

The second difference is that the assembly procedure of the dumbbells differs between the two vendors. The resulting welding sequence should lead to a specific series of welding patterns. In figure 9.6, the orientation patterns along the cavity axis are shown.

As can be seen, the orientation pattern of the grain boundaries for Ettore Zanon is equal in each cell. All cells from all cavities from Ettore Zanon show an A-type pattern. This is due to the assembly and welding sequence of Ettore Zanon, where all dumbbells are aligned in the EBW vacuum chamber and welded together in one run with no interruption.

---

[1]See section 8.3.3 for the definition.

111
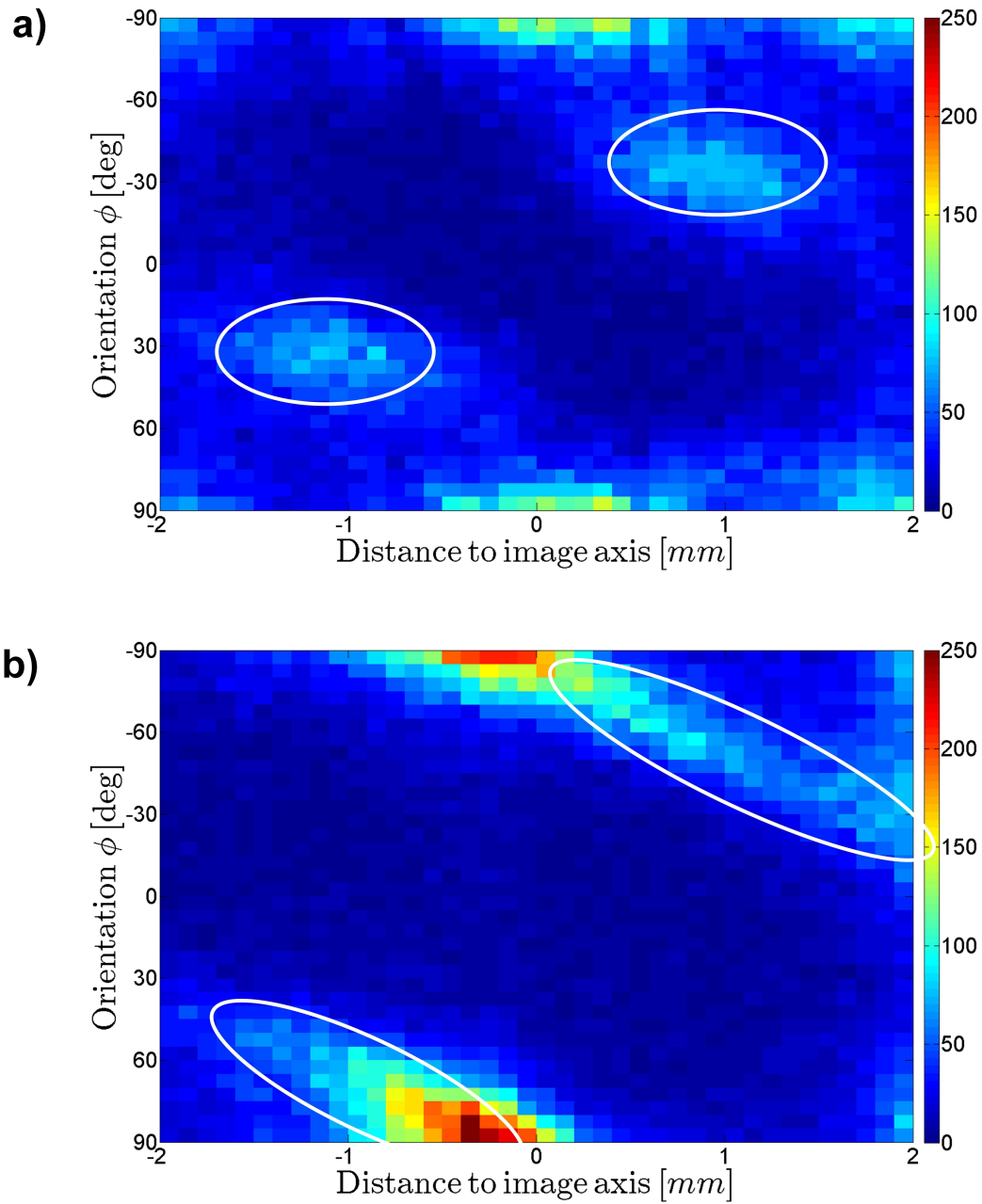
Figure 9.5: The x-axis shows the boundary centroid position with respect to the image axis. The y-axis shows the boundary orientation ϕ in degrees w.r.t. an axis perpendicular to the welding seam. Only the welding seam region is shown. The upper plot (a) represents boundaries in the welding seam region of a Ettore Zanon cavity, the lower plot (b) of a RI cavity. The white ellipses encircles the welding seam boundaries. The color depicts the counts per bin.
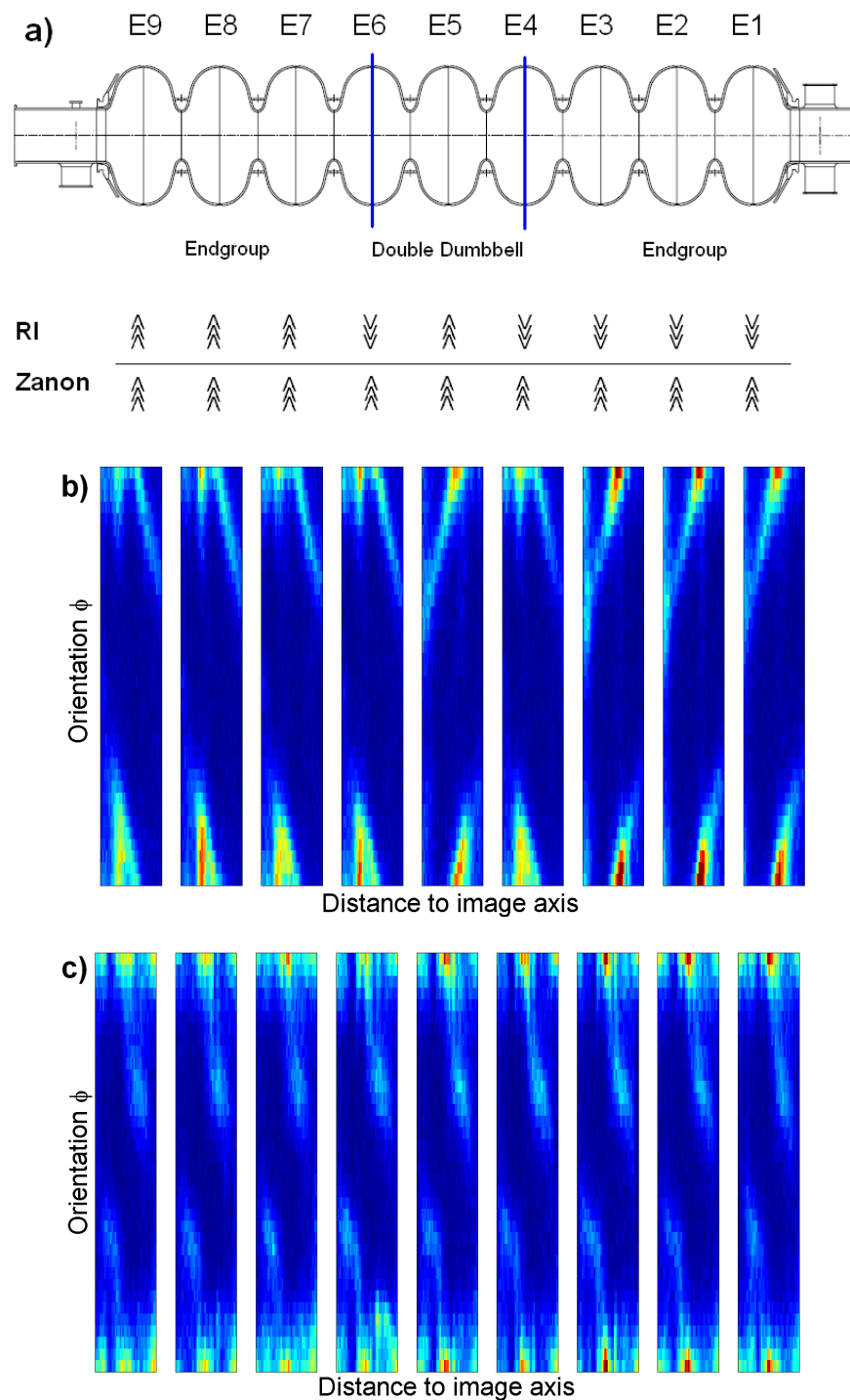
Figure 9.6: a) sketches the assembly procedure of a cavity at the two vendors and allows for the assignment of the patterns to the corresponding cells. Within the histograms, the color depicts the counts per bin. The x-axis shows the boundary centroid with respect to the image axis, only for the welding seam region. The y-axis shows the boundary orientation w.r.t. an axis perpendicular to the welding seam. b) is for RI and c) for Ettore Zanon.

113

In contrast, the sequence for RI is more complex. Equators one to three form the A-type orientation pattern. Equators seven to nine form the V-type orientation pattern. Equator four and six also form a V-type pattern and equator five has an A-type pattern. The assembly procedure at RI is as follows

- Assembly of the end cells first, welding equator one to three and equator seven to nine.

- Assembly and welding of the central double dumbbell, which is connected at what later is labeled equator five.

- Final connection of two end cell groups and the double dumbbell with a welding at equator four and six.

Between each step, the fabricated parts are brought out of the EBW vacuum chamber, and the end cell groups are rotated by 180° with respect to each other before the final welding. Hence, the orientation patterns found by the image processing algorithm along the cavity can be explained by the EBW parameters and the assembly procedure, which are vendor specific.

9.2.5 Boundary Roughness

The intensity gradient is used as a measure for the slope of a grain boundary, see section 7.3.4 for details. The resulting variable R_{dq} is used to quantify surface roughness by optical means. In the two plots in figure 9.7 and 9.8, the distributions for the vendors and the two regions are shown.

For a quantification, the fit parameters of the exponential modified Gaussian distribution (EMG) are given in table 9.4 and the average value of the distribution in table 9.5.   As

$\left[10^{-3}\frac{\text{Bit}}{\mu\text{m}}\right]$	WS			HAZ		
	μ	σ	λ^{-1}	μ	σ	λ^{-1}
RI	1.6 ± 0.1	0.7 ± 0.1	1.2 ± 0.1	2.0 ± 0.1	0.9 ± 0.2	1.1 ± 0.1
E.Z.	2.2 ± 0.1	0.8 ± 0.1	1.2 ± 0.1	2.3 ± 0.1	0.8 ± 0.2	1.3 ± 0.1

Table 9.4: The fit parameters μ is the mean, σ the variance of the Gaussian component and λ^{-1} the exponential decay rate of the EMG distribution, see equation 8.2, in the welding seam region and the heat affected zone with the 95% confidence interval.

seen in the plots and verified by the values of the EMG parameters, the cavities produced by RI show a smaller average roughness, a reduction of 17% in comparison to cavities produced by Ettore Zanon. The biggest difference of the average roughness, quantified by μ, is found in the welding seam region. The heat affected zone of BCP cavities have a slightly larger amount of steep grain boundaries, quantified by λ^{-1}.
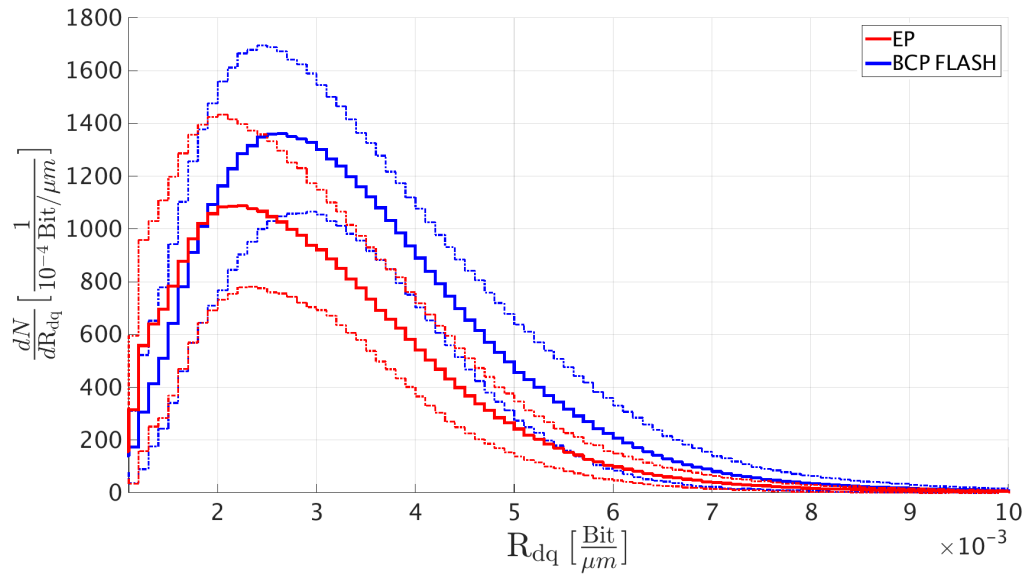
Figure 9.7: The x-axis shows the boundary gradient R_{dq} for boundaries within the welding seam region and the y-axis shows the counts per bin. The plots show the average R_{dq} distribution for all cells with a one σ interval. The red distribution is for RI and the blue distribution is for Ettore Zanon.
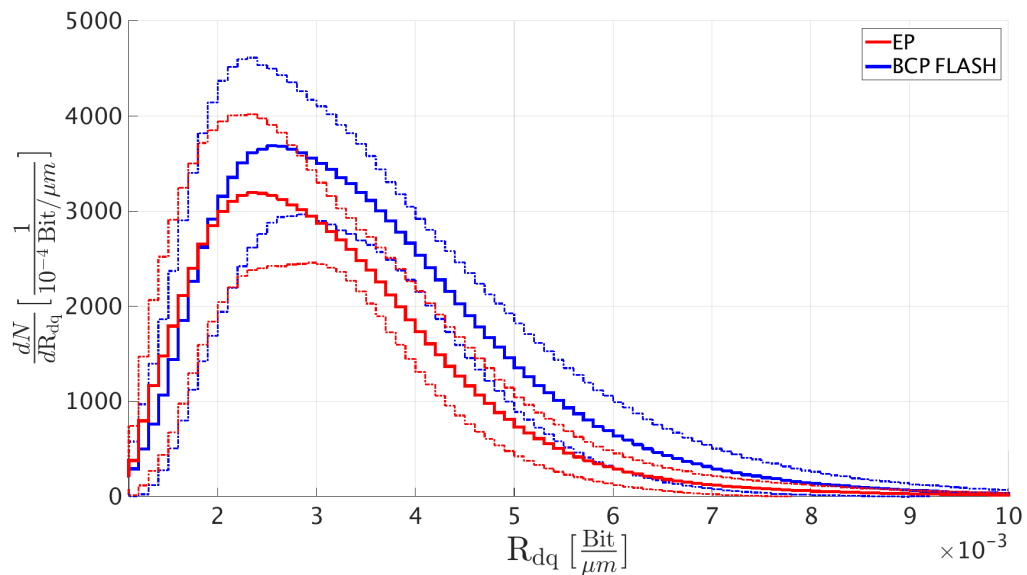
Figure 9.8: The x-axis shows the boundary gradient R_{dq} for boundaries within the heat affected zone and the y-axis shows the counts per bin. The plots show the average R_{dq} distribution for all cells with a one σ interval. The red distribution is for RI and the blue distribution is for Ettore Zanon.

$\left[10^{-3}\frac{\text{Bit}}{\mu\text{m}}\right]$	$\overline{R_{dq}}$	
	WS	**HAZ**
RI	2.8 ± 0.1	3.1 ± 0.1
E.Z.	3.4 ± 0.1	3.6 ± 0.1

Table 9.5: The average R_{dq} derived by the EMG fit with 95% confidence interval.

These results are in good agreement with the surface topology of EP and BCP treated cavities. It is known that EP leads to a smaller average roughness than BCP [75, 189], as well as smaller boundary step heights and slopes [176, 256], which is reflected in the average R_{dq}. In addition, a spatial inhomogeneous removal of material by EP has been observed [176], where the welding seam regions are more affected then the heat affected zone due to the spatial modulation of the applied electric field. This effect is visible in the mean of the Gaussian component, μ. The BCP treated cavities show a uniform roughness value while the values for EP treated cavities differ for the regions.

9.3   Summary

Two vendors produce cavities for XFEL. Each vendor is certified to perform a different chemical surface treatment procedure, namely EP and BCP Flash, as well as a different assembly and electron beam welding procedure. To quantify vendor specific optical surface properties as a consequence of these different procedures, nine cavities produced at RI and eleven cavities produced at Ettore Zanon were inspected and the results of the image analysis compared.

Differences in the total numbers of observed grain boundaries, the grain boundary density ρ and the distribution of the grain boundary area, parametrized by the scaling factor α, have been found and can be explained by the different surface treatment procedures. The boundary roughness values of EP cavities are on average 17% below the values for BCP cavities. This tendency was expected since it is known, that EP yields smoother surfaces. A vendor specific welding seam grain boundary angle due to different electron beam welding parameters was identified with the help of the optical surface properties deduced by the algorithm. In addition, the vendor specific sequence of welding patterns along the cavity reflect the different cavity assembly procedures.

In conclusion, the framework, developed in this thesis, allows an identification of the cavity vendor with a small set of variables obtained from OBACHT images. It can be used as a quality assurance tool in future fabrication series, since it enables an automatized quantification of the inner surface state, sensitive to fabrication specific differences.

CHAPTER 10

Correlation between RF limitations and Optical Surface Properties

The main motivation for the construction of an optical inspection for cavities was to gain a better understanding of their RF performance. Correlations between quenches or field emission during cold RF tests and localized defects seen in optical inspections are well known [119, 217, 219–222]. A systematic study on the correlation of general optical surface properties and RF performances has not been performed yet. Theoretical calculations in [122, 123] have shown that accelerating fields of 40-50 MV/m are achievable if surface structures and localized defects are below 10 µm. Thus with the given optical resolution, it is possible to resolve relevant surface structures for high-gradient cavities at OBACHT. The aim of this chapter is to study defect free cavities to identify underlying correlations between optical surface properties and RF limitations.

10.1 Dataset

In order not to be affected by local defects and to deduce an unbiased correlation between optical surface properties and the RF performance of a cavity, the cavities are selected by the following criteria:

1. No surface chemistry between optical inspection and the cold RF test

2. Optical inspection shows no local defect

3. Little or no field emission during the RF test.

The first criterion is needed to assure that the results of the two methods, optical inspection and cold RF test, can be correlated. A local defect, which is more likely to be the cause of a possible limitation of the cavity RF performance, has to be avoided in order to study the correlation between global surface properties and the $E_{acc,max}$. This is the reason for the second criterion. The last criterion prevents a falsification of the $E_{acc,max}$, because field emission is caused by a local defect at the iris region and introduces a new

117

loss mechanism. This additional loss mechanism affects the achievable accelerating field $E_{acc,max}$.

The different models for loss mechanisms yielding a low RF performance introduced in section 3.3.5 are used to guide the decision, which optical surface variables should be considered. How those variables are determined is described in section 10.1.2.

10.1.1 Cold RF Tests

The RF parameter used for this study is the maximal accelerating field $E_{acc,max}$. The decision to use this parameter has a simple methodological advantage - the maximal accelerating field of a cavity, measured in π-mode, is determined by the worst cell. This single cell limits the performance of the complete cavity.

A total number of 17 cavities from the XFEL production fulfill the before mentioned criteria, nine RI and eight Ettore Zanon cavities. To increase the dataset, but also to improve the universality of this study, three large grain cavities were included, namely AC151, AC153 and AC154. They fulfill the boundary conditions and increase the dataset to a total number of 20 cavities. Figure 10.1 shows the RF test results in an R_s versus $E_{acc,max}$ diagram. The datasets are taken from the XFEL cavity database [276]. All 20 cavities
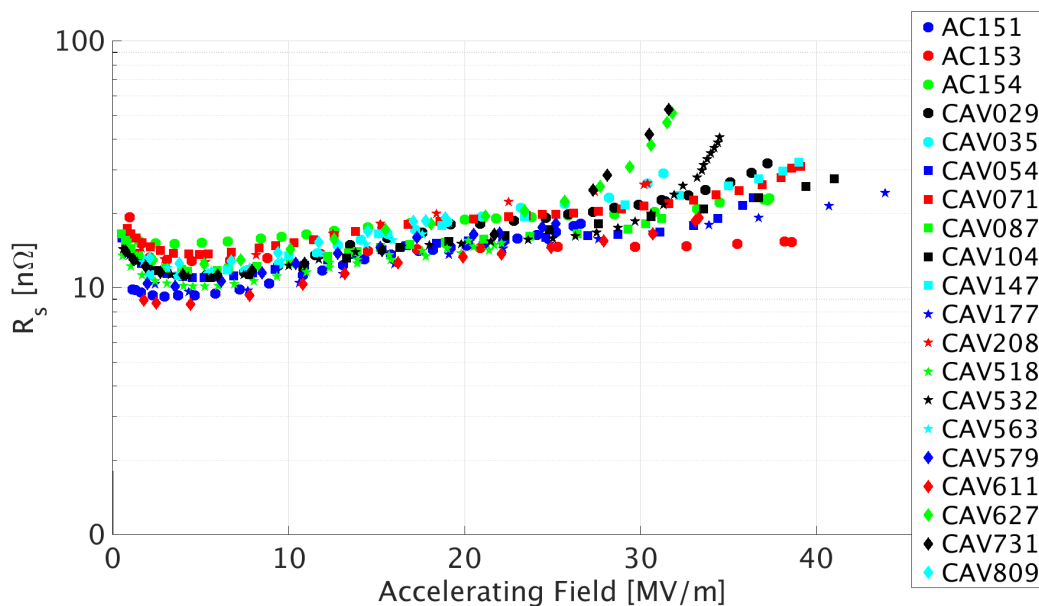
Figure 10.1: R_s versus $E_{acc,max}$ diagram of the used dataset. The applied accelerating field is shown on the x-axis, the y-axis shows the corresponding surface resistance measured in a cold RF test.

in the diagram show a similar behaviour. Although a slight variation in the minimal resistance occurs, the slope is quite similar. Eleven cavities out of the mentioned HiGrade cavities were produced with niobium from a single niobium supplier. Those eleven cavities form an additional subgroup, besides the RI and Ettore Zanon cavities, to disentangle a possible material influence.

10.1.2 Optical Surface Properties

The purpose if this investigation is to identify the RF limiting cell. The general assumption for this study is, that the maximal accelerating field $E_{acc,max}$ shows a negative correlation to the optical determined variable and the optically worst cell should also be the RF limiting cell. Hence, the maximum value of the optical surface variable of the nine cells identifies the optically worst cell. This maximum value is used to represent the whole cavity.

The different loss models introduced in section 3.3.5 predict different correlations between the RF performance and the surface properties. Those models can be related to optical variables within this framework:

1. **Magnetic Field Enhancement Model**: The basic equation of the Magnetic Field Enhancement (MFE) model (c.f. equation 3.14) relates the losses per length of a single grain boundary to the inverse of its bending radius. Since R_{dq} is also proportional to the inverse of the bending radius of the boundary, and the total losses need to be summarized over all grain boundaries, a dependency of the maximal accelerating field $E_{acc,max}$ on $\sum (A \cdot R_{dq})$ will be explored.

2. **Flux Pinning at Grain Boundaries**: As soon as the accelerating field is above a certain onset field, the magnetic flux will penetrate the cavity and create an additional RF loss. The explicit shape of the boundary influences this onset field. Hence, a dependency on $\sum (A \cdot R_{dq})$ is expected, since R_{dq} is a measure for the boundary shape and the losses need to be summed over all grain boundaries.

3. **Diffusion at Grain Boundaries**: Interstitials show a preferred diffusion at grain boundaries. The total sum of the grain boundary area $\sum A$ as optical surface variable is expected to serve as a correlator within this model.

4. **Grain Boundaries as Weak Links**: The weak link model assumes, that each grain boundary behaves as a Josephson contact, which leads to a loss term proportional to the grain boundary area, see equation 3.19. For that reason, the sum of the grain boundary area $\sum A$ may serve as a correlator.

The variables which will be discussed are the total grain boundary area $\sum A$ and the total grain boundary area times boundary roughness $\sum (A \cdot R_{dq})$. With these optical variables, the loss mechanism model with the best predictive power for the experimental data will be explored.

10.2 Results

As a first step, the optically worst cell will be identified for each cavity and the longitudinal distribution of the optically worst cells over the complete cavity is discussed in section 10.2.1. As a second step, to further investigate the assumption on the negative correlation between $E_{acc,max}$ and the optical surface properties, a comparison between second sound

results and the optical surface properties are performed in section 10.2.2. For each cavity, the data doublet of the maximal accelerating field and the maximal value of the optical surface property is used for the correlations in section 10.2.3.

10.2.1 Optical Assessment of Cells

In order to identify the optically worst cell, the distribution of the optical surface property within each cavity for every of the 20 cavities will be investigated. The variable with the most explanatory power should be the total grain boundary area $\sum A$ as discussed in section 10.1.2.

Identification of the Optically Worst Cell
The main term for the correlations is the total grain boundary area $\sum A$. Figure 10.2 shows the obtained values for each equator of each cavity. The observed values have a
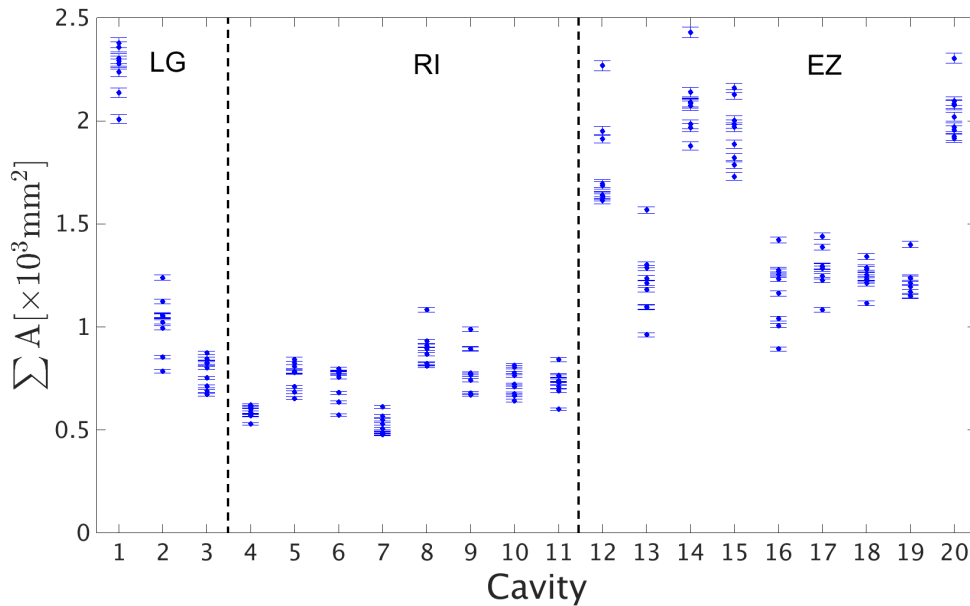
Figure 10.2: The total grain boundary area for each cavity in the dataset. LG stands for the three large grain cavities in the dataset. For each cavity, the values for all nine cells are shown.

vendor dependent mean and spread, shown in table 10.1, while the total range lies between 0.5 to $2.5 \times 10^3 \mathrm{mm}^2$. The difference between the vendor dependent mean is expected due to the vendor specific scaling factor α, discussed in section 9.2.3. The optically inspected area for an equator A_{tot} is simply the circumference of a cell at the equatorial welding times the width of an image. With the width of an image of 12 mm and the inner radius of an equator, which is 103.3 mm [67], A_{tot} can be obtained:

$$A_{tot} = 12\mathrm{mm} \cdot 2\pi \cdot 103.3\mathrm{mm} = 7.7 \times 10^3 \mathrm{mm}^2$$

120

$[\times 10^3 \mathrm{mm}^2]$	$\overline{\sum A}$	$\sigma_{\sum A}$
RI	0.7	0.06
E.Z.	1.5	0.14

Table 10.1: Vendor dependent total grain boundary area. The values are calculated over all cells from one vendor.

Hence, between 6 to 32 % of the inspected area is covered by grain boundaries. A plausibility check of the values for the total grain boundary area can be performed by obtaining an estimate of the grain size from this data. The first step is to divide the average total grain boundary area by the total number of grain boundaries (see section 9.2.1 for explicit numbers). This yields an average grain boundary area. For RI, this value is on the order of 5400 μm^2 and for Ettore Zanon 9200 μm^2. Experience with OBACHT pictures suggests an optical grain boundary thickness of 10 μm. With this value an average grain size can be calculated. This grain size, given in diameter, is 150 μm for RI and 300 μm for Ettore Zanon. Those values are in agreement with observed grain sizes in the heat affected zone and the welding seam after fabrication, see table 4.3 on page 39. In conclusion, the observed total grain boundary area per equator is within reasonable limits.

Dependence on Cell Position

A priori, the vendors should produce cavities with uniform properties. Hence, the null hypothesis H_0 is that an uniform longitudinal distribution of limiting cells should be observed. The expectation value is $E_{o,c} = N_{measurements}/N_{cells} = 20/9 = 2.\overline{2}$ per cell and the significance level for the χ^2-test is set to $p = 0.05$, the degrees of freedom (dof) equals eight. Figure 10.3 shows the longitudinal distributions of the frequency of the found limiting cell. With the given experimental distributions, the observed χ^2_{obs} is 18.8. With given dof of eight and the p-value of 0.05, the null hypothesis H_0 is rejected since $\chi^2_{obs} \gg \chi^2_{theo}$. In more than 13 of 20 of the measurements, the last three cells, cell seven to nine, were found to contain the limiting equator. A similar observation was found in [201], where the observed longitudinal quench distribution showed a deviation from the expectation in the endcells.

To calculate the probability of the occurrence of a cell as optically worst cell the Binomial cumulative distribution function is used. Assuming a constant probability $p = 1/9$ that a cell is the limiting cell, n the number of cavities tested and k the experimental occurrence found for each cell, the probability of the measured test outcome can be calculated with

$$F(k,n,p) = P(X \leq k) = \sum_{i=0}^{k} \binom{n}{i} p^i (1-p)^{n-i}. \tag{10.1}$$

Hence, the probability that the end cells seven to nine are the limiting cells in 65% of the measurements is $3.7 \cdot 10^{-3}$. The probability, that none of the cells four to six were found to be the optically worst cell in any test is below $3 \cdot 10^{-4}$. Both probabilities show that

121
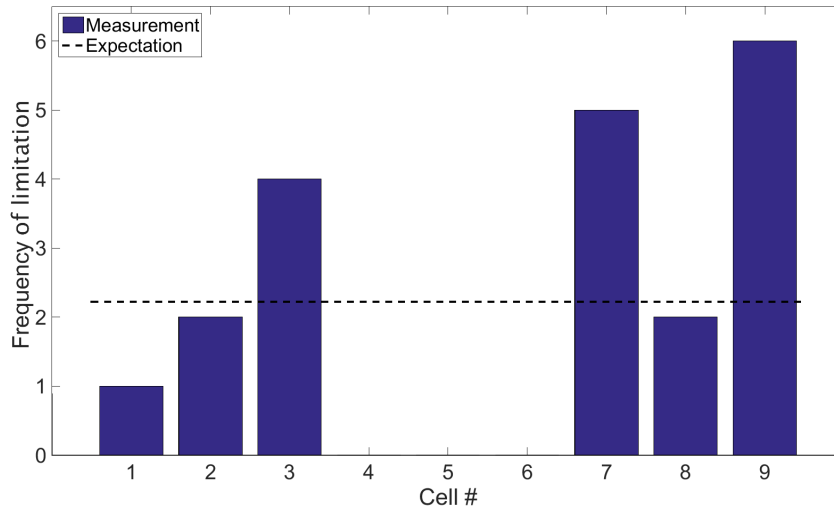
Figure 10.3: The longitudinal distribution of the maximum value of $\sum A$. The bars depict the measured frequency, the dashed line shows the expected frequency $p_{0,c}$.

these observations are noticeable, where a possible origin will be discussed later.

The experimental distribution separated for both vendors is shown in figure 10.4. A χ^2-test of the uniformity of a vendor dependent distribution is not possible because of the small sample size. With the given values and the observed occurrence, the probability for RI, that equator seven to be found as the optically worst cell in four of nine inspections is $1.2 \cdot 10^{-2}$. For Ettore Zanon, the probability for equator nine is $7.4 \cdot 10^{-3}$. The probability, that none of the cells four to six were found to be the optically worst cell in any test is $2.6 \cdot 10^{-2}$ for RI and $3.9 \cdot 10^{-2}$ for Ettore Zanon.

Discussion

The observed non-uniform distributions indicate, that the origin of the limitations lies within the fabrication procedure of cavities. Usually, surface contaminations during assembly or mounting of HOM-antennas and input couplers are discussed as a reason for the frequent limitations in the outer cells. But a local surface contamination would not influence the optical surface properties of a whole cell nor would it explain the vendor specific limiting cell as found with this method. As explained in chapter 9, both vendors pursue a different cavity assembly and electron beam welding procedure. Although details of these procedures, which could help to identify the very reason for this observation, are not public, it is clear that the cause for the vendor specific highly non-uniform distribution of gradient limiting cells - as defined by optical surface properties in defect free cavities - has to be found somewhere within these procedures.
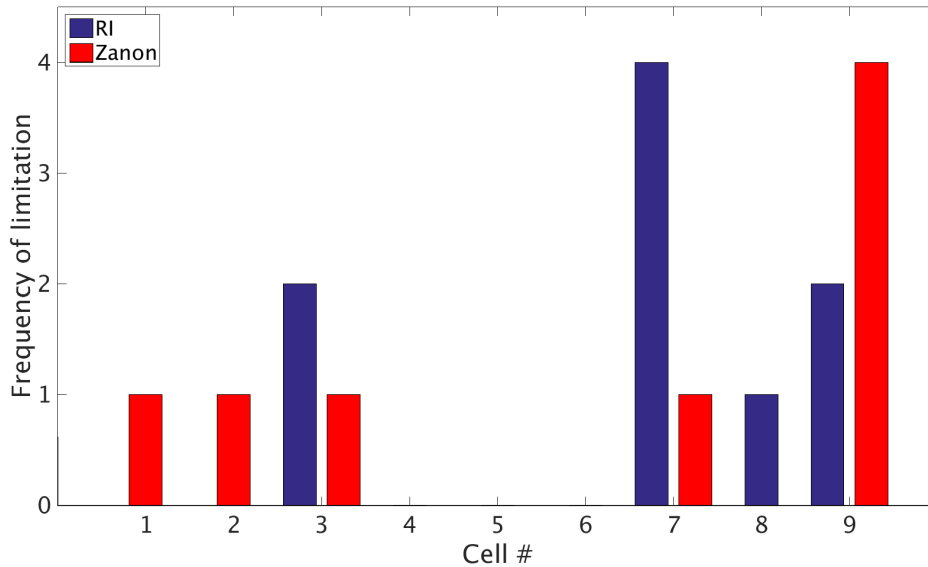
Figure 10.4: The longitudinal distribution of the maximum value of $\sum A$ displayed for both vendors. The bars depict the measured occurrence.

10.2.2 Correlation between Second Sound and Optical Surface Properties

Only two of the cavities in the used dataset, CAV00518 and CAV00087, have been tested with the second sound set up. The quench spot is obtained with a ray tracing method, described in [213]. The spot which minimizes the root-mean-square error (RMSE) between the theoretical and the experimentally second sound velocity is the most likely origin of the second sound wave and therefore the quench spot. The corresponding RMSE-maps for the two cavities are shown in figure 10.5.

For both, CAV0087 and CAV00518, the quench spot obtained by second sound has been found to be in cell nine. A visual inspection of the cavity surfaces with the second sound results did not reveal a local defect which could be identified as the cause for the quench. The same equators were identified as optically worst cells by the image processing and analysis algorithm developed in this thesis. The agreement between the second sound test and the optically worst cell in two of two tests supports the assumption on the negative correlation between optical deduced surface properties and the RF limitation of a cavity.

Since the visual inspection did not lead to an obvious quench spot, an attempt to correlate the angular quench origin with the angular distribution of the total grain boundary was done. The total grain boundary of an image against the image angle is shown in figure 10.6.
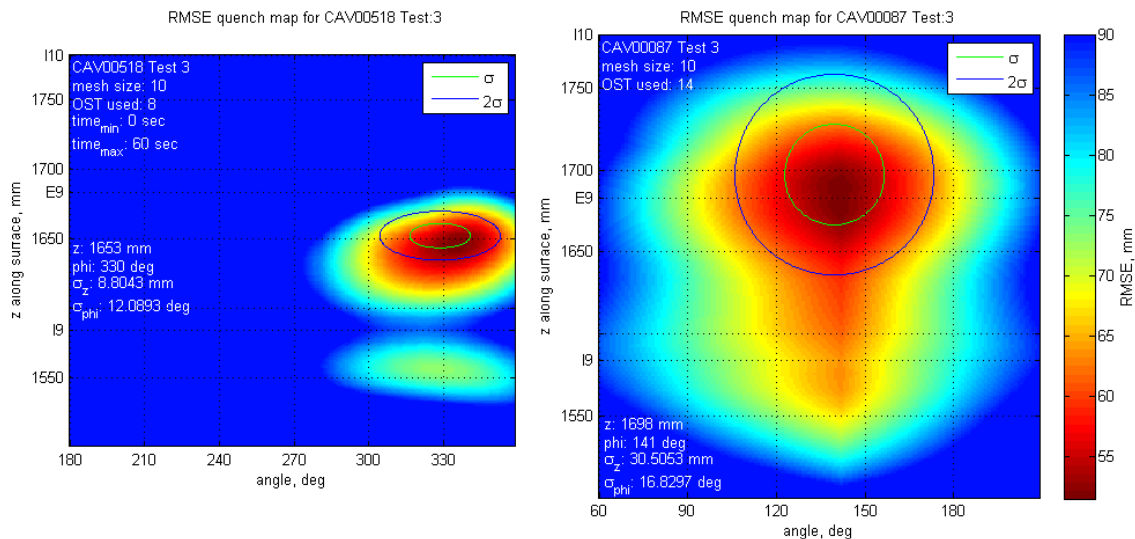
Figure 10.5: RMSE-Map of CAV518 (left) and CAV087 (right). The x-axis is the cell angle, the y-axis the longitudinal position along the cavity. The z-axis shows the color coded RMSE value. The most likely quench spot for CAV518 is about 44 mm below equator nine at (330 ± 12) degrees and for CAV087 at equator nine at (141 ± 16) degrees [213].
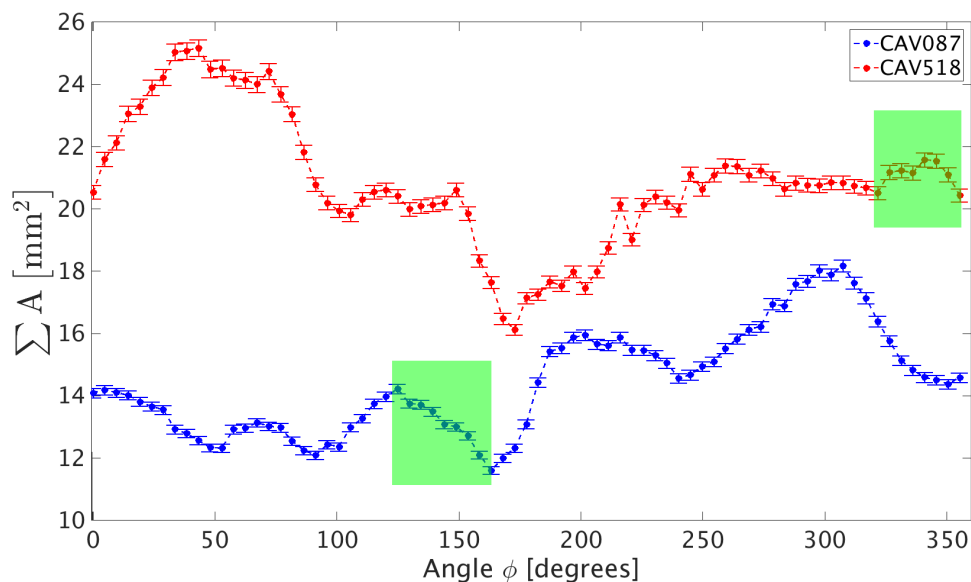
Figure 10.6: The total grain boundary area per image versus the image angle. The upper plot shows the distribution for CAV00518, the lower plot for CAV00087. The green boxes depict the most likely quench positions as obtained by second sound.

The magnitude of the fluctuations can be estimated by the observed boundary density discussed in section 9.2.2. Relative fluctuations of 30% around the average value can be expected. Hence, the fluctuations observed in the plot are within reasonable limits and do not indicate surface irregularities. No clear correlation between the angular total grain boundary distribution and the second sound test was found, although both quench spots are close to a local maximum.

10.2.3 Correlation between Accelerating Field and Optical Surface Properties

For a quantitative statement on the goodness of the relation between the optical surface property and $E_{acc,max}$, the Pearson correlation coefficient ρ is used [277]. Since both, the optical surface property and $E_{acc,max}$ are subject to measurement uncertainties, the calculation of the correlation coefficient should include these uncertainties. With appropriate estimators, the corrected Pearson correlation coefficient can be deduced [278, 279] which tests the influence of the uncertainty on the correlation coefficient. The 95% confidence interval of the correlation coefficient is calculated with a bootstrapping method [272, 280].

Total Grain Boundary Area $\sum A$

The first variable under investigation is the total grain boundary area $\sum A$ found in the equator images. Figure 10.7 shows the measured accelerating field as a function of the total boundary area.
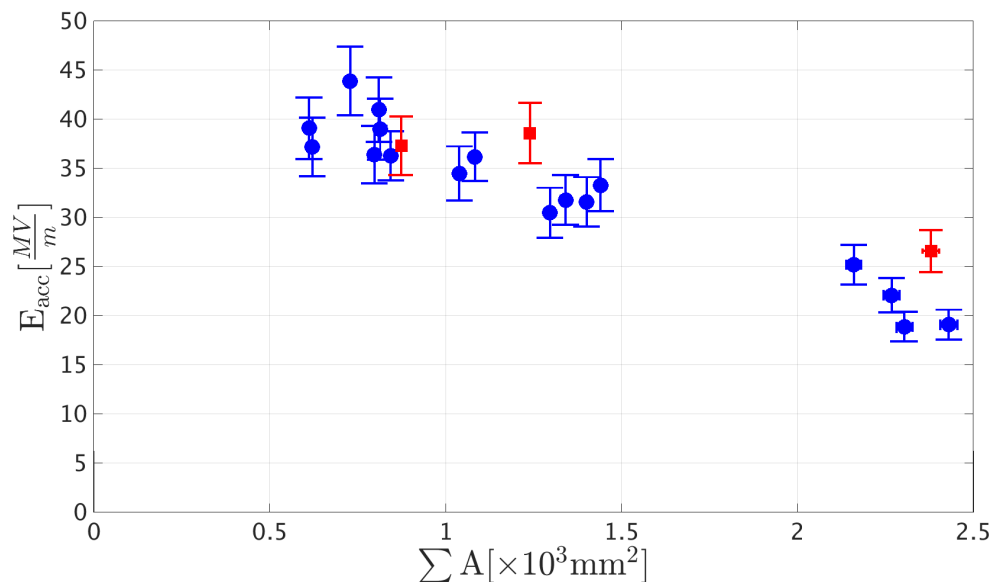
Figure 10.7: On the x-axis, the boundary area sum, which stands for a complete cavity, is shown, while the y-axis depicts the maximum accelerating field achieved by the respective cavity. The red squares display large grain cavities, the blue circles fine grain cavities.

The correlation coefficients are given in table 10.2. A very strong negative correlation of

	All	RI	E.Z.	Sheets
Pearson ρ	-0.93	-0.91	-0.96	-0.97
Corrected ρ	-0.93	-0.90	-0.96	-0.97
95% c.i.	[-0.96,-0.84]	[-0.99,-0.5]	[-0.99,-0.54]	[-0.99,-0.82]
Significance σ	6	3.4	4	5.2

Table 10.2: Pearson correlation coefficients for the variable $\sum A$ and $E_{acc,max}$ for different subgroups.

$\rho = $ -0.93 between the two variables $\sum A$ and $E_{acc,max}$ was found. The result is consistent for all the different subgroups, which were tested to reveal systematic origins of a possible correlation. Those subgroups are the nine RI cavities, the eight Ettore Zanon cavities and the eleven cavities from both vendors but from the same niobium supplier (Sheets). The large grain cavities are only included in the complete sample. The statistical significance of the correlation was found to be 6σ. In order to exclude possible contributions from local surface irregularities, the angular total grain boundary area distribution of the five worst cavities is shown imagewise in figure 10.8. The observed fluctuations are within
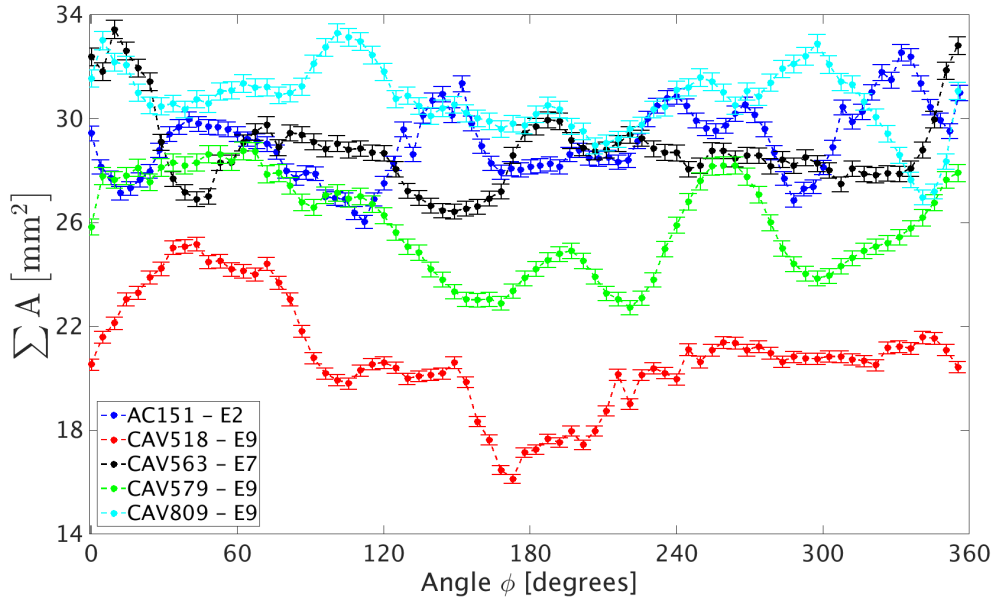
Figure 10.8: The total grain boundary area per image versus the image angle. The angular distribution of the optically worst equators of the five low performing cavities.

reasonable limits, based on the boundary density fluctuations ρ. On account of this, the possibility for local surface irregularities as a cause for the low maximal accelerating field can be neglected. In addition, CAV00518 has been tested with the second sound setup, where no specific local surface irregularity has been found. Summing up, the observed

negative correlation of ρ = -0.93 between $\sum A$ and $E_{acc,max}$ is based on global optical surface properties. Total grain boundary areas above 2000 mm^2 per equator indicates a lower achievable maximal accelerating field below 27 MV/m for this dataset.

Sum of Product of Boundary Area and Boundary Roughness $\sum (A \cdot R_{dq})$
Including the boundary roughness as a weight in the total grain boundary area could improve the relationship, as discussed within the different loss models. Figure 10.9 shows the measurement. The corresponding correlation coefficients are given in table 10.3.
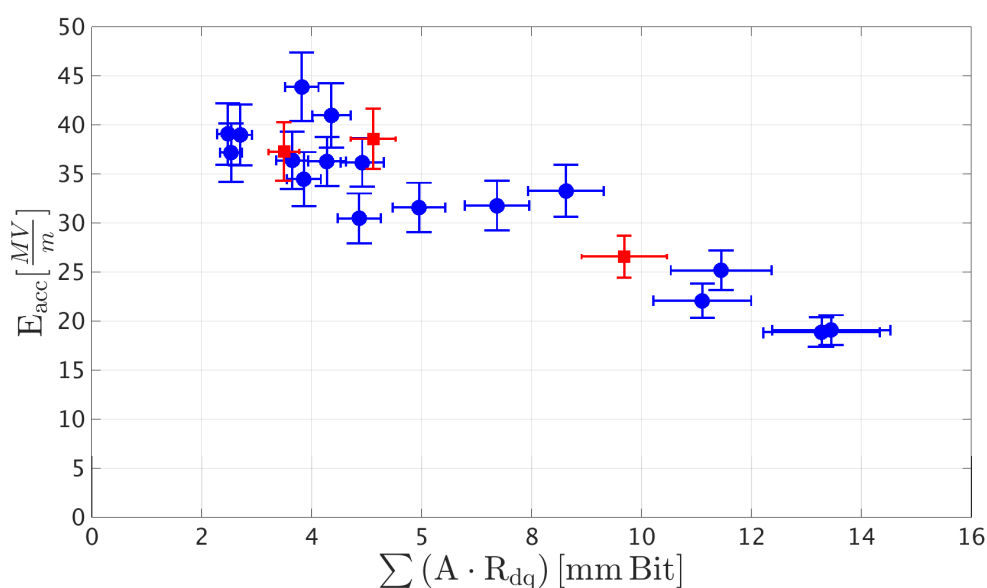
Figure 10.9: On the x-axis, the boundary area sum times the boundary roughness, which stands for a complete cavity, is shown, while the y-axis depicts the maximum accelerating field achieved by the respective cavity. The red squares display large grain cavities, the blue circles fine grain cavities.

	All	RI	E.Z.	Sheets
Pearson ρ	-0.91	-0.86	-0.92	-0.96
Corrected ρ	-0.90	-0.85	-0.91	-0.95
95% c.i.	[-0.96,-0.78]	[-0.99,-0.21]	[-0.97,-0.53]	[-0.98,-0.71]
Significance σ	5.7	3	3.3	4.9

Table 10.3: Pearson correlation coefficients for the variables $\sum (A \cdot R_{dq})$ and $E_{acc,max}$ for different subgroups.

Again, a very strong negative correlation of ρ = -0.91 between between $\sum A$ and $E_{acc,max}$ was found. The result is consistent within the different subgroups. The statistical significance of the correlation was found to be 5.7σ. A total boundary area times boundary

roughness above 10 mm Bit indicates a lower achievable maximal accelerating field below 27 MV/m for this dataset.

Range of Validity

The correlations shown in the figures 10.7 and 10.9 seem to have different validity ranges, although the coefficient of determination shows that both variables represent the data well over the whole range. To quantify this observation, the χ^2 as a measure of the goodness of fit is discussed. The degrees of freedom (dof) are four and 14 below and above 27 MV/m. The obtained values of the linear regression below and above 27 MV/m will be compared. This threshold value was chosen, since it is the upper accelerating field value of the five worst cavities. The results are given in table 10.4. A $\chi^2_{\text{red}} = \chi^2/\text{dof} \gg 1$ indicates a poor

	χ^2/dof for $\sum A$	χ^2/dof for $\sum (A \cdot R_{\text{dq}})$
$\leq$ **27 MV/m**	3.39	0.78
$>$ **27 MV/m**	0.74	1.25

Table 10.4: Reduced χ^2_{red} for the linear regression.

model fit. A $\chi^2_{\text{red}} > 1$ indicates that the fit has not fully captured the data. The CDF value for $\sum A$ above 27 MV/m is 0.26 and below 0.99. For $\sum (A \cdot R_{\text{dq}})$ below 27 MV/m it is 0.46 and above 0.77. In conclusion, the data suggests that the better correlator for the five worst cavities is the total grain boundary area times boundary roughness $\sum (A \cdot R_{\text{dq}})$. Above 27 MV/m, the total grain boundary area $\sum A$ is the best correlator for this dataset.

Discussion

Both variables examinedexamined, the total grain boundary area $\sum A$ and the total grain boundary area times boundary roughness $\sum (A \cdot R_{\text{dq}})$, correlate with the observed maximal accelerating field achieved in the cold RF test. Nevertheless, the variables seem to have a limited range of validity in which the corresponding loss mechanism is dominant. A possible explanation for this validity range is a saturation of the effect based on the boundary roughness and has already been observed [281]. The saturation can be explained with the magnetic field enhancement model by Knobloch et.al. [132] and OBACHT is sensitive to resolve the relevant slope angles, see section 7.4.2. The penetration of the magnetic field at grain boundaries at low accelerating fields due to geometrical enhancement would increase the losses and limit the cavity performance. The magnetic field enhancement factor is $\beta_m = \left(\frac{r}{R}\right)^{-1/3}$ with r the bending radius of the boundary. A smoother boundary implies a larger r and hence a smaller field enhancement, but for large r, the improvement of the field enhancement slows down due to the scaling factor n = -1/3. On account of this, the maximum achievable accelerating field becomes less dependent on the boundary roughness. Therefore, smoothing boundaries beyond the currently with EP achievable level does not improve the cavity performance since this effect becomes less important. Nevertheless, cavities with a large boundary roughness, as were for the five

cavities in the dataset, are possibly limited by this effect.

The observed dependency on the total grain boundary area can be explained by two models, namely the grain boundaries as weak links and the diffusion model. As it was found in [282] for large grain cavities in high accelerating fields, no preferential heating at grain boundaries was observed. This would contradict the weak link model, since a preferred heating at the boundaries should be observed assuming this model. In addition, a slightly stronger correlation was found here, if only cavities build with niobium from the same supplier are considered: $\rho = -0.93$ for the whole dataset and $\rho = -0.97$ for cavities from the same niobium supplier. This is in agreement with the diffusion model, due the similar chemical composition of interstitials from one supplier. Furthermore, recent studies showed that artificial changes of the chemical composition in the surface layer significantly improve the cavity performance [149].

Dzyuba et.al. [138] developed and tested a loss model based on the theoretical work in [137, 283], where both, surface roughness and contamination, equally contribute to the losses observed in a cavity and each should exacerbate the negative effect of the other. However, the physical effect behind the surface roughness loss mechanism in this paper was flux pinning and not magnetic field enhancement and the authors of the study argued that the magnetic field enhancement model should be included in their work to further analyze it. Still, the model developed in Dzyuba et.al. [138] additionally supports the experimental results of this thesis.

Summing up, the two optical surface properties, namely the grain boundary area A and roughness R_{dq}, are well suited to describe the maximal accelerating field achieved by a cavity. This observation can be interpreted by the combination of two models, namely the magnetic field enhancement and the diffusion model. The surface topography and the chemical composition of the near-surface layer are the corresponding surface properties of these two models, whereby both have to be controlled and improved to achieve high accelerating fields.

10.3 Summary

With the formalism developed in this thesis, it is possible to optically analyze a fully equipped and tested cavity and correlate the surface properties with its RF performance. A correlation between the optical surface properties and the maximal accelerating field $E_{acc,max}$ and a vendor specific distribution of accelerating field limiting cells was found.

The dataset consists of 20 inspected cavities. All of them had to fulfill boundary conditions to ensure that the RF performance solely relies on the global optical surface properties as seen during the OBACHT inspection. For a further investigation of a possible vendor- or niobium-specific influence, subgroups were established which allow a disentanglement of these possible influences.

By determining the optically worst cell for each cavity, a non-uniform distribution of those cells along the cavity was found. In addition, a vendor dependent distribution was observed and a vendor specific most likely limiting cell. This cell is cell seven for RI and cell nine for Ettore Zanon and the overall distribution can be probably explained by the assembly and electron beam welding procedures.

Two cavities, CAV00518 and CAV00087, have been tested with the second sound setup and the equators containing the quench spot and its angular position have been obtained. The same equators were identified as optically worst cell with the image processing and analysis algorithm. The angular position of the quench spot identified by second sound did not lead to a local defect on the cavity surface, which could have been the cause for the quench. Neither did the angular distribution of the optical surface properties lead to an explicit identification, although both quench spots are close to a local maxima.

Due to the already introduced loss models, the optical surface variable of choice were the total grain boundary area $\sum A$ and the total grain boundary area times the boundary roughness $\sum (A \cdot R_{dq})$. Both show a strong correlation with the maximal accelerating field $E_{acc,max}$: $\rho = -0.93$ with a significance of 6σ for the total grain boundary $\sum A$ and $\rho = -0.91$ with a significance of 5.7σ for the total grain boundary area times the boundary roughness $\sum (A \cdot R_{dq})$. Although both optical surface properties correlate with the maximal accelerating field, they seem to have a limited range of validity in which the corresponding loss mechanism is dominant. This is quantified by the χ^2/dof as a measure for the goodness of fit in the different co-domains.

This observation can be interpreted by two different loss mechanisms, where each contributes to the cavity performance. For cavities with a rough surface, the limitation is best described by the magnetic field enhancement model. As the surface gets smoother, this influence vanishes or saturates and the mere existence of grain boundaries become important. Together with observations from other studies, this behaviour is best described by the diffusion model, in which grain boundaries are not the problem themselves but allow interstitials to diffuse into the near-surface niobium which influences the cavity performance. Hence, both loss mechanisms, the surface roughness and the near-surface chemical composition, contribute equally to the limitation of the cavity performance.

Summing up, a vendor specific distribution of accelerating field limiting cells and a strong correlation between global optical surface properties and the maximal accelerating field in defect free cavities was found.

CHAPTER 11

Summary

In the scope of this thesis, a framework has been developed, which allows an automated analysis of images of the inner surface of superconducting radio frequency (SRF) cavities by means of an optical inspection robot (OBACHT). This framework includes an image processing and analysis algorithm which yields a set of optical surface properties quantifying the inner cavity surface. With the resolution of OBACHT and the image processing code it is possible to resolve and quantify surface structures down to > 10 µm. This resolution is at least needed to investigate surface structures which could lead to performance limiting processes of SRF cavities.

Checks on the plausibility and reliability of the introduced optical surface properties on test patterns as well as on cavities were performed. In particular, the topography development of the cavity surface due to a chemical surface treatment is a good test case for the image processing and analysis algorithm. All observations of the development of the optical surface properties are consistent with the appearance of the grain structure due to the surface chemistry and have lead to a quantitative description of the inner cavity surface.

A first application of the newly developed framework was an investigation of optical surface properties for different vendors. Significant differences in the quantitative characterization by means of the optical surface properties have been identified. Each difference turns out to be related to the vendor specific cavity assembly, electron beam welding and surface treatment procedures.

In order to study the interplay between the optical surface properties and RF limitations, the concept of an optically worst cell which is assumed to be the limiting cell of the RF performance was introduced. An eye-catching observation has been made. A non-uniform distribution of the optically worst cell was observed. In fact, the non-uniform distribution is vendor specific. This observation can only be explained by the vendor specific assembly procedure and equatorial welding sequence. A crosscheck with second sound tests of two cavities support the assumptions of the identity of the optically worst cell and the limiting cell of the RF performance.

In an unprecedented study, correlations of optical surface properties versus the maximal achievable accelerating field $E_{acc,max}$ of 20 cavities has been investigated. A strong negative correlation of the total grain boundary area and also of the total grain boundary area times the boundary roughness versus the maximal achievable accelerating field has been found. These observed correlations can be described by two loss mechanisms, namely the magnetic field enhancement model and the diffusion model.

A quantitative characterization and analysis of the cavity surface by means of optical methods has been achieved. The image processing and analysis algorithm developed in this thesis can be used for the quality assurance of a future ILC cavity production.

List of Figures

10.2 The total grain boundary area for each cavity in the dataset. LG stands for the three large grain cavities in the dataset. For each cavity, the values for all nine cells are shown. 120

10.3 The longitudinal distribution of the maximum value of $\sum A$. The bars depict the measured frequency, the dashed line shows the expected frequency $p_{0,c}$ 122

10.4 The longitudinal distribution of the maximum value of $\sum A$ displayed for both vendors. The bars depict the measured occurrence. 123

10.5 RMSE-Map of CAV518 (left) and CAV087 (right). The x-axis is the cell angle, the y-axis the longitudinal position along the cavity. The z-axis shows the color coded RMSE value. The most likely quench spot for CAV518 is about 44 mm below equator nine at (330 ± 12) degrees and for CAV087 at equator nine at (141 ± 16) degrees [213]. 124

10.6 The total grain boundary area per image versus the image angle. The upper plot shows the distribution for CAV00518, the lower plot for CAV00087. The green boxes depict the most likely quench positions as obtained by second sound. 124

10.7 On the x-axis, the boundary area sum, which stands for a complete cavity, is shown, while the y-axis depicts the maximum accelerating field achieved by the respective cavity. The red squares display large grain cavities, the blue circles fine grain cavities. 125

10.8 The total grain boundary area per image versus the image angle. The angular distribution of the optically worst equators of the five low performing cavities. 126

10.9 On the x-axis, the boundary area sum times the boundary roughness, which stands for a complete cavity, is shown, while the y-axis depicts the maximum accelerating field achieved by the respective cavity. The red squares display large grain cavities, the blue circles fine grain cavities. 127

List of Tables

References

[1] S. L. Glashow. Partial-symmetries of weak interactions. *Nuclear Physics*, 22(4):579–588, 1961. (Cited on page 9.)

[2] S. Chatrchyan, V. Khachatryan, A. Sirunyan, and A. Tumasyan. Observation of a new boson at a mass of 125 GeV with the CMS experiment at the LHC. *Physics Letters B*, 716(1):30–61, 2012. (Cited on pages 9 and 14.)

[3] G. Aad, T. Abajyan, B. Abbott, and J. Abdallah. Observation of a new particle in the search for the Standard Model Higgs boson with the ATLAS detector at the LHC. *Physics Letters B*, 716(1):1–29, 2012. (Cited on pages 9 and 14.)

[4] M. Duehrssen. Higgs Combination. In *Proceedings of 50th Rencontres de Moriond EW*, 2015. (Cited on pages 9 and 14.)

[5] P. W. Higgs. Broken Symmetries and the Masses of Gauge Bosons. *Physical Review Letters*, 13(16):508–509, 1964. (Cited on page 9.)

[6] F. Wilczek. Beyond the standard model: An Answer and twenty questions. *ArXiv preprint hep-ph/9802400*, 1998. (Cited on page 9.)

[7] R. D. Peccei and H. R. Quinn. CP conservation in the presence of pseudoparticles. *Physical Review Letters*, 38(25):1440, 1977. (Cited on page 9.)

[8] L. Canetti, M. Drewes, and M. Shaposhnikov. Matter and antimatter in the universe. *New Journal of Physics*, 14(9):95012, 2012. (Cited on page 9.)

[9] G. Goldhaber. The Acceleration of the Expansion of the Universe: A Brief Early History of the Supernova Cosmology Project (SCP). *American Institute of Physics Conference Series*, 1166(1), 2009. (Cited on page 9.)

[10] C. L. Bennett, D. Larson, J. L. Weiland, et al. Nine-year Wilkinson Microwave Anisotropy Probe (WMAP) observations: final maps and results. *The Astrophysical Journal Supplement Series*, 208(2):20, 2013. (Cited on page 9.)

[11] J. Brau, R. M. Godboleb, F. R. Le Diberderc, et al. The physics case for an e+e- linear collider. *ArXiv preprint arXiv:1210.0202*, 2012. (Cited on pages 9 and 14.)

References

[12] H. Baer, M. Berggren, J. List, et al. Physics case for the ILC project: perspective from Beyond the Standard Model. *ArXiv preprint arXiv:1307.5248*, 2013. (Cited on pages 9 and 14.)

[13] G. Weiglein, T. Barklow, E. Boos, et al. Physics interplay of the LHC and the ILC. *Physics Reports*, 426:47–358, 2006. (Cited on pages 9 and 14.)

[14] A. Arbey, M. Battaglia, and F. Mahmoudi. The Higgs boson, Supersymmetry and Dark Matter: Relations and Perspectives. *arXiv preprint arXiv:1504.05091*, 2015. (Cited on pages 9 and 14.)

[15] T. Behnke, J. Brau, B. Foster, et al. The International Linear Collider Technical Design Report-Volume 1: Executive Summary. *ArXiv preprint arXiv:1306.6327*, 2013. (Cited on pages 9 and 13.)

[16] J. Brau, Y. Okada, and N. Walker. International Linear Collider Reference Design Report, The International Linear Collider Technical Design Report. Technical report, ILC GDE, 2013. (Cited on pages 9, 13, 15, CXXXVII, and CXLVII.)

[17] G. Wolf. The Glorious days of physics: A Tribute to Bjorn H. Wiik and his physics. In *International School of Subnuclear Physics: 37th Course: Basics and Highlights of Fundamental Physics*, pages 20–69. Ettore Majorana Foundation and Centre for Scientific Culture, 2000. (Cited on page 11.)

[18] R. Brinkmann. Proposal for a TESLA Test Facility. Technical report, DESY, 1992. (Cited on page 11.)

[19] F. Richard, J. R. Schneider, D. Trines, and A. Wagner. TESLA Technical Design Report Part I: Executive Summary (2001). Technical report, DESY-01-011, hep-ph/0106314, 2001. (Cited on page 11.)

[20] M. Vogt, B. Faatz, J. Feldhaus, et al. The Free-Electron Laser FLASH at DESY. In *Proceedings of IPAC2013*, pages 10–12, 2013. (Cited on page 11.)

[21] E. Saldin, W. Sandner, Z. Sanok, et al. First observation of self-amplified spontaneous emission in a free-electron laser at 109 nm wavelength. *Physical Review Letters*, 85(18):3825–3829, 2000. (Cited on page 11.)

[22] V. Ayvazyan, N. Baboi, J. Schneider, et al. A new powerful source for coherent VUV radiation: Demonstration of exponential growth and saturation at the TTF free-electron laser. *The European Physical Journal D - Atomic, Molecular and Optical Physics*, 20(1):149–156, 2002. (Cited on page 11.)

[23] V. Ayvazyan, N. Baboi, I. Bohnet, et al. Generation of GW Radiation Pulses from a VUV Free-Electron Laser Operating in the Femtosecond Regime. *Physical Review Letters*, 88(10):104802, 2002. (Cited on page 11.)

[24] V. Ayvazyan, N. Baboi, J. Bähr, et al. First operation of a free-electron laser generating GW power radiation at 32 nm wavelength. *The European Physical Journal D*, 37(2):297–303, November 2005. (Cited on page 11.)

[25] W. Ackermann, G. Asova, V. Ayvazyan, et al. Operation of a free-electron laser from the extreme ultraviolet to the water window. *Nature photonics*, 1(6):336–342, June 2007. (Cited on page 11.)

[26] S. Schreiber. First Lasing in the Water Window with 4.1 nm at FLASH. In *Proceedings of FEL2011*, pages 164–165, 2010. (Cited on page 11.)

[27] DESY. *Photon Science - Annual Report 2010*. 2010. (Cited on page 11.)

[28] DESY. *Photon Science - Annual Report 2011*. DESY, 2011. (Cited on pages 11, 12, and CXLVII.)

[29] DESY. Photon Science - Annual Report 2014. Technical report, 2014. (Cited on page 11.)

[30] D. Kostin. New Accelerating Modules RF Test at TTF. In *Proceedings of LINAC2004*, number 1 in Proceedings, pages 672–674, 2004. (Cited on page 11.)

[31] D. Kostin, W. Moeller, A. Goessel, and R. Lange. Testing the FLASH Superconducting Accelerating Modules. In *Proceedings of SRF2007*, 2007. (Cited on page 11.)

[32] D. Kostin, W. Moeller, A. Goessel, and K. Jensch. Superconducting Accelerating Module Tests at DESY. In *Proceedings of SRF2009*, pages 180–184, 2009. (Cited on page 11.)

[33] K. Honkavaara, B. Faatz, J. Feldhaus, et al. FLASH Upgrade. In *Proceedings of IPAC2010*, pages 1290–1292, 2010. (Cited on pages 11, 12, and CXXXVII.)

[34] M. Altarelli, R. Brinkmann, M. Chergui, et al. The Technical Design Report of the European XFEL. 4:2006–2097, 2006. (Cited on pages 11, 13, 14, 35, 36, 38, 39, 40, CXXXVII, CXXXVIII, and CXLVII.)

[35] K. Honkavaara, S. Ackermann, V. Ayvazyan, et al. Status of the FLASH II project. In *Proceedings of FEL2012*, pages 1–4, 2012. (Cited on page 11.)

[36] S. Schreiber and B. Faatz. First Lasing at FLASH II. In *Proceedings of FEL2014*, pages 2014–2015, 2014. (Cited on page 11.)

[37] E. Vogel, C. Albrecht, N. Baboi, et al. Test and Commissioning of the Third Harmonic RF System for FLASH. In *Proceedings of IPAC2010*, pages 4281–4283, 2010. (Cited on pages 12 and CXXXVII.)

References

[38] G. Cancelo, B. Chase, M. Davidsaver, et al. Analysis of DESY-FLASH LLRF Measurements for the ILC Heavy Beam Loading Test. In *Proceedings of PAC2009*, pages 2189–2191, 2009. (Cited on page 12.)

[39] N. Walker, S. Schreiber, L. Froehlich, et al. Operation of the FLASH Linac with Long Bunch Trains and High Average Current. In *Proceedings of PAC2009*, pages 2766–2768, 2009. (Cited on page 12.)

[40] S. Pei, C. Adolphsen, and J. Carwardine. FLASH Beam-Off RF Measurements and Analyses. In *Proceedings of PAC2009*, 2009. (Cited on page 12.)

[41] S. Pei, C. Adolphsen, J. Carwardine, and N. Walker. Latest Results on Cavity Gradient and Input RF Stability at FLASH/TTF Facility. In *Proceedings of IPAC2010*, page 7, 2010. (Cited on page 12.)

[42] B. Horst, A. Matheisen, B. Petersen, et al. Experiences on Improved Cavity Preparation Cycles with a Vision on Industrialization of the XFEL Cavity Preparation. In *Proceedings of SRF2009*, pages 791–793, 2009. (Cited on pages 13 and 35.)

[43] D. Reschke. Challenges in SRF Module Production for the European XFEL. In *Proceedings of SRF2011*, pages 2–6, 2011. (Cited on page 13.)

[44] D. Reschke. Infrastructure, Methods and Test Results for the Testing of 800 Series Cavities for the European XFEL. In *Proceedings of SRF2013*, pages 806–809, 2013. (Cited on page 13.)

[45] D. Proch. Overview of industrialization strategies for ILC. *Proceedings of SRF2007*, pages 1961–1965, 2007. (Cited on page 13.)

[46] A. Gresele, M. Giaretta, A. Visentin, A. Sulimov, and J. Thie. The Statistics of industrial XFEL Cavities fabrication at E. Zanon. In *Proceedings of SRF2013*, pages 180–182, 2013. (Cited on pages 13 and 60.)

[47] A. Sulimov, J. Thie, M. Pekeler, and D. Trompetter. The Statistics of industrial XFEL Cavities fabrication at Research Instruments. In *Proceedings of SRF2013*, pages 9–11, 2013. (Cited on pages 13 and 60.)

[48] S. Aderhold, D. Reschke, and J. Schaffran. Test Results for the Testing of 800 Series Cavities for the European XFEL. In *TTC Workshop*, 2014. (Cited on page 13.)

[49] N. Walker. XFEL vertical test results and extrapolation to ILC cavity & test numbers. In *Proceedings of LCWS2014*, 2014. (Cited on pages 13, 28, and 44.)

[50] CORDIS. ILC HiGrade Project. Project reference: 206711, 2008. (Cited on page 13.)

[51] E. Elsen. EU ILC-HiGrade plans and beyond. In *Proceedings of LCWS2011*, 2011. (Cited on page 13.)

[52] ICFA. Final International Technology Recommendation Panel Report. Technical report, ICFA, 2004. (Cited on page 13.)

[53] F. Zimmermann and A. Blondel. A High Luminosity ee Collider in the LHC tunnel to study the Higgs Boson. *ArXiv:1112.2518v1 [hep-ex]*, 12(1):5–12, 2011. (Cited on page 14.)

[54] M. Aicheler, P. Burrows, M. Draper, T. Garvey, and P. Lebrun. A Multi-TeV Linear Collider based on CLIC Technology: CLIC Conceptual Design Report. Technical report, CERN, 2012. (Cited on page 14.)

[55] F. Simon. Precis of the Physics Case for the ILC. In *Proceedings of LCWS2014*, 2014. (Cited on page 14.)

[56] S. Asai, M. Hazumi, K. Hanagaki, and J. Hisano. The Final Report of the Subcommittee on Future Projects of High Energy Physics 1. Technical report, Japanese Physics Society, 2012. (Cited on page 14.)

[57] I. Blumenfeld, C. Clayton, F. Decker, et al. Energy doubling of 42 GeV electrons in a metre-scale plasma wakefield accelerator. *Nature*, 445(7129):741–744, February 2007. (Cited on page 14.)

[58] C. Adolphsen, C. Beard, L. Bellantoni, et al. Design of the ILC Crab Cavity System. Technical report, slac-pub-12751, 2007. (Cited on page 15.)

[59] H. Aihara, P. Burrows, and M. Oreglia. SiD Letter of Intent. *arXiv preprint arXiv:0911.0006*, 2009. (Cited on page 15.)

[60] T. Abe, S. Schuwalow, M. Yamauchi, et al. The international large detector: Letter of intent. Technical report, Fermilab, DESY, KEK, 2010. (Cited on page 15.)

[61] T. Behnke, J. Brau, P. Burrows, J. F. Verdu, and M. Peskin. ILC TDR Volume 3 : Physics and Detectors - Detailed Baseline Design. Technical report, ILC GDE, 2012. (Cited on page 15.)

[62] H. Kamerlingh Onnes. On the change of electric resistance of pure metals at very low temperatures, etc. IV. The resistance of pure mercury at helium temperatures. *Comm. Phys. Lab. Univ. Leiden*, 120b, 1911. (Cited on page 18.)

[63] H. Kamerlingh Onnes. On the change of electric resistance of pure metals at very low temperatures, etc. V. The disappearance of the resistance of mercury. *Comm. Phys. Lab. Univ. Leiden*, 122b, 1911. (Cited on page 18.)

References

[64] H. Kamerlingh Onnes. On the electrical resistance of pure metals, etc. VI. On the sudden change in the rate at which the resistance of mercury disappears. *Comm. Phys. Lab. Univ. Leiden*, 124c, 1911. (Cited on page 18.)

[65] J. Kirchgessner, H. Padamsee, H. L. Phillips, et al. Superconducting Cavities for Synchrotron Use. *IEEE Transactions on Nuclear Science*, NS-22(3), 1975. (Cited on page 18.)

[66] M. Tigner. CESR - An Electron Positron Colliding Beam Facility at Cornell. *IEEE Transactions on Nuclear Science*, 24(3), 1977. (Cited on page 18.)

[67] B. Aune, R. Bandelmann, D. Bloess, and B. Bonin. Superconducting TESLA cavities. *Physical Review Special*, 3, 2000. (Cited on pages 18, 20, 23, 36, 120, and CXLVII.)

[68] C. Reynolds, B. Serin, W. Wright, and L. Nesbitt. Superconductivity of Isotopes of Mercury. *Physical Review*, 78(4):487, 1950. (Cited on page 18.)

[69] E. Maxwell. Isotope Effect in the Superconductivity of Mercury. *Physical Review*, 78(4):477, 1950. (Cited on page 18.)

[70] L. Cooper. Bound Electron Pairs in a Degenerate Fermi Gas. *Physical Review*, 104(4):1189–1190, November 1956. (Cited on page 18.)

[71] J. Bardeen, L. Cooper, and J. Schrieffer. Theory of superconductivity. *Physical Review*, 108:1175–1204, 1957. (Cited on page 18.)

[72] M. J. Buckingham. Very High Frequency Absorption in Superconductors. *Physical Review*, 101(4):1431–1432, February 1956. (Cited on page 19.)

[73] Crankshaft Publishing. Electrical Conduction in Metals and Alloys, 1999. (Cited on pages 19 and CXXXVII.)

[74] D. Mattis and J. Bardeen. Theory of the Anomalous Skin Effect in Normal and Superconducting Metals. *Physical Review*, 111(2):412–417, 1958. (Cited on pages 20 and 38.)

[75] H. Padamsee, J. Knobloch, and T. Hays. *RF Superconductivity for Accelerators*. Wiley-VCH Verlag, Weinheim, 2008. (Cited on pages 20, 23, 27, 30, 37, 38, 43, 47, 49, 104, 116, CXXXVIII, and CXXXIX.)

[76] F. London and H. London. The Electromagnetic Equations of the Supraconductor. *Proceedings of the Royal Society of London*, A149(886:71), 1935. (Cited on page 20.)

[77] W. Meissner and R. Ochsenfeld. Ein neuer Effekt bei Eintritt der Supraleitfähigkeit. *Naturwissenschaften*, 21(44):787–788, 1933. (Cited on page 20.)

[78] V.L. Ginzburg and L.D. Landau. Ginzburg-Landau-Theorie. *Zh. Eksp. Teor. Fiz*, 20(1064):546, 1950. (Cited on page 20.)

[79] L. Gorkov. Microscopic derivation of the Ginzburg Landau equations in the theory of Superconductivity. *Sov.phys.JETP*, 9:1364, 1959. (Cited on page 20.)

[80] L.W. Shubnikow, W.I. Chotkewitsch, J.D. Schepele, and J.N. Rjabinin. Magnetic properties of superconducting metals and alloys. *Zh. Exper. Teor. Fiz.*, V.7.(No.2):221–237, 1936. (Cited on page 20.)

[81] A. A. Abrikosov. On the Magnetic Properties of Superconductors of the Second Group. *Zh. Eksp. i Teor. Fiz.*, 32:1442, 1957. (Cited on page 20.)

[82] N. R. A. Valles and M. U. Liepe. Temperature dependence of the superheating field in niobium. *ArXiv preprint arXiv:1002.3182 (2010)*, page 8, 2010. (Cited on page 21.)

[83] R-B. Flippen. The radial velocity of magnetic field penetration in type II superconductors. *Physics Letters*, 17(3):193–194, 1965. (Cited on pages 21 and 32.)

[84] S. J. Chapman. Superheating Field of type-II superconductors. *SIAM Journal on Applied Mathematics*, 55:1233–1258, 1995. (Cited on page 21.)

[85] R. Miller. Comparison of Standing Wave and Traveling Wave Structures. *Conf.Proc.*, C860602:200, 1986. (Cited on page 22.)

[86] V. A. Moiseev, V. V. Paramonov, and K. Floettmann. Comparison of Standing and Travelling Wave Operations for a Positron Pre-Accelerator in the TESLA Linear Collider. In *Proceedings of EPAC 2000*, pages 842–844, 2000. (Cited on page 22.)

[87] E. Vogel, Ch. Gerth, W. Koprek, et al. Beam loading compensation using real time bunch charge information from toroid monitor at flash. In *Proceedings of PAC2007*, pages 2074–2076, 2007. (Cited on page 22.)

[88] F. Bumiller. Untersuchung über Vakuumüberschläge an Beschleunigungsrohren. *Zeitschrift Angewandte Mathematik und Physik*, 7:366–369, 1956. (Cited on page 22.)

[89] R. L. Geng, H. Padamsee, A. Seaman, and V. D. Shemelin. World Record Accelerating Gradient Achieved in a Superconducting Niobium RF Cavity. *Proceedings of PAC2005*, pages 653–655, 2005. (Cited on page 22.)

[90] J. Sekutowicz, K. Ko, L. Ge, et al. Design of a low loss SRF cavity for the ILC. In *Proceedings of PAC2005*, pages 3342–3344, 2005. (Cited on page 22.)

References

[91] F. Furuta, K. Saito, T. Saeki, et al. Experimental Comparison at KEK of High Gradient Performance of Different Single Cell Superconducting Cavity Designs. In *Proceedings of EPAC 2006*, pages 750–752, 2006. (Cited on page 22.)

[92] R. L. Geng. Review of new shapes for higher gradients. Technical Report 1, Cornell University, 2006. (Cited on page 22.)

[93] M. Ross, N. Walker, and A. Yamamoto. Plug Compatibility. Technical report, D00000000865055, 2009. (Cited on page 22.)

[94] A. Bosotti, C. Pagani, R. Paparella, et al. S1-Global Report. Technical report, D00000001005135, 2012. (Cited on page 22.)

[95] S. Aderhold, A. Gössel, J. Iversen, et al. Update on Large Grain Cavities with 45 MV/M in a Nine-Cell Cavity at DESY. In *Proceedings of SRF2011*, pages 1–4, 2011. (Cited on pages 23 and 39.)

[96] M. Pekeler. *Untersuchungen der feldbegrenzenden Mechanismen in supraleitenden Niob-Resonatoren*. PhD thesis, Universität Hamburg, 1996. (Cited on pages 23, 46, CXXXVIII, and CXXXIX.)

[97] D. E. Nagle, E. A. Knapp, and B. C. Knapp. Coupled Resonator Model for Standing Wave Accelerator Tanks. *The Review of Scientifc Instruments*, 38(11), 1967. (Cited on page 23.)

[98] T. Schilcher. *Vector Sum Control of Pulsed Accelerating Fields in Lorentz Force Detuned Superconducting Cavities*. PhD thesis, Universität Hamburg, 1998. (Cited on page 23.)

[99] P. Lapostolle and A. Septier. *Linear Accelerators*. CERN, New York, xxii edition, 1970. (Cited on page 24.)

[100] J. Frisch, L. Hendrickson, D. Mccormick, et al. High Precision SC Cavity Diagnostics with HOM Measurements. Technical report, DESY, 2006. (Cited on page 24.)

[101] H. Podlech. Superconducting versus normal conducting cavities. *ArXiv e-prints*, 2013. (Cited on page 26.)

[102] M. Liepe, S. Belomestnykh, J. Dobbins, et al. Pushing the limits: RF field control at high loaded Q. In *Proceedings of PAC2005*, pages 2642–2644. IEEE, 2005. (Cited on page 26.)

[103] K. Saito. Basic Principles of SRF. In *Proceedings of SRF2005*, page Tutorial at the SRF Workshop 2005. KEK, 2005. (Cited on pages 26 and CXXXVIII.)

[104] J. Norem and M. Pellin. Gradient limits and SCRF performance. In *Proceedings of SRF2007*, pages 0–2, 2007. (Cited on page 26.)

[105] P. Bauer, G. L. Ciovati, A. Gurevich, et al. A comparison of Q-slope models and data in bulk Nb SRF cavities. In *SRF material meetings, FNAL*, 2005. (Cited on pages 26, 30, 31, 37, and CXXXVIII.)

[106] A. Chao and M. Tigner. *Handbook of accelerator physics and engineering*. World Scientific Publishing Company Incorporated, 2nd editio edition, 1999. (Cited on page 27.)

[107] D. Proch and U. Klein. Multipacting in Superconducting RF structures. In *Proceedings Conference for Future Possibilities for Electron Accelerators*, 1979. (Cited on page 27.)

[108] B. Bonin. Q degradation of Niobium cavities due to Hydrogen contamination. In *Proceedings of SRF1991*, 1991. (Cited on page 27.)

[109] A. D. Le Claire. The analysis of grain boundary diffusion measurements. *British Journal of Applied Physics*, 14(6):351, 1963. (Cited on page 27.)

[110] B. Roux, H. Jaffrezic, A. Chevarier, N. Chevarier, and M. T. Magda. Molecular-dynamics simulations of hydrogen diffusion in niobium: Influence of imperfections. *Physical Review B*, 52(6):4162–4170, August 1995. (Cited on page 27.)

[111] K. Schulze, O. Bach, D. Lupton, and F. Schreiber. Purification of niobium. *Niobium-Proceedings of the international symposium*, pages 163–223, 1981. (Cited on page 28.)

[112] R.H. Fowler and L. Nordheim. Electron Emission in Intense Electric Fields. *Proceedings of the Royal Society of London Series A*, 119:173–181, 1928. (Cited on page 28.)

[113] B. Bonin. Field Emission in RF Cavities. In *CERN Accelerator School*, 1995. (Cited on page 28.)

[114] H. A. Schwettman, J. P. Turneaure, and R. F. Waites. Evidence for surface-state-enhanced field emission in RF superconducting cavities. *Journal of Applied Physics*, 45(2):914–922, 1974. (Cited on page 28.)

[115] A. Navitski. Surface roughness and correlated field emission investigations of electropolished Nb samples. In *Terascale Workshop*, number November, 2009. (Cited on page 28.)

[116] R. V. Latham. Prebreakdown Electron Emission. *IEEE Transactions on Electrical Insulation*, EI-18(3):194–203, 1983. (Cited on page 28.)

[117] D. Reschke, X. Singer, G. Müller, and A. Pandey. Field emission from crystalline niobium. *Physical Review Special Topics - Accelerators and Beams*, 023501(12):1–8, 2009. (Cited on pages 28, 29, and CXXXVIII.)

References

[118] B. Bonin. Field emission and surface conditioning. *Vacuum*, 46(8 - 10):907–912, 1995. (Cited on page 28.)

[119] R. L. Geng, G. Ciovati, and A. C. Crawford. Gradient Limiting Defects in 9-Cell Cavities EP Processed and RF at Jefferson Lab. In *Proceedings of SRF2009*, pages 370–374, 2009. (Cited on pages 29, 53, and 117.)

[120] H. Padamsee, D. Proch, P. Kneisel, and J. Mioduszewski. Field strength limitations in superconducting cavities-multipacting and thermal breakdown. *IEEE Transactions on Magnetics*, 17:947–950, 1981. (Cited on page 29.)

[121] H. Padamsee. Heat Transfer and Models for Breakdown. In *Proceedings of SRF1980*, pages CLNS—-340, 1980. (Cited on page 29.)

[122] H. Safa. An Analytical Approach for Calculating the Quench Field in Superconducting Cavities. In *Proceedings of SRF1995*, pages 413–418, 1995. (Cited on pages 29 and 117.)

[123] Y. Xie, M. Liepe, D. Meidlinger, and H. Padamsee. Thermal modeling of ring-type defects. In *Proceedings of SRF2009*, pages 331–333, 2009. (Cited on pages 29 and 117.)

[124] H. Safa. Statistical analysis of the quench fields in SCRF cavities. In *Proceedings of SRF1997*, pages 1–9, 1997. (Cited on page 29.)

[125] H. Padamsee. Calculations for breakdown induced by "large defects" in superconducting niobium cavities. *IEEE Transactions on Magnetics*, 19(CERN-EF-RF-82-5):1322–1325, 1982. (Cited on page 29.)

[126] Y. Xie, H. Padamsee, and O. Romanenko. Relationship between defects pre-heating and defects size. In *Proceedings of SRF2009*, pages 5–8, 2009. (Cited on page 29.)

[127] S.-H. Kim and O. Ridge. Simulation of quench dynamics in SRF cavities under pulsed operation. In *Proceedings of PAC2003*, pages 1365–1367, 2003. (Cited on page 29.)

[128] D. Meidlinger. Basic understanding for the various causes of quench. In *Proceedings of SRF2009*, pages 117–122, 2009. (Cited on page 29.)

[129] A. Ermakov, I. Jelezov, X. Singer, and W. Singer. Physical Properties and Structure of Large Grain / Single Crystal Niobium for Superconducting RF Cavities. *Applied Superconductivity*, 97(Eucas 2007):1–8, 2008. (Cited on page 30.)

[130] P. Dhakal, G. Ciovati, P. Kneisel, and G. Myneni. Superconducting DC and RF Properties of Ingot Niobium. *ArXiv e-prints*, 2(1202.0811), 2012. (Cited on page 30.)

[131] B. Visentin. Q-Slope at High Gradients: Review about Experiments and Explanations. In *Proceedings of SRF2003*, 2003. (Cited on page 30.)

[132] J. Knobloch, R. L. Geng, M. Liepe, and H. Padamsee. High-field Q slope in superconducting cavities due to magnetic field enhancement at grain boundaries. *Proceedings of SRF1999*, pages 77–91, 1999. (Cited on pages 30, 31, 89, 90, 104, 128, CXXXVIII, and CXLII.)

[133] V. Shemelin and H. Padamsee. Magnetic field enhancement at pits and bumps on the surface of superconducting cavities. Technical report, Cornell University, 2008. (Cited on pages 30, 31, and CXXXVIII.)

[134] T. Kubo. Models of the magnetic field enhancement at pits. *ArXiv preprint arXiv:1308.3311*, (5):1–5, 2013. (Cited on page 30.)

[135] G. Ciovati and A. Gurevich. Measurement of RF losses due to trapped flux in a large grain niobium cavity. In *Proceedings of SRF2007*, pages 132–136, 2007. (Cited on page 32.)

[136] G. Ciovati and A. Gurevich. Evidence of high-field radio-frequency hot spots due to trapped vortices in niobium cavities. *Applied Superconductivity*, 122001:1–12, 2008. (Cited on page 32.)

[137] A. Buzdin and M. Daumens. Electromagnetic pinning of vortices on different types of defects. *Physica C: Superconductivity*, 294(3-4):257–269, 1998. (Cited on pages 32 and 129.)

[138] A. Dzyuba, A. Romanenko, and L. D. Cooley. Model for initiation of quality factor degradation at high accelerating fields in superconducting radio-frequency cavities. *Superconductor Science and Technology*, 23(12):125011, 2010. (Cited on pages 32 and 129.)

[139] L. Lilje. *Experimental Investigations on Superconducting Niobium Cavities at Highest Radiofrequency Fields*. PhD thesis, Universität Hamburg, 2001. (Cited on pages 32, 35, and 42.)

[140] H. Shiraishi, K. Furuya, and R. Watanabe. Change in solute oxygen level and loss of ductility of niobium during oxidation in imperfect vacuum conditions. *Journal of the Less Common Metals*, 63(2):147–158, 1979. (Cited on page 32.)

[141] C. Antoine, B. Berthier, B. Bonin, et al. Evidence of preferential diffusion and segregation of impurities at grain boundaries in very pure niobium used radiofrequency cavities. In *Proceedings of SRF1995*, 1995. (Cited on page 32.)

[142] C. Antoine, H. Safa, B. Berthier, et al. Nuclear Microprobe Studies of Impurities Segregation in Niobium Used for Radiofrequency Cavities. In *Proceedings of SRF1997*, pages 911–917, 1997. (Cited on page 32.)

References

[143] C. Antoine, A. Aspart, S. Regnault, and A. Chincarini. Surface Studies: Method of analysis and results. In *Proceedings of SRF2001*, 2001. (Cited on page 32.)

[144] E. W. Hart. On the role of dislocations in bulk diffusion. *Acta Metallurgica*, 5(10):597 –, 1957. (Cited on pages 32 and 33.)

[145] P. Heitjans and J. Kärger. *Diffusion in condensed matter*. Springer, 2005. (Cited on pages 32 and 33.)

[146] J. Fuss. Diplomarbeit. Universtität Stuttgart, 1976. (Cited on page 32.)

[147] M. Hörmann. Erstellung von hochwärmeleitfähigen Niob im technischen Maßstab für die Hochfrequenzsupraleitung. *Zeitschrift für Metallkunde*, 77(5):338–347, 1986. (Cited on pages 32 and CXLVII.)

[148] K.K. Schulze. Preparation and characterization of ultra-high-purity niobium. *Journal of Metal*, 33:33 – 41, 1981. (Cited on pages 32, 37, and CXLVII.)

[149] A. Grassellino, A. Romanenko, D. Sergatskov, et al. Nitrogen and argon doping of niobium for superconducting radio frequency cavities: a pathway to highly efficient accelerating structures. *Superconductor Science and Technology*, 26(10):102001, 2013. (Cited on pages 33 and 129.)

[150] T. L. Hylton, A. Kapitulnik, M. R. Beasley, et al. Weakly coupled grain model of high-frequency losses in high Tc superconducting thin films. *Applied Physics Letters*, 53(14):1343–1345, 1988. (Cited on page 33.)

[151] H. Safa, M. Boloré, Y. Boudigou, et al. Specific Resistance Measurement of a Single Grain Boundary in Pure Niobium. In *Proceedings of SRF1999*, pages 267–269, 1999. (Cited on page 33.)

[152] K. Schulze. Extractive metallurgy of refractory metals. In *Chicago Conference*, 1981. (Cited on page 33.)

[153] V. Ambegaokar and A. Baratoff. Tunneling Between Superconductors. *Physical Review Letters*, 10(11):486–489, June 1963. (Cited on page 33.)

[154] S. Aderhold, S. Chel, E. Elsen, et al. Cavity Process. *ILC HiGrade Report*, pages 1–5, 2010. (Cited on pages 35, 40, 41, 93, 107, and CXXXVIII.)

[155] X. Singer, J. Iversen, W. Singer, et al. Material for fabrication of large grain cavities for European XFEL. In *Proceedings of SRF2011*, page 22603, 2011. (Cited on pages 35 and 39.)

[156] W. Singer. XFEL Cavity Recipe for Mechanical Fabrication and Treatment. In *Proceedings of SRF2011*, 2011. (Cited on pages 35 and 111.)

[157] W. Singer, A. Brinkmann, D. Proch, and X. Singer. Quality requirements and control of high purity niobium for superconducting RF cavities. *Physica C: Superconductivity*, 386(0):379–384, 2003. (Cited on pages 35 and 38.)

[158] P. Kneisel, G. Ciovati, P. Dhakal, et al. The Rise of Ingot Niobium as a Material for Superconducting Radiofrequency Accelerating Cavities. *ArXiv e-prints*, pages 1–51, 2013. (Cited on page 35.)

[159] R. Grill, W. Simader, D. Janda, et al. Correlation of Microstructure , Chemical Composition and RRR-Value in High Purity Niobium (Nb-RRR). In *Proceedings of SRF2011*, pages 863–867, 2011. (Cited on page 37.)

[160] P. Kneisel, G. Ciovati, G. R. Myneni, et al. Influence of Ta content in high purity niobium on cavity performance. In *Proceedings of PAC2005 Accelerator Conference*, volume 2005, pages 3955–3957, 2005. (Cited on page 37.)

[161] B. Bonin. Materials for Superconducting Cavities. In *CERN Accelerator School*, pages CERN–96–0, 1995. (Cited on page 37.)

[162] L. P. Kadanoff and P. C. Martin. Theory of Many-Particle Systems. II. Superconductivity. *Physical Review*, 124(3):670–697, November 1961. (Cited on page 38.)

[163] H. Umezawa. Niobium Production at Tokyo Denkai. In *First International Symposium on the Superconducting Science and Technology of Ingot Niobium*, volume 1352, pages 79–83. AIP Publishing, 2011. (Cited on page 38.)

[164] A. Brinkmann, M. Lengkeit, X. Singer, and W. Singer. Testing of Niobium Material for the European XFEL Pre-series Production. *Proceedings of LINAC2010*, 2010. (Cited on page 38.)

[165] W. Singer, D. Proch, and A. Brinkmann. Diagnostic of Defects in High Purity Niobium. In *Proceedings of SRF1997*, number figure 1, pages 850–863, 1997. (Cited on page 38.)

[166] R. Grill, W. Simader, B. Paniol, and W. Feuring. Production of High-Purity-Niobium Under Industrial Scale for Upcoming Linear Collider Projects. In *Proceedings of PAC2009*, 2009. (Cited on page 38.)

[167] H. Jiang, T. R. Bieler, C. Compton, and T. L. Grimm. Mechanical properties, microstructure, and texture of electron beam butt welds in high purity Niobium. In *Proceedings of PAC2003*, volume 2, pages 1359–1361. IEEE, 2003. (Cited on pages 39 and CXLVII.)

[168] C. Antoine. Materials and surface aspects in the development of SRF Niobium cavities Materials and surface aspects in the development of SRF Niobium

cavities. Technical Report 227579, CEA Saclay, 2012. (Cited on pages 39, 44, CXXXIX, and CXLVII.)

[169] W. Singer, S. Aderhold, J. Iversen, et al. Development of Large Grain Superconducting Resonators for the European XFEL. In *Proceedings of SRF2009*, pages 150–152, 2009. (Cited on pages 38 and 39.)

[170] P. Kneisel, G. R. Myneni, G. Ciovati, J. Sekutowicz, and T. Carneiro. Preliminary Results From Single Crystal and Very Large Crystal Niobium Cavities. In *Proceedings of PAC2005*, pages 3991–3993, 2005. (Cited on page 39.)

[171] W. Singer, S. Aderhold, J. Iversen, et al. Advances in Large Grain Resonators for the European XFEL. In *American Institute of Physics Conference Series*, pages 13–24, 2011. (Cited on page 39.)

[172] G. Kreps, D. Proch, and J. Sekutowicz. Half-Cell and Dumb-Bell Frequency Testing for the Correction of the Tesla Cavity Length. In *Proceedings of SRF1999*, number d, 1999. (Cited on page 39.)

[173] J. Iversen, A. Goessel, D. Klinke, G. Kreps, and C. Mueller. Development and design of a RF-measurement machine for the european XFEL cavity fabrication. In *Proceedings of SRF2009*, pages 786–790, 2009. (Cited on page 39.)

[174] J. L. Kirchgessner. Forming and Welding of Niobium for Superconducting Cavities. In *Proceedings of SRF1987*, 1987. (Cited on pages 39 and 40.)

[175] P. N. Potukuchi, L. S. S. Chandra, M. K. Chattopadhyay, et al. Superconducting properties of niobium after electron beam welding. *Physical Review Special Topics - Accelerators and Beams*, 14(12):122001, 2011. (Cited on page 40.)

[176] R. L. Geng, J. Knobloch, and H. Padamsee. Mirco-Structures of RF Surfaces in the Electron-Beam-Weld Regions of Niobium. In *Proceedings of SRF1999*, 1999. (Cited on pages 40, 92, 116, and CXLIII.)

[177] J. Sekutowicz, C. Yinghua, and W. E. Yixiang. A different tuning method for accelerating cavities. In *Proceedings of SRF1989*, 1989. (Cited on page 40.)

[178] J. Thie, A. Goessel, J. Iversen, et al. Commissioning and Upgrade of Automatic Cavity Tuning Machines for the European XFEL. In *Proceedings of SRF2011*, 2011. (Cited on page 40.)

[179] M. Grundner. *Oberflächenuntersuchungen an Niob für supraleitende Resonatoren mittels der Röntgen-Photoelektronenspektroskopie und der Auger-Elektronenspektroskopie*. PhD thesis, Universität Karlsruhe, 1977. (Cited on page 40.)

[180] A. Dacca, G. Gemme, L. Mattera, and R. Parodi. XPS analysis of the surface composition of niobium for superconducting RF cavities. *Applied Surface Science*, 126(3):219–230, 1998. (Cited on page 40.)

[181] J. Guerin. Etude du bain de polissage chimique de niobium. Technical report, CERN, 1989. (Cited on page 42.)

[182] R. Hillenbrand, N. Krause, K. Schmitzke, and Y. Uzel. Abschlussbericht - Supraleitenden Resonatoren. Technical report, Siemens AG, 1982. (Cited on page 42.)

[183] R. Röth. *Untersuchungen zu anomalen Verlusten in Niobresonatoren*. PhD thesis, Universität Wuppertal, 1993. (Cited on page 42.)

[184] L. Lilje, A. Matheisen, D. Proch, et al. Improved Surface Treatment of the Superconducting TESLA Cavities 1. *Nuclear Instruments and Methods in Physics Research Section A: Accelerators, Spectrometers, Detectors and Associated Equipment*, 516.2, 2004. (Cited on pages 42, 43, and CXXXIX.)

[185] W.C. Elmore. Electrolytic Polishing. *Journal of Applied Physics*, 10(724), 1939. (Cited on page 42.)

[186] W.C. Elmore. Electrolytic Polishing II. *Journal of Applied Physics*, 11(797), 1940. (Cited on page 42.)

[187] A. Citron, G. Dammertz, M. Grundner, et al. The Karlsruhe-CERN superconducting RF separator. *Nuclear Instruments and Methods*, 164(31):55, 1979. (Cited on page 42.)

[188] K. Saito. Electropolishing of L-band cavities. Technical report, KEK Report 89-21, 1989. (Cited on page 42.)

[189] G. Ciovati, T. Higo, P. Kneisel, et al. Final Surface Preparation for Superconducting Cavities. Technical report, Fermilab, 2008. (Cited on pages 42, 116, and CXXXIX.)

[190] L. Ponto and M. Hein. Elektropolitur von Niob. Technical report, Bergische Universität Wuppertal, 1986. (Cited on page 42.)

[191] H. Tan. *Surface Study of Niobium for SRF Accelerators*. PhD thesis, The College of William and Mary, 2008. (Cited on page 42.)

[192] K. Saito, H. Inoue, E. Kako, and T. Fujino. Superiority of Electropolishing over Chemical Polishing on High Gradients. In *Proceedings of SRF1997*, pages 795–813, 1997. (Cited on page 43.)

References

[193] B. Visentin, J. P. Charrier, and B. Coadou. Improvements of Superconducting Cavity Performances at High Accelerating Gradients. In *Proceedings of EPAC 1998*, number June in Proceedings, pages 5–7, 1998. (Cited on page 43.)

[194] P. Kneisel. Preliminary Experience with 'in-Situ' Baking of Niobium Cavities. In *Proceedings of SRF1999*, pages 328 – 335, 1999. (Cited on page 43.)

[195] G. Ciovati, G. Myneni, F. Stevie, P. Maheshwari, and D. Griffis. High field Q slope and the baking effect: Review of recent experimental results and new data on Nb heat treatments. *Physical Review Special Topics - Accelerators and Beams*, 13(2):22002, February 2010. (Cited on page 44.)

[196] A. Matheisen, K. Escherich, R. Bandelmann, H. M. Zimmermann, and N. Krupka. A New High Pressure Rinsing System Established at DESY. In *Proceedings of SRF2009*, pages 794–796, 2009. (Cited on page 44.)

[197] J. H. Hetherington and F. D. C. Willard. Two-, Three-, and Four-Atom Exchange Effects in bcc 3He. *Physical Review Letters*, 35(21):1442–1444, November 1975. (Cited on page 45.)

[198] F.D.C. Willard. L'helium 3 solide. Un antiferromagnetique nucleaire. *La Recherche*, 114, 1980. (Cited on page 45.)

[199] M. Wenskat. Studies to optimize the accelerating gradient of the superconducting TESLA cavities for the International Linear Collider. Diplomarbeit. Universität Göttingen, 2010. (Cited on pages 47 and CXXXIX.)

[200] J. Knobloch. Basic Concepts of Measurements Made on Superconducting RF Cavities. In *Proceedings of SRF1991*, number August, 1991. (Cited on page 47.)

[201] F. Schlander. *Study of Quality and Field Limitation of Superconducting 1.3 GHz 9-Cell RF-Cavities at DESY*. PhD thesis, Universität Hamburg, 2012. (Cited on pages 48, 51, 121, and CXXXIX.)

[202] H. E. Feisi. Uncertainty of data obtained in SRF cavity vertical test. *ArXiv e-prints*, 2013. (Cited on page 48.)

[203] K. Yamamoto. Results of performance test and error estimation in AMTF, 2015. (Cited on page 48.)

[204] T. Tajima, K. Asano, T. Furuya, et al. Temperature mapping system developed at KEK for field emission studies on superconducting cavities. *15th International Conference on High-energy Accelerators*, (1):751–753, August 1992. (Cited on page 48.)

[205] J. Knobloch. Field emission and thermal breakdown in superconducting niobium cavities for accelerators. *IEEE Transactions on Applied Superconductivity*, 9(2):1016–1022, 1999. (Cited on pages 49 and CXXXIX.)

[206] Z. A. Conway, D. L. Hartill, H. S. Padamsee, and E. N. Smith. Defect location in superconducting cavities cooled with He-II using Oscillating Superleak Transducers. In *Proceedings of SRF2009*, pages 113–116, 2009. (Cited on page 50.)

[207] L. Tisza. Sur la théorie des liquides quantiques. Application à l'hélium liquide. *Journal De Physique Et Le Radium*, 1(8):350–358, 1940. (Cited on page 50.)

[208] L. Tisza. Theory of Liquid Helium. *Physical Review*, 72(9):17, 1947. (Cited on page 50.)

[209] L. Tisza. Theory of Superconductivity. *Physical Review*, 80(4):10, 1950. (Cited on page 50.)

[210] J. Peshkov. Determination of the velocity of propagation of the second sound in helium II. *J. Phys.*, 10:389, 1946. (Cited on page 50.)

[211] R. Williams, S. Beaver, J. C. Fraser, R. S. Kagiwada, and I. Rudnick. The velocity of second sound near Tλ. *Physics Letters A*, 29(5):279–280, 1969. (Cited on page 50.)

[212] E. Sherlock. Oscillating Superleak Second Sound Transducers. *Review of Scientific Instruments*, 41(11):1603–1609, 1970. (Cited on page 50.)

[213] Y. Tamashevich. New insights into second sound quench evaluation. In *TTC Workshop*, 2014. (Cited on pages 51, 123, 124, and CXLV.)

[214] R. Laasch. Quench detection with 2nd sound. In *DPG-Frühjahrstagung 2015*, 2015. (Cited on page 51.)

[215] Y. Iwashita, Y. Tajima, and H. Hayano. Development of high resolution camera for observations of superconducting cavities. *Physical Review Special Topics - Accelerators and Beams*, 11(9):1–9, September 2008. (Cited on pages 51, 53, 56, 62, and CXL.)

[216] M. Lemke, E. Elsen, S. Aderhold, et al. OBACHT - Optical Bench for Automated Cavity Inspection with High Resolution on Short Time Scales. Technical report, DESY, 2013. (Cited on pages 51, 54, 57, and CXL.)

[217] S. Aderhold. *Study of field-limiting defects in superconducting RF cavities for electron-accelerators*. PhD thesis, Universität Hamburg, 2015. (Cited on pages 51, 53, 56, 59, 61, 87, 108, 117, CXL, CXLII, and CXLIV.)

[218] T. Tajima, A. Canabal, T. Harden, and R. Roybal. Conceptual design of automated systems for SRF cavity optical inspection and assembly. In *Proceedings of EPAC 2008*, pages 922–924, 2008. (Cited on pages 53 and 56.)

[219] K. Watanabe. Review of optical inspection methods and results. In *Proceedings of SRF2009*, pages 123–128, 2009. (Cited on pages 53 and 117.)

[220] W.-D. Möller. Review of results from temperature mapping and subsequent cavity inspection. In *Proceedings of SRF2009*, pages 109–112, 2009. (Cited on pages 53 and 117.)

[221] S. Aderhold. Optical Inspection of SRF Cavities at DESY Comparison of Optical Inspection and T-Map Data. In *Proceedings of IPAC2010*, pages 2896–2898, 2010. (Cited on pages 53 and 117.)

[222] W. Singer, X. Singer, S. Aderhold, et al. Surface investigation on prototype cavities for the European X-ray Free Electron Laser. In *Proceedings of IPAC2011*, volume 14, pages 2902–2904, 2011. (Cited on pages 53 and 117.)

[223] L. Steder. The Optical Cavity-Inspection Tool OBACHT - to be published. Technical Report ILC, DESY, 2013. (Cited on page 55.)

[224] L. Steder. Measurement Manual for OBACHT. Technical report, DESY, 2012. (Cited on page 55.)

[225] Y. Iwashita, H. Fujisawa, H. Tongu, et al. R&D of Nondestructive Inspection Systems for SRF Cavities. In *Proceedings of SRF2009*, number 3, pages 297–299, 2009. (Cited on page 56.)

[226] B. E. Bayer. Color Imaging Array. Patent US3971065, 1976. (Cited on page 57.)

[227] X. Liu, M. Tanaka, and M. Okutomi. Single-Image Noise Level Estimation for Blind Denoising. *IEEE Transactions on Image Processing*, 22(12):5226–5237, 2013. (Cited on page 57.)

[228] H. Kirshner, F. Aguet, D. Sage, and M. Unser. 3-D PSF Fitting for Fluorescence Microscopy: Implementation and Localization Application. *Journal of Microscopy*, 249(1):13–25, 2014. (Cited on page 58.)

[229] A. Griffa, N. Garin, and D. Sage. Comparison of Deconvolution Software in 3D Microscopy: A User Point of View - Part 1. *G.I.T. Imaging & Microscopy*, 12(1):43–45, 2010. (Cited on page 58.)

[230] M. Born and E. Wolf. *Principles of Optics*. Cambridge University Press, 7th editio edition, 2003. (Cited on page 58.)

[231] S. Frisken-Gibson and F. Lanni. Diffraction by a circular aperture as a model for three-dimensional optical microscopy. *Journal of the Optical Society of America A*, 6(9), 1989. (Cited on page 58.)

[232] USAF. MIL-STD-150A, 1951. (Cited on page 58.)

[233] B. Forster, D. Van De Ville, J. Berent, D. Sage, and M. Unser. Complex wavelets for extended depth-of-field: A new method for the fusion of multichannel microscopy images. *Microscopy Research and technique*, 65(1-2):33–42, 2004. (Cited on page 59.)

[234] K. Watanabe. Recent inspection results by Kyoto-camera. In *TTC Workshop*, pages 1–19, 2008. (Cited on page 61.)

[235] D. R. Martin, C. C. Fowlkes, and J. Malik. Learning to detect natural image boundaries using local brightness, color and texture cues. *IEEE transactions on pattern analysis and machine intelligence*, 26(5):530–549, 2004. (Cited on page 63.)

[236] CIE. CIE(1931). In *Commission internationale de l'Eclairage proceedings*. Cambridge University Press, 1931. (Cited on page 65.)

[237] A. D. Broadbent. A critical review of the development of the CIE1931 RGB color-matching functions. *Color Research & Application*, 29(4):267–272, 2004. (Cited on page 65.)

[238] P. S. Heckbert. Graphics Gems IV. chapter Contrast, page 575. Academic Press Professional, Inc., San Diego, CA, USA, 1994. (Cited on pages 66 and 68.)

[239] S. M. Pizer, E. P. Amburn, and J. D. Austin. Adaptive Histogram Equalization and Its Variations. *Computer Vision, Graphics and Image Processing*, 39:355–368, 1987. (Cited on page 66.)

[240] J. S. Lim. *Two-Dimensional Signal and Image Processing*. Prentice Hall, Englewood Cliffs, NJ, 1990. (Cited on page 68.)

[241] E. Arias-Castro and D. L. Donoho. Does median filtering truly preserve edges better than linear filtering? *The Annals of Statistics*, 37(3):1172–1206, 2009. (Cited on page 68.)

[242] N. Otsu. A Threshold Selection Method from Gray-Level Histograms. *IEEE Transactions on Systems, Man and Cybernetics*, 9:62–66, 1979. (Cited on page 68.)

[243] Labview. Thresholding. *http://zone.ni.com/reference/en-XX/help/372916M-01/nivisionconcepts/thresholding/*, 2013. (Cited on pages 68 and CXLI.)

[244] R. M. Haralick and L. G. Shapiro. *Computer and Robot Vision (Volume I)*. Addison Wesley Longman, 2002. (Cited on pages 69 and 81.)

[245] A. L. Dulmage and N. S. Mendelsohn. Coverings of bipartite graphs. *Canadian Journal of Mathematics*, 10(4):516–534, 1958. (Cited on page 70.)

References

[246] P. Hall. On Representatives of Subsets. *Journal of the London Mathematical Society*, s1-10(1):26–30, 1935. (Cited on page 70.)

[247] B. Jähne. *Practical Handbook on Image Processing for Scientific and Technical Applications*. CRC Press, 2 edition, 2004. (Cited on page 75.)

[248] M.-K. Hu. Visual pattern recognition by moment invariants. *IRE Transactions on Information Theory*, 8(2):179–187, 1962. (Cited on page 80.)

[249] S. B. Patil. Image Processing Method To Measure Sugarcane Leaf Area. *International Journal of Engineering Science and Technology*, 3(8):6394–6400, 2011. (Cited on page 80.)

[250] R. Klette and J. Zunic. On errors in calculated moments of convex sets using digital images. Technical Report May, CITR, The University of Auckland, New Zealand, September 1999. (Cited on pages 81 and 82.)

[251] S. X. Liao. *Image Analysis by Moments*. PhD thesis, University of Manitoba, 1993. (Cited on page 82.)

[252] International Organization for Standardization. ISO 25178 - Geometric Product Specifications (GPS) Surface texture: areal, 2009. (Cited on page 83.)

[253] I. T. Young, J. J. Gerbrands, and L. J. Van Vliet. *Fundamentals of image processing*. Delft University of Technology Delft, The Netherlands, 1998. (Cited on page 84.)

[254] W. Singer, S. Aderhold, A. Ermakov, et al. Development of large grain cavities. *Physical Review Special Topics - Accelerators and Beams*, 16(1):12003, 2013. (Cited on pages 87, 108, and CXLIV.)

[255] H. Tian, G. Ribeill, C. Xu, C. E. Reece, and M. J. Kelley. A novel approach to characterizing the surface topography of niobium superconducting radio frequency (SRF) accelerator cavities. *Applied Surface Science*, 257(11):4781–4786, 2011. (Cited on pages 91, 92, and CXLII.)

[256] C. Xu, H. Tian, C. E. Reece, and M. J. Kelley. Enhanced Characterization of Niobium Surface Topography. *Physical Review Special Topics - Accelerators and Beams*, 14:123501, 2011. (Cited on pages 91 and 116.)

[257] W. Singer. SRF Cavity Fabrication and Materials. *CERN Yellow Report*, 5:171–207, 2014. (Cited on page 94.)

[258] D. Saylor, A. Morawiec, and G. S. Rohrer. Distribution and energies of grain boundaries in magnesia as a function of five degrees of freedom. *Journal of the American Ceramic Society*, 85(12):3081–3083, 2002. (Cited on page 97.)

[259] G. S. Rohrer and D. Saylor. The distribution of internal interfaces in polycrystals. *Zeitschrift für Metallkunde*, 95:197–214, 2004. (Cited on pages 97 and 98.)

[260] J. Gruber, D. C. George, A. P. Kuprat, G. S. Rohrer, and A. D. Rollett. Effect of anisotropic grain boundary properties on grain boundary plane distributions during grain growth. *Scripta Materialia*, 53(3):351–355, 2005. (Cited on page 97.)

[261] J. Li, S. Dillon, and G. S. Rohrer. Relative grain boundary area and energy distributions in nickel. *Acta Materialia*, 57(14):4304–4311, 2009. (Cited on page 97.)

[262] W. T. Read and W. Shockley. Dislocation Models of Crystal Grain Boundaries. *Physical Review*, 78(3):275–289, 1950. (Cited on page 98.)

[263] J. P. Hirth and J. Lothe. *Theory of Dislocations*. Krieger Publishing Company, 1992. (Cited on page 98.)

[264] R. E. Reed-Hill and R. Abbaschian. *Physical Metallurgy Principles*. International Thomson Publishing, 1992. (Cited on page 98.)

[265] S. J. Dillon and G. S. Rohrer. Mechanism for the development of anisotropic grain boundary character distributions during normal grain growth. *Acta Materialia*, 57(1):1–7, 2009. (Cited on page 98.)

[266] G. S. Rohrer. Private Communication, 2015. (Cited on page 98.)

[267] A. Clauset, C. R. Shalizi, and M. E. J. Newman. Power-law distributions in empirical data. *ArXiv e-prints*, page 43, June 2007. (Cited on pages 98 and 99.)

[268] Y. Virkar and A. Clauset. Power-law distributions in binned empirical data. *The Annals of Applied Statistics*, 8(1):89–119, March 2014. (Cited on page 98.)

[269] Y Virkar and A Clauset. Power-law distributions in binned empirical data. *ArXiv e-prints*, August 2012. (Cited on page 98.)

[270] J. Wright, J. Reeds, M. H.. Wright, and P. E. Wright. Convergence Properties of the Nelder-Mead Simplex Method in Low Dimensions. *SIAM Journal of Optimization*, 9:112–147, 1998. (Cited on page 104.)

[271] T. Van Zandt. *Analysis of Response Time Distributions*. John Wiley & Sons, Inc, 2002. (Cited on page 104.)

[272] B. Efron. Bootstrap methods: another look at the jackknife. *The Annals of Statistics*, pages 1–26, 1979. (Cited on pages 104 and 125.)

[273] Ettore Zanon. http://www.zanon.com/. (Cited on page 107.)

References

[274] Research Instruments. http://www.research-instruments.de/. (Cited on page 107.)

[275] T. Kubo, Y. Ajima, H. Hayano, et al. Electron Beam Welding for High Gradient Superconducting Cavity. In *Proceedings of IPAC2013*, volume 2, pages 2–4, 2013. (Cited on page 111.)

[276] V. Gubarev, P.D. Gall, S. Yasar, A. Sulimov, and J. Iversen. A database for the European XFEL. In *Proceedings of SRF2013*, 2013. (Cited on page 118.)

[277] K. Pearson. Note on regression and inheritance in the case of two parents. *Proceedings of the Royal Society of London*, 58(347-352):240–242, 1895. (Cited on page 125.)

[278] W. H. Pearson. Estimation of a correlation coefficient from an uncertainty measure. *Psychometrika*, 31(3):421–433, 1966. (Cited on page 125.)

[279] TU Darmstadt. Berechnung der Korrelation bei Vorliegen von Messfehlern. Technical report, TU Darmstadt, Zentrum für Statistik, 2011. (Cited on page 125.)

[280] B. Efron. Better Bootstrap Confidence Intervals. *Journal of the American Statistical Association*, 82(397):171–185, 1987. (Cited on page 125.)

[281] G. Wu, M. Ge, P. Kneisel, K. Zhao, and J. Ozelis. Investigations of surface quality and SRF cavity performance. Technical report, Fermilab, 2010. (Cited on page 128.)

[282] G. Eremeev. *Study of the High Field Q-Slope Using Thermometry*. PhD thesis, Cornell University, 2008. (Cited on page 129.)

[283] A.Yu. Aladyshkin, A. S. Mel'nikov, I. A. Shereshevsky, and I. D. Tokman. What is the best gate for vortex entry into type-II superconductor? *Physica C: Superconductivity*, 361(1):67–72, 2001. (Cited on page 129.)

Acknowledgment